

**DISPERSION AND SELF-ASSEMBLY OF COLLOIDAL 2D NANOPATELETS  
IN LIQUIDS AND POLYMER MATRICES**

A Dissertation

by

PENG LI

Submitted to the Office of Graduate and Professional Studies of  
Texas A&M University  
in partial fulfillment of the requirements for the degree of

DOCTOR OF PHILOSOPHY

Chair of Committee,	Hung-Jue Sue
Committee Members,	Tahir Cagin
	Miladin Radovic
	Hong-Cai Zhou
Head of Department,	Ibrahim Karaman

May 2016

Major Subject: Materials Science and Engineering

Copyright 2016 Peng Li

## ABSTRACT

Colloidal self-assembly of two-dimensional (2D) nanoplatelets, such as clay and graphene, has been extensively investigated to prepare oriented mesophases for structural and functional applications. Controlling the dispersion and organization of nanoplatelets in solvents and polymer matrices at the nanoscale is crucial to realizing their full potential. Inspired by highly aligned platelet-based lamellar structures observed in natural materials such as nacre, several assembly techniques have been developed which include layer-by-layer assembly, electrophoretic deposition, air/water interface assembly, etc. However, the above approaches typically share the limitations of requiring time-consuming sequential depositions or extensive energy consumption, and suffer from limited robustness and poor stability in humid environments, which severely limit large-scale applications.

The objective of this research is to gain a fundamental understanding of nanoplatelet self-assembly behavior and to efficiently control nanoplatelet mesophases in solvents and polymers via a simple and scalable manner. In this study, we investigated colloidal self-assembly behaviors based on alpha-zirconium phosphate (ZrP) nanoplatelets as a model nanoparticle. Various oligomers were employed to modify surfaces of ZrP nanoplatelets via proton exchange interaction. The exfoliated ZrP layers in epoxy form a long-range smectic order aligned parallel to the substrate surface. Detailed lyotropic behavior of the ZrP smectic mesophases in a number of solvents was characterized using small-angle X-ray scattering. These highly aligned nanocomposites exhibit exceptional

physical properties, which include outstanding oxygen barrier properties, low viscosity under shear, superb mechanical rigidity and strength, excellent fire retardation and corrosion resistance properties. Graphene and its derivatives have attracted unusual attention due to its unique mechanical, thermal, optical, and electronic properties. Here, a direct colloidal self-assembly approach was utilized to prepare photonic crystals based on 2D modified graphene oxide (GO) in aqueous solution. The GO sheets form ordered photonic structure spontaneously without the need for multiple processing steps. The wavelength of light reflected by the GO photonic crystal dispersion can be controlled over the entire visible light spectrum simply by varying the GO concentration.

In this dissertation, the fundamental principles responsible for the formation of long-range liquid crystalline order of nanoplatelets in solvents and polymer matrices are systematically investigated. The proposed research will benefit the design, synthesis, structure and property optimization, and applications of high-performance nanocomposites.

## ACKNOWLEDGEMENTS

I would like to thank my mentor and advisor, Professor Hung-Jue Sue, my committee members, Prof. Tahir Cagin, Prof. Hong-Cai Zhou, and Prof. Miladin Radovic, for their guidance throughout the course of the dissertation research.

I appreciate the support and discussions from my colleagues in Dr. Sue's research group: Minhao, Xi, Spencer, Kevin White, Haiqing, Mike, Hongfeng, Chin-Fu, Tsao-Cheng, Tatsuya, James, Chunxia, Fan, Peng Liu, Chuang, Kevin Laux, Sugiyama-san, and Mohammed, Yasheng, Farhad, Megan, Jerry, and Isabel Cantu.

I am very grateful to KANEKA Corporation for financial support throughout the duration of this research. Thanks also go to the people at MCF and MIC who have helped me with instrumentation. Special thanks are given to Dr. Krishnamoorti for SAXS, Dr. Takahara for synchrotron-based x-ray scattering techniques, Dr. Wooley for DLS work, Rita Silbernagel for her assistance in ICP-MS experiment, Fuwu Zhang for his assistance in freeze-dried SEM work, and Dr. Robert Gunther for his assistance in gas permeability measurement.

I would like to express my deepest gratitude to my family. To my parents, sister and my wife for their love and constant support all these years while I worked on my PhD.



## TABLE OF CONTENTS

	Page
ABSTRACT .....	ii
ACKNOWLEDGEMENTS .....	iv
TABLE OF CONTENTS .....	v
LIST OF FIGURES.....	viii
LIST OF TABLES .....	xv
CHAPTER I INTRODUCTION AND LITERATURE REVIEW .....	1
1.1 Introduction .....	1
1.2 Dispersion and Self-assembly of 2D Crystals .....	4
1.3 Interaction Potentials between Self-assembled Nanoparticles.....	6
1.3.1 Double Layer Repulsion.....	6
1.3.2 Steric Interaction via Oligomer Brushes .....	8
1.3.3 Depletion Interaction.....	11
1.4 Oriented Nanoplatelets in Polymer Matrices .....	14
CHAPTER II TUNABLE LYOTROPIC PHOTONIC LIQUID CRYSTAL BASED ON GRAPHENE OXIDE .....	17
2.1 Introduction .....	17
2.2 Experimental .....	20
2.2.1 Materials.....	20
2.2.2 Synthesis of Graphene Oxide .....	20
2.2.3 Characterization .....	21
2.3 Results and Discussion.....	22
2.3.1 Preparation and Exfoliation of Graphene Oxide .....	22
2.3.2 Factors Influencing Stability of 2D Crystals .....	26
2.3.3 Spectral and Structural Characterization of GO Photonic Crystals .....	33
2.4 Conclusion.....	39
CHAPTER III SPRAY-COATED EPOXY BARRIER FILMS CONTAINING HIGH ASPECT RATIO FUNCTIONALIZED GRAPHENE NANOSHEETS.....	40
3.1 Introduction .....	40
3.2 Experimental .....	43
3.2.1 Materials.....	43

3.2.2 Synthesis of Modified Graphene .....	43
3.2.3 Preparation of Epoxy/MG Barrier Film .....	44
3.2.4 Characterization .....	44
3.3 Results and Discussion.....	45
3.3.1 Preparation and Characterization of Modified Graphene in Epoxy.....	45
3.3.2 Rheological Behavior of Epoxy/Modified Graphene Suspensions.....	58
3.3.3 Gas Barrier Properties .....	62
3.4 Conclusion.....	71
<b>CHAPTER IV THERMALLY STABLE AND CONDUCTIVE FREE-STANDING HYBRID FILMS BASED ON REDUCED GRAPHENE OXIDE .....</b>	<b>72</b>
4.1 Introduction .....	72
4.2 Experimental .....	75
4.2.1 Materials.....	75
4.2.2 Synthesis and Exfoliation of ZrP Nanoplatelets.....	75
4.2.3 Preparation of De-bundled SWCNTs.....	75
4.2.4 Preparation of Graphene Oxide Based Hybrid Films.....	76
4.2.5 Characterization .....	77
4.3 Results and Discussion.....	78
4.3.1 Micromorphology of ZrP/Graphene Composites.....	78
4.3.2 Thermal Stability and Conductivity of Graphene Hybrid Films.....	86
4.4 Conclusion.....	95
<b>CHAPTER V HIGH-PERFORMANCE EPOXY NANOCOMPOSITE COATINGS CONTAINING SELF-ASSEMBLED CLAY IN SMECTIC ORDER .....</b>	<b>96</b>
5.1 Introduction .....	96
5.2 Experimental .....	98
5.2.1 Materials.....	98
5.2.2 Synthesis and Functionalization of ZrP Nanoplatelets .....	98
5.2.3 Preparation of Epoxy/ZrP Coatings in Smectic Order .....	99
5.2.4 Characterization .....	99
5.3 Preparation of Smectic ZrP Nanoplatelets in Solvents and Epoxy .....	100
5.4 Anti-corrosion Epoxy Spray Coatings Containing Smectic ZrP.....	106
5.5 Self-assembly Behavior of Oligomer Modified ZrP Nanoplatelets .....	117
5.5.1 Effect of Oligomers Tethered on ZrP Surfaces .....	117
5.5.2 Effect of ZrP Aspect Ratio .....	125
5.6 Conclusion.....	129
<b>CHAPTER VI CONCLUSION AND FUTURE WORK .....</b>	<b>131</b>
6.1 Summary .....	131
6.2 Recommended Future Research Work.....	134
6.2.1 Self-assembly and Phase Transition of Colloidal Nanoplatelets .....	134

6.2.2 Functional Properties of Composites Containing Smectic Clay .....	134
REFERENCES .....	136

## LIST OF FIGURES

	Page
Figure 1.1 Schematic of the nanoscale morphology of polymer/clay composites.....	5
Figure 1.2 (a) Repulsive and attractive forces as a function of separation distance between two colloidal particles. (b) DLVO pair interaction in colloidal suspension as a function of the ionic strength.....	8
Figure 1.3 Schematic of depletion interaction between self-assembled spherical particles (green spheres) in a solution of depletion agent molecules (grey spheres) described by Asakura model. Dashed line represents excluded volume in which center of depletion agent cannot enter.....	12
Figure 2.1 Cross-polarized light OM of the GO-L aqueous dispersion (0.4 vol %) with the sample rotation of (a) 0° and (b) 45°. (c) XRD results of the GO aqueous dispersions. Note that (I) is as-prepared GO, (II) is GO after stirring, and (III) is GO after stirring and removal of unexfoliated particles.....	23
Figure 2.2 (a, d) Tapping-mode AFM images, (b, e) height profiles, and (c, f) width distributions of GO. (a, b, c) are GO-L, while (d, e, f) are GO-S. ....	24
Figure 2.3 (a) FTIR-ATR spectrum of GO-L. (b) TGA spectra of graphite and GO-L. XPS elemental fine scan analysis of GO-L: (c) C1s spectra. (d) O1s spectra.....	25
Figure 2.4 Dynamic light scattering (DLS) results of different sized GO aqueous dispersions via three different measurement modes: (a) GO-L and (b) GO-S. GO average diameter obtained from DLS is not a true size but rather the effective hydrodynamic diameter of an equivalent sphere described by the tumbling of the platelets. The relative sizes between GO-S and GO-L can be assessed by DLS.....	28
Figure 2.5 Optical images of GO-L aqueous dispersion at NaCl concentrations of (a) $1.2 \times 10^{-5}$ M, (b) 0.008 M and (c) 0.3 M. (Left: photographic images; middle: OM images; right: cross-polarized OM images). The white arrows in (c) indicate GO-L aggregates. (d) Zeta potential of GO-L aqueous dispersion as a function of NaCl concentration.....	29

Figure 2.6 (a) Optical reflectance spectra and (b) visual images of GO-L dispersions of different structural colors. From left to right the weight fraction of GO-L is 0.91, 0.75, 0.67, 0.55, 0.51, 0.44 and 0.36 wt%, respectively. (c) Peak positions ( $\lambda_{\max}$ ) of reflectance spectra versus GO-L wt%, demonstrating the dependence of iridescent color on GO-L concentration. (d) d-spacing exhibits a linear dependence on the inverse volume fraction. D-spacing was calculated from $d = \lambda_{\max}/2\eta$ .....	32
Figure 2.7 (a) Iridescent color of GO-L gel inside a centrifuge tube. (b) and (c) show the color of GO-L gel on a glass slide from different viewing angles. (d) Difference in structural colors of GO-L gel with increasing resting time (RT) at room temperature. All photographs were taken under white light.....	35
Figure 2.8 SEM images of surface of freeze-dried GO-L photonic structures at GO-L concentrations of (a) 0.36 wt% and (b) 0.91 wt%, respectively. The dashed white lines indicate the alignment direction of the GO-L sheets.....	36
Figure 2.9 SEM images of cross-sectional view of freeze-dried GO-L photonic dispersions at various GO-L concentrations: (a) 0.36 wt% and (b) 0.91 wt%.....	37
Figure 2.10 (a) SAXS 2D patterns of GO-L aqueous dispersions at various GO-L concentrations. (b) Profiles of scattering intensity as a function of scattering vector $q$ ( $q = 4\pi\sin\theta/\lambda = 2\pi/d$ ) for various GO-L dispersions, including measured data (red line) and calculated profile (blue line) based on the 1D paracrystal model. The numbers labeled on the patterns and profiles are the corresponding GO-L concentrations.....	38
Figure 3.1 Schematic of epoxy/MG nanocomposite films preparation.....	47
Figure 3.2 Images of GO viewed using (a) AFM, (b) OM, (c, d) cross-polarized light OM, and © SAXS of GO aqueous dispersion. Profiles of scattering intensity as a function of scattering vector $q$ ( $q = 4\pi\sin\theta/\lambda = 2\pi/d$ ) for 1.32 wt% GO dispersion including measured data (red line) and calculated profile (blue line) based on the 1D paracrystal model. Inset in (b) is photograph of GO aqueous suspension.....	48
Figure 3.3 (a) Photograph of GO, rGO and MG in acetone having a concentration of 0.7mg/mL. (b) Tapping-mode AFM image, (c) height profile, and (d) size distribution of MG.....	49

Figure 3.4 (a) FTIR-ATR spectra of GO and MG; inset shows the details of wavenumber region from 1600 to 700 cm <sup>-1</sup> . (b) TGA results of GO, rGO and MG. (c) XRD of graphene oxide (GO), reduced graphene oxide (rGO), and modified graphene (MG).....	50
Figure 3.5 (a) XRD results of cured neat epoxy, graphite, and epoxy/MG films at various MG concentrations. TEM of cross-sectional epoxy/MG films at different MG loading: (b) 2.4 vol%, (c) 3.6 vol%.....	52
Figure 3.6 DMA of neat epoxy and epoxy/MG bulk samples.....	54
Figure 3.7 (a) Photograph of epoxy/MG (3.6 vol.%) film on PI substrate. OM images of epoxy/MG film surface at various MG concentrations: (b) 0.6 vol%, (c) 2.4 vol%, (d) 3.6 vol%, (e) 5.5 vol%, and (f) 7.5 vol%.....	55
Figure 3.8 GISAXS 2D diffractogram of epoxy/MG nanocomposite films at (a) 0.6 vol.%, (b) 2.4 vol.%, (c) 3.6 vol.%, and (d) 5.5 vol.% ZrP. (e) GISAXS 1D diffractogram spectrum of epoxy/MG films at various concentrations. ....	56
Figure 3.9 (a) OM and (b) cross-polarized light OM of epoxy/MG precursor (3.6 vol. %) before curing reaction.....	57
Figure 3.10 The response of the epoxy/MG suspension to (a, b) linear viscoelastic response, and (c) large amplitude oscillatory deformation.....	60
Figure 3.11 Oxygen relative permeability plots of epoxy/MG ( $P_C$ ) at various MG loadings compared to the pristine epoxy ( $P_n$ ). Predicted values from various models are also included for comparison.....	62
Figure 3.12 (a) Oxygen transmission rate (OTR) and (b) permeability of pure polyimide film, epoxy/MG (3.6 vol.%) coating on polyimide substrate, and epoxy/MG (3.6 vol.%) coating alone at different humidity conditions.....	64
Figure 3.13 (a) Experimental data and Bharadwaj barrier model predictions as a function of nanoplate aspect ratio. (b) Schematic of oxygen barrier mechanism of epoxy/MG nanocomposites.....	66

Figure 3.14 (a) Transmittance spectra of epoxy/MG films at various MG concentrations, illustrating a decreased transparency with increased MG loadings.	
(b) TGA results of epoxy/MG coatings at various MG concentrations.....	69
Figure 4.1 (a) Atomic force microscopy (AFM) image of GO deposited on mica surface from aqueous solution (inset: height profile of GO). (b) OM of GO/ZrP (System E) at 10 g/L on a glass slide (inset: photograph of the aqueous suspension).	
(c) SEM of ZrP (inset: an individual ZrP), (d) size distribution of ZrP particles.	
(e) TEM of GO/ZrP (System E) dispersion, and (f) its corresponding EDS spectrum.....	80
Figure 4.2 Polarized-light optical microscopy images of GO/ZrP (System E) after (a) 2 min and (b) 30 min of solvent evaporation. (c) Schematic of possible interaction between GO and ZrP.....	81
Figure 4.3 (a) – (c) OM images of GO/ZrP film (System E) at various magnifications. Polarized-light OM images of (d) GO film (System B) and (e) GO/ZrP hybrid film.....	82
Figure 4.4 SEM images of different free-standing films from surface view of (a) pure GO (System B), (b) GO/pristine ZrP (System C), and (c) GO/ZrP (System E). White arrows indicate big aggregated particles.....	84
Figure 4.5 SEM images of different free-standing films from cross-sectional view: (a) pure GO, (b) GO/pristine ZrP (System C), and (c) GO/ZrP (System E). EDS mapping of GO/ZrP film (System E) from cross-sectional view showing distribution of different elements: (d) C and (e) Zr element.....	85
Figure 4.6 TGA studies of GO/ZrP films with different ZrP loading. (a) Graphite, (b) GO/ZrP-43% (System F), (c) GO/ZrP-20% (System E), (d) GO/pristine ZrP-22% (System C), (e) GO/ZrP-12% (System D), and (f) GO.....	87
Figure 4.7 XPS elemental analysis: C1s spectra of (a) GO and (b) TRGO. ....	88
Figure 4.8 XRD patterns of different free-standing film samples before and after thermal annealing process.....	89
Figure 4.9 (a) Visual images, (b) SEM surface view, and (c) SEM cross-sectional view of GO/ZrP/SWCNTs (System G) film.....	91

Figure 4.10 Photographs of various free-standing films (35 mm in diameter): (a) TRGO (System H), (b) TRGO/ZrP (System I), and (c) TRGO/ZrP/SWCNTs (System J). SEM surface and cross sectional views of: (d, g) TRGO, (e, h) TRGO/ZrP, and (f, i) TRGO/ZrP/SWCNTs.....	92
Figure 4.11 Illustration of thermal reduction process of (a) GO film and (b) GO/ZrP hybrid film during annealing.....	94
Figure 5.1 (a, b) SEM images and (c) size distribution of as-prepared ZrP nanoplatelets .....	101
Figure 5.2 Stability of the Jeffamine M1000 modified ZrP with a concentration of 10 mg/mL in different solvents.....	102
Figure 5.3 Cross-polarized light optical micrographs of the oligomer modified ZrP in various solvents showing strong birefringence including: (a) xylene, (b) water, (c) acetone, (d) ethanol, (e) DMF, and (f) THF, respectively.....	103
Figure 5.4 SAXS 2D and 1D diffractograms of the oligomer modified ZrP in various solvents including (a, d) xylene, (b, e) water, and (c, f) THF, respectively.....	104
Figure 5.5 (a, b) SAXS 2D and 1D diffractograms of smectic epoxy/ZrP suspension	105
Figure 5.6 Cross-polarized light OM of epoxy/ZrP liquids at two magnifications.....	105
Figure 5.7 Schematic of the process used to prepare the smectic epoxy/ZrP coatings on a metal substrate. ....	107
Figure 5.8 (a) 2D and (b) 1D diffractograms of GISAXS, suggesting ZrP nanoplatelets are aligned parallel to the metal substrate.....	108
Figure 5.9 TEM of cross-section of smectic epoxy/ZrP coating.....	109
Figure 5.10 Potentiodynamic polarization results of bare Al alloy, neat epoxy, and smectic epoxy/ZrP-coated Al alloy.....	110



Figure 5.11 (a, b, c) Nyquist plots, and (d, e, f) Bode plots of bare Al alloy, neat epoxy, and smectic epoxy/ZrP-coated Al alloy.....	111
Figure 5.12 (a) Oxygen transmission rate (OTR) and permeability of neat epoxy and smectic epoxy/ZrP films tested under relative humidity of 50 RH% at 23°C. (b) Schematic of the improved barrier performance of aggressive oxygen.....	114
Figure 5.13 SEM images of (a) neat epoxy coating and (b) smectic epoxy/ZrP coating on the aluminum substrates after testing for evaluating adhesion according to ASTM standard D 3359-02.....	115
Figure 5.14 Fourier-Transform Infrared spectra (FTIR) of neat epoxy and smectic epoxy/ZrP nanocomposites.....	116
Figure 5.15 Schematic of surface modified ZrP nanoplatelets with various oligomers.....	117
Figure 5.16 TEM of oligomer M600 modified ZrP in an epoxy matrix. Red circles show the ZrP local domain.....	120
Figure 5.17 (a) cross-polarized light OM and (b) SAXS of ZrP-M2000/epoxy suspensions (c) TEM of oligomer M2000 modified ZrP in an epoxy matrix after curing. ....	121
Figure 5.18 DLS of ZrP nanoplatelets modified by various oligomers including M600, M1000 and M2000.....	123
Figure 5.19 TGA results of neat oligomers (a) and oligomer modified ZrP (b) under air flow condition.....	124
Figure 5.20 SEM of ZrP with small (a) and large (b) aspect ratio; (c)TEM and XRD of M1000 modified ZrP with large size in epoxy.....	126
Figure 5.21 TGA results of M1000 modified ZrP with different aspect ratio under air flow condition.....	127

Figure 5.22 Possible self-assembly behavior of oligomer modified ZrP in epoxy dominated by different interaction potentials. Where  $\delta_T$  is depletion thickness; h is distance between nanoplates;  $\Delta V$  is entropy-driven extra free volume..... 128

## LIST OF TABLES

	Page
Table 3.1 List of permeability models for polymer nanocomposites.....	63
Table 4.1 Different samples prepared and their composition.....	78
Table 4.2 GO decomposition temperatures of films with different ZrP loading.....	87
Table 4.3 XPS analysis of C, O contents and calculated C/O ratios for different films.....	89
Table 4.4 Electrical conductivity of different free-standing films.....	94
Table 5.1 TGA summary information of ZrP ( $\alpha=160$ ) modified by various oligomers.....	124
Table 5.2 TGA summary information of M1000 modified ZrP with different aspect ratio.....	127

## CHAPTER I

### INTRODUCTION AND LITERATURE REVIEW

#### 1.1 Introduction

There is significant increase in the use of nanoparticles to modify a range of physical properties of fluid and polymer systems. Colloidal manipulation of nanoscale materials has gathered enormous attention since the advent of nanotechnology. Colloidal self-assembly approach is not only an important route for low-cost device fabrication at a scalable manner, but also crucial to understanding of various fundamental phenomena such as dispersion stability, colloidal precipitation, mesophase transition, etc. Based on geometry, nanomaterials can be categorized into zero dimensional (0D) like quantum dots, one dimensional (1D) like carbon nanotubes, two dimensional (2D) like clay nanoplatelets, and complex nanostructures. Plate-like inorganic crystals normally have a layered structure where each layer is less than one nanometer in thickness and more than hundred nanometers in diameter. The layers in each crystal are stacked parallel to each other through secondary bonding such as hydrogen bonding or van der Waal forces while within each layer atoms are bonded through chemical bonding. These layered compounds have been widely used as catalysts, ion exchangers, barrier, additives, fillers, etc. Among the vast variety of nanoparticles, two representative 2D nanostructures have been chosen for the current study including modified graphene and alpha-zirconium phosphate (ZrP) nanoplatelets.

Dispersion stability and orientation of colloidal nanoplatelets in solvents and polymers is not only important to control the structural uniformity and but also crucial in realizing their full potential. Polymer/clay nanocomposites have received tremendous attention in recent years due to their low cost, excellent performance, and potential for expanding the application space of polymers. However, there remain significant challenges to achieving high-volume production of high-performance polymer/clay nanocomposites for commercial applications, particularly due to current limitations in the incorporation of high levels of clay in polymer matrices without causing clay agglomeration or requiring sophisticated and energy-intensive sample preparation steps. In this dissertation a novel colloidal approach to disperse and assemble nanoplatelets in various solvents and polymers is introduced. The relationship between liquid crystalline microstructure and physical properties are discussed.

The primary objectives of this dissertation are to study the colloidal dispersion and self-assembly behavior of 2D nanomaterials in solvents and polymers, to understand their phase transition mechanisms, and to explore the high-performance physical properties based on high aligned liquid crystalline structure. The ZrP nanoplatelets are chosen as a model system due to their well-controlled chemical structure, well-defined geometries good chemical stability, and ease of exfoliation. The concepts employed in this dissertation are relatively universal and should have widespread impact in the field of nanoparticle colloidal self-assembly.

The dissertation is organized as follows. In Chapter I a literature review is presented regarding dispersion stability and self-assembly of nanoplatelets in solvent and polymers. Chapter II discusses tunable lyotropic photonic liquid crystal based on graphene oxide (GO). The reflected color of GO suspensions can be tuned across the entire visible spectrum by adjusting the GO concentration. The GO aspect ratio and the colloidal interactions between GO sheets are among the important factors that control the formation of GO photonic crystals. In Chapter III, exfoliated epoxy nanocomposites containing large-aspect-ratio modified graphene (MG) were prepared via a facile spray coating approach. The MG sheets are individually exfoliated and form liquid crystalline mesophases in epoxy precursor at a low concentration. The epoxy/MG nanocomposite films exhibit significantly improved gas barrier properties at different humidity levels. Chapter IV discusses thermally stable and highly conductive films prepared based on thermally reduced graphene oxide and exfoliated ZrP hybrids. With the incorporation of the inorganic nanoplatelets, the thermal stability and structural integrity of the hybrid films are greatly improved, while good electrical conductivity of the reduced GO is maintained. Chapter V focuses on the self-assembly behavior of 2D ZrP nanoplatelets in solvents and an epoxy matrix. Lyotropic liquid crystal behavior of ZrP nanoplatelets was observed in a number of different solvents, which suggests the phenomena are largely entropically driven and would be suitable for various coating systems. Epoxy nanocomposite coatings containing self-assembled zirconium phosphate nanoplatelets (ZrP) in smectic order were successfully prepared by spray-coating using a simple, energy-efficient fabrication process that may be suitable for industrial use. Various

subjects including oligomers tethered on ZrP surface, ZrP aspect ratio and nanoscale interaction are discussed. Aluminum substrates with smectic epoxy/ZrP coatings showed a substantial improvement in corrosion resistance compared to the metal surface coating with unfilled epoxy alone. The results show that the epoxy coatings containing highly aligned ZrP nanoplatelets in smectic order may be used to effectively protect metal surfaces from corrosion using an efficient approach. Each chapter from Chapters II to V is related in the sense that they are associated with two-dimensional nanoparticles for various applications. Chapter VI and VII present the conclusion of this dissertation and future work.

## **1.2 Dispersion and Self-assembly of 2D Crystals**

2D crystals, alternatively nanoplatelets, are flat monolayers of nanoparticles with high aspect ratios. A number of different inorganic reinforcing platelets have been used for fabrication of high-performance nanocomposites such as silicates, metal oxides, talc, and zirconium phosphate. 2D discotic suspensions have been found to show a rich variety of distinct phases, including isotropic, nematic, columnar, smectic, and chiral phases. Self-assembly of photonic structure based on colloidal two-dimensional (2D) inorganic nanoplatelets has been extensively investigated.[1-3] Gabriel et al.[3] studied dispersion of  $\text{H}_3\text{Sb}_3\text{P}_2\text{O}_{14}$  nanoplatelets, which forms a gel-like lamellar phase in aqueous solution. It was also reported[2] that sterically-stabilized gibbsite nanoplatelets suspensions exhibited strong Bragg reflection in the visible light range due to the formation of long-range smectic liquid crystal phases. Moreover, if functional platelets

with a unique set of properties are utilized, then it is possible to design materials with advanced properties tailored across different functionalities and multiple length scales.

As shown in Figure 1.1, typically there are several different micromorphologies of polymer/clay nanocomposites which include phase-separated aggregated phases, intercalated phases, disordered exfoliated phases, and highly aligned liquid crystalline phases.

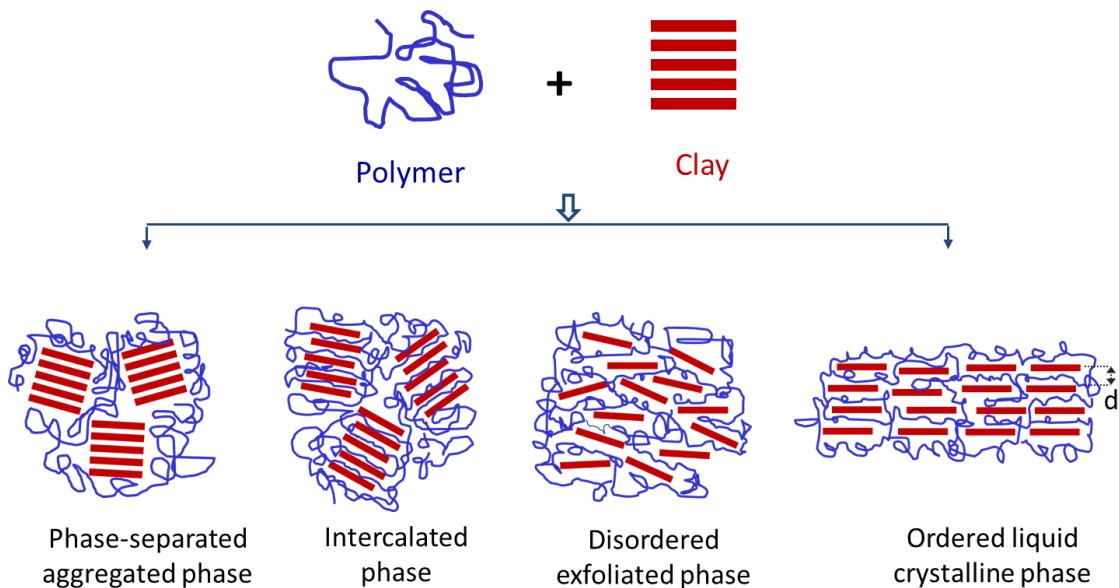


Figure 1.1 Schematic of the nanoscale morphology of polymer/clay composites.



## 1.3 Interaction Potentials between Self-Assembled Nanoparticles

### 1.3.1 Double Layer Repulsion

Repulsion (Coulombic or steric) and attraction (van der Waals, Coulombic, or depletion interaction) are the major forces that govern the colloidal self-organization process.[4,5] The DLVO (Derjaguin, Landau, Verwey and Overbeek) theory[6] explains the colloidal stability of charged nanoparticles considering that the total interaction potential between colloidal particles is in function of the interparticle separation (Figure 1.2 (a)). The total DLVO energy potential ( $V_{DLVO}$ ) is equal to the summation of double layer repulsive potential ( $V_R$ ) and the Van der Waals attractive potential ( $V_A$ ) and given as follows:

$$(1.1) \quad V_{DLVO} = V_R + V_A$$

$$(1.2) \quad V_R = k \frac{q_1 q_2}{\epsilon x} e^{-x/\lambda_D} \quad \lambda_D = \frac{1}{\sqrt{4\pi B n}} \quad V_A = \frac{-A}{12\pi x^2}$$

where  $\epsilon$  is dielectric constant;  $q_1$  and  $q_2$  are charges of particles;  $n$  is the free ion concentration;  $k$  is the Boltzmann constant;  $B$  is Bjerrum length. It is the distance between two elementary charges at which their interaction is equal to  $kT$ ;  $x$  is the interparticle separation;  $A$  is Hamaker constant.  $\lambda_D$  is Debye screening length (or double layer thickness). In a charged colloidal suspension, counterions (with opposite charges as the nanoparticles) accumulate at the colloidal surface while co-ions (with the same

charges as the nanoparticles) are depleted from the colloidal surface. Far from the colloidal particles, the concentration of these two ions attains a constant averaged value. The inhomogeneous layer including Stern layer and Slipping layer is described as a double layer, which strongly depends on the ionic strength.[7] For a given colloidal particle geometry and Van der Waals interaction, the effect of ionic strength on the DLVO potential is qualitatively represented in Figure 1.2 (b). From (i) to (iv) more salts are added in the colloids. At low ionic concentration (i), the double layer repulsive force ( $V_R$ ) dominates, the maximum of  $V_{DLVO}$  exceeds several  $kT$  and stable colloidal system is expected. As salt concentration is increased (ii), there is a local energy barrier that could prevent the irreversible aggregations of colloidal nanoparticles. At large interparticle separation a secondary minimum appears which could lead to reversibly flocculated aggregates. At very high salt concentration (iii; iv), the Van der Waals attractive force is dominant and the colloidal suspension become unstable with irreversible aggregations.

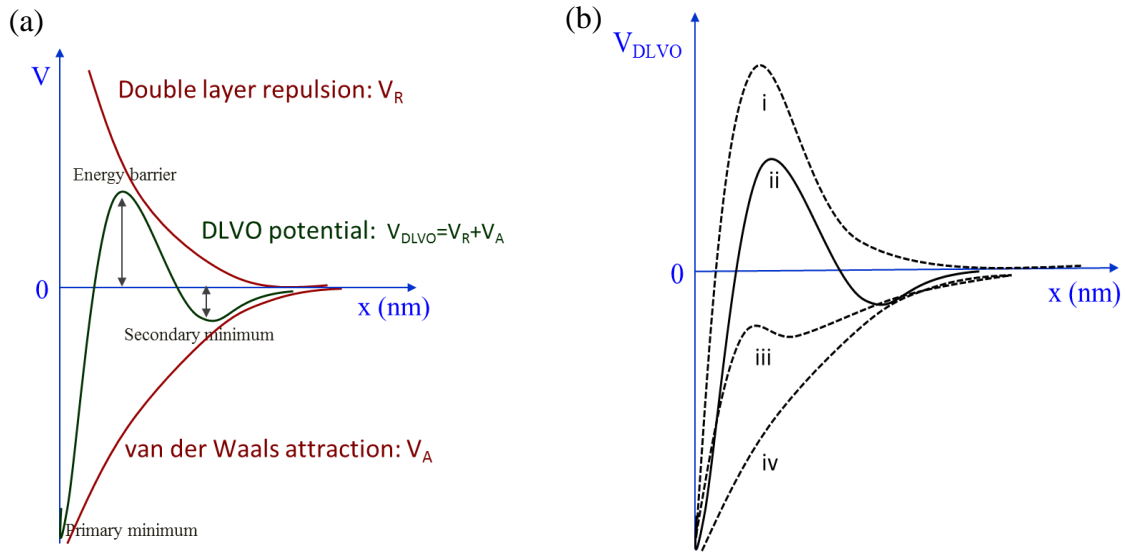


Figure 1.2 (a) Repulsive and attractive forces as a function of separation distance between two colloidal particles. (b) DLVO pair interaction in colloidal suspension as a function of the ionic strength.

### 1.3.2 Steric Interaction via Oligomer Brushes

Double layer repulsion in apolar solvents is hard to achieve as dissociation is less likely to occur. Colloidal dispersions can be stabilized by oligomers or polymers attached to the particle surface. As two colloidal particles approach each other the local osmotic pressure increases significantly due to steric hindrance of the attached oligomer or polymer chains. The Flory-Krigbaum theory[8] considers the repulsive interaction of overlapping brushes with brush density distribution function ( $\varphi$ ) in a good solvent (Flory-Huggins chain-solvent interaction parameter,  $\chi$  is less than 0.5) and given as follows:

$$(1.3) \quad V_{steric} = 2k_B T \cdot (v_s^2/v_i) \cdot \left(\frac{1}{2} - \chi\right) \cdot \int \phi_1 \phi_2 dV$$

$$(1.4) \quad V_{elastic} = 2k_B T \cdot \left[ \frac{\delta^2 - 1}{2} - \ln \delta \right] \quad \delta = x/L$$

where  $v_s$  is Kuhn segment volume and  $v_i$  is solvent molecular volume. The free energy of interaction between brushes consists of two factors: an osmotic repulsion ( $V_{steric}$ ) and a stretching factor ( $V_{elastic}$ ) originating from the elastic energy gain upon retraction of brushes. The repulsive interaction is significant as the brushes begin to overlap. Onsager's theory[9] predicts that hard rigid rods form nematic phases when their volume fraction in the suspension become larger than a critical value ( $\phi_c$ ). This is due to a net gain in entropy as the loss of orientational entropy is compensated by an increase in translational entropy. Smectic phases are rarely seen and tend to be present only at high volume fractions or when there are long range repulsive interactions between nanoplatelets. A similar behavior is observed in 2D crystals. The challenge is to preserve the long-range positional and orientation order of 2D mesophases from the liquid suspensions to a robust solid form that can be used to address technological needs.

The approach of tethering oligomer brushes on nanoparticle surfaces to create repulsive steric interaction has long been used to stabilize and assemble the colloidal particles. The theory of oligomer brushes has been established through various methods including self-consistent field theory (SCF), scaling theory, Monte Carlo theory[10-12] and so on. Based on the assumption that oligomers tethered on nanoparticles are well soluble in surrounding solvents, the surface-tethered oligomer brushes can be

characterized by several parameters including oligomer length, excluded volume parameter between brush ( $\omega$ ), oligomer grafting density and morphology of oligomers tethered on nanoparticles. Specifically oligomer length is described by Flory radius of the oligomer in random coil configuration ( $R_F \sim N^{3/5} b$ ) where  $N$  is degree of polymerization and  $b$  is Kuhn characteristic length. The other parameter is average distance between grafted oligomers ( $\Gamma^{-0.5}$ ) where  $\Gamma$  is the surface grafting density in the unit of  $1/\text{nm}^2$ . [13]

Steric interaction increases upon compression due to the increase in osmotic pressure with brushes overlapping region. Specifically the entropic repulsion is derived from the osmotic pressure between the oligomer brush region and pure solvent phase. The increased osmotic pressure is due to the unfavorable exclusion of solvent molecules in the oligomer overlapping region. In addition, the elastic component of brush compression also contributes to the repulsive interaction which is in function of brush compression ratio. Based on the SCF treatment, the equilibrium oligomer length ( $h$ ) and the free energy per unit area may be approximated as [12]

$$(1.5) \quad h_0 = N \left( \frac{12\Gamma\omega b^5}{\pi^2} \right)^{1/3}$$

$$(1.6) \quad f(h) = \frac{kT\Gamma\pi^2 h_0^2}{6Nb^2} \left[ 0.5 \left( \frac{h_0}{h} \right) + 0.5 \left( \frac{h}{h_0} \right)^2 - 0.1 \left( \frac{h}{h_0} \right)^5 \right]$$

For nanoparticle with curved geometries, steric interaction potentials may be derived via the Derjaguin approximation. Specifically, steric repulsion ( $U_s$ ) between two spherical nanoparticles with short tethered oligomer length ( $h < a$ ) is given by [14,15]

$$(1.7) \quad U_s(u) \approx \frac{2\pi a_1 a_2}{(a_1 + a_2)} \frac{kT\Gamma\pi^2 h_0^2}{6Nb^2} \left[ -\ln u - \frac{9}{5}(1-u) + \frac{1}{3}(1-u^3) - \frac{1}{30}(1-u^6) \right]$$

Interaction potentials between oligomer modified gold nanoparticles with radius of 25 nm were studied by Rubenstein.[13] The nanoparticles are functionalized by polyethylene glycol ligands with either 10 or 20 chemical monomers ( $n$ ). It shows the minimum energy separation between nanoparticle surfaces is slightly less than two times of equilibrium brush thickness. The repulsive interaction potential significantly depends on oligomer length and surface grafting density. The specific parameters in this model include grafting density of  $1 \text{ nm}^{-2}$  and excluded volume parameter of 1. The minimum energies of gold nanoparticles modified by short ( $n=10$ ) and long ( $n=20$ ) oligomers are  $-8kT$  and  $-2kT$ , respectively. In contrast bare gold particles without surface modification only have minimum energy of  $-400kT$ .

### 1.3.3 Depletion Interaction

In addition to repulsive interactions, entropic effects can also induce attractive forces responsible for self-assembled microstructures of nanoparticles. The concept of depletion interaction was first explained by Asakura and Oosawa[16] using a model of large hard-sphere particles immersed in a solution containing small solute species (i.e.,

depletion agents) as shown in Figure 1.4. An osmotic pressure develops when large particles get so close that no solute molecules occupy the region between them. The attractive depletion interactions occur due to net osmotic pressure and push spheres towards to each other. As the separation of self-assembled spherical particles is large enough at low volume fraction (Figure 1.3 a), total excluded volume of the colloidal system keeps constant so there is no entropically driven depletion interaction. Above a critical volume fraction of self-assembled particles (shown in Figure 1. 3 b), overlapping of excluded volume shell occurs which increases the free volume available to the solute molecules, decreasing the free energy of the colloidal system. As a result, attractive depletion interactions represented by yellow arrows (Figure 1.3 b) are created due to increased entropy and push particles together.

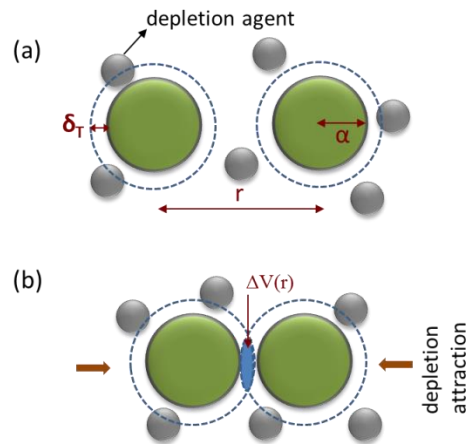


Figure 1.3 Schematic of depletion interaction between self-assembled spherical particles (green spheres) in a solution of depletion agent molecules (grey spheres) described by Asakura model. Dashed line represents excluded volume in which center of depletion agent cannot enter.

Consider two hard-sphere particles immersed in a solution of smaller depletion agents. The solvent molecules may be treated as a uniform phase in which the particles and the solute interact. As the particle surfaces approach a separation smaller than the diameter of depletion agents, it created an extra free volume ( $\Delta V_{\odot}$ ) available to depletion agents due to the overlapping of excluded volume. The increased free volume leads to a decrease in free energy of the overall system which is defined as follows[17,18]

$$(1.8) \quad F = -kT \ln Q = -kT \ln V^N$$

where  $k$  is Boltzmann constant and  $Q$  is the canonical partition function that is approximated by the number of solute species ( $N$ ) and the total free volume accessible to solute ( $V$ ).  $V$  is expressed in terms of the initial volume,  $V_0$ , and the volume gained,  $\Delta V_{\odot}$ , defined as

$$(1.9) \quad V = V_0 + \Delta V_{\odot}$$

Thus the free energy of the system and the free energy of interaction ( $\Delta F(r)$ ) is given by

$$(1.10) \quad F = -NkT \ln [V_0 + \Delta V(r)] \approx -NkT \left[ \ln V_0 + \frac{\Delta V_{\odot}}{V_0} \right]$$

$$(1.11) \quad \Delta F(r) = F(r) - F(\infty) = -NkT \Delta V(r)/V_0$$

In the case of spherical particle and depletion agents, the separation  $\odot$  dependence of the entropic depletion interaction potential becomes a simple geometric defined as



$$(1.12) \quad U_{dep}(r) = -\frac{\pi p_0}{12} [2(2a + \sigma)^3 - 3(2a + \sigma)^2 r + r^3] \quad (2a < r < 2a + \sigma)$$

In the context of self-assembly, entropic depletion attraction has been used to assemble a number of various colloidal systems including block-copolymer micelles, [19] nanoplatelets particles, semiconductor nanorods and cubic colloids[20,21]. It was reported[20] that depletion attractive interaction can be used for the effective shape-selective separation from binary mixture of nanorods and spheres with similar surface chemistry. There are several parameters influencing depletion interaction which can be used to engineer self-assembly process at the nanoscale. Aspect ratio of self-assembled particles, concentration and geometry of depletion agents, and extra free volume gained,  $\Delta V^{\circ}$  play an important role in engineering the self-assembly process.

#### **1.4 Oriented Nanoplatelets in Polymer Matrices**

Polymer nanocomposite containing 2D plate-like nanostructure such as graphene and its derivatives and clay,[22-24] have been extensively reported due to their low cost, excellent mechanical properties, improved the corrosion resistance of metals and gas barrier performance, and unique electronic properties.[25-27] It has been found that the performance of polymer/nanoplatelet composites strongly depend on the nanoplatelet aspect ratio, volume fraction, dispersion level, and particularly the degree of alignment of the fillers. Biological materials such as nacre (mother-of-pearl) have outstanding strength and stiffness due to their robust brick-and-mortar architecture, which consists of alternating layers of soft proteins and aligned calcium carbonate platelets.[28] The

mechanical performance of polymer/clay nanocomposites may potentially be significantly improved by achieving similar architecture. Transferring these highly regular and organized structures into a structural polymeric system may lead to commercially viable materials suitable for a variety of high performance engineering applications, such as light-weight vehicles, high-performance packaging materials, and biomedical implants, but must be achieved in an efficient and scalable manner.[29]

A number of different inorganic reinforcing platelets have been used for the fabrication of high-performance polymer nanocomposites, such as graphene, graphene oxide, and clay.[30-32] Significant improvements in stiffness and strength have been achieved at rather low nanofiller concentrations, particularly in the case of polymer nanocomposites reinforced with high aspect ratio, exfoliated clay nanoparticles. [32] Nevertheless, improvements in strength and modulus at high clay concentrations are still notably lower than those anticipated based on theoretical models for reinforced polymers. The limitations are mainly attributed to difficulties in achieving high volume fraction of well-dispersed and highly ordered nanoplatelets in polymer matrices without nanoplatelet agglomeration.

Several assembly techniques have been developed to achieve the brick-and-mortar structure and corresponding mechanical properties of biological composites. Kotov[28] et al. used LbL assembly to fabricate a polyvinyl alcohol (PVA) hybrid film containing 50 vol.% montmorillonite (MMT) that showed exceptionally large tensile strength of 400 Mpa and Young's modulus of 106 Gpa. The tensile properties greatly exceed those

of natural nacre, which has a tensile strength of 140-170 Mpa and Young's modulus of 60-70 Gpa.[33] Using controlled freeze-casting of ceramic aqueous suspensions, Ritchie[34] et al. designed a poly(methyl methacrylate) (PMMA) film containing aluminum oxide platelets and observed lamellar organization. At concentration of 80 vol.% aluminum oxide, the tensile strength of the composite was reported to be 200 Mpa. Most previous approaches for preparing highly aligned lamellar structures are limited in scale and are often highly specific to certain polymer/clay systems.

Plate-like nanostructures, such as graphene and clays, are excellent barrier materials to gases and moisture and have been integrated with polymeric binding resins and applied as nanocomposite coatings to improve the corrosion resistance of metals. [35-38] The barrier properties of these protective coatings strongly depend on the aspect ratio, volume fraction, dispersion level, and, in particular, degree of alignment of the fillers. Inspired by highly aligned platelet-based lamellar structures observed in natural materials such as nacre, several assembly techniques have been developed to fabricate polymer/clay nanocomposites with lamellar structure, such as layer-by-layer assembly, ice templating and sintering of ceramics, vacuum-assisted self-assembly, electrophoretic deposition, and air/water interface assembly.[39-48] However, the above approaches typically share the limitations of requiring extensive energy consumption, and suffer from limited robustness and poor stability in humid or aqueous environments, which severely limit commercial use.

## CHAPTER II

### TUNABLE LYOTROPIC PHOTONIC LIQUID CRYSTAL BASED ON GRAPHENE OXIDE\*

#### 2.1 Introduction

An intriguing phenomenon in nature is structural coloration, which is commonly developed in biological communication, mimicry, and mate selection.[49-51] An exemplary example of structural coloration can be observed in fruit pollia 17irconyl17e, which exhibits a brilliant iridescent color caused by Bragg reflection of periodically stacked multilayers of cellulose microfibrils.[52] In the realm of chemistry, structural coloration in solutions of surfactant and inorganic nanoplatelets has been demonstrated, which is caused by the formation of long-range ordered mesophases.[2,53] Essentially, when periodic photonic structures with interlamellar spacing on the order of wavelength of visible light are formed, Bragg reflection in the visible wavelengths occurs. These photonic materials have attracted significant attention in recent years due to their application in controlling propagation of light at a different range of frequencies.[54,55]

---

\*Reprinted with permission from “Tunable Lyotropic Photonic Liquid Crystal Based on Graphene Oxide” by Peng Li, Minhao Wong, Xi Zhang, Haiqing Yao, Ryohei Ishige, Atsushi Takahara, Masahiro Miyamoto, and Hung-Jue Sue. 2014, ACS Photonics, 1, 79–86. Copyright (2013) by American Chemical Society. <http://pubs.acs.org/doi/abs/10.1021/ph400093c>

Self-assembly of photonic structure based on colloidal two-dimensional (2D) inorganic nanoplatelets has been extensively investigated.[1-3] Repulsion (Coulombic or steric) and attraction (van der Waals, Coulombic, or depletion interaction) are the major tools applied to govern the colloidal self-organization process.[4,5] Gabriel et al.[3] studied the dispersion of  $\text{H}_3\text{Sb}_3\text{P}_2\text{O}_{14}$  nanoplatelets, which forms a gel-like lamellar phase in aqueous solution. Iridescence was observed as water swells the  $\text{H}_3\text{Sb}_3\text{P}_2\text{O}_{14}$  gel to increase interlamellar spacing to an appropriate distance. It was also reported[2] that sterically-stabilized gibbsite nanoplatelets suspensions exhibited strong Bragg reflection in the visible light range due to the formation of long-range smectic liquid crystal phases. These oriented colloidal platelets can be used as templates for generation of ordered solid structures with unique photonic properties.[1] Moreover, if functional 2D platelets with a unique set of properties are utilized, then it is possible to design materials with advanced properties tailored across different functionalities and multiple length scales.

Compared to inorganic 2D nanoplatelets, graphene and its derivatives have attracted unusual attention due to its unique mechanical, thermal, optical, and electronic properties.[56-59] Chemically derived graphene oxide (GO) has traditionally served as a precursor for synthesizing graphene on large scale. Because of its easy processability, water solubility, heterogeneous electronic structure, and accessible oxygen-containing functional groups, GO shows great potential in various nanotechnology applications, including solar cells, cellular imaging, chemical and biological sensors, and advanced optoelectronics device.[60-63] Compared with graphene, GO is fluorescent over a broad

range of wavelengths due to the recombination of electron-hole pairs in localized electronic states.[64] The embedded oxygen-containing functional groups also allow GO to interact with various organic and inorganic species for preparation of advanced functional hybrids.[65,66] Furthermore, chemical reduction of GO through the removal of oxygen species and/or rearrangement of carbon atoms can achieve the recovery of  $sp^2$  network structure, which provides a pathway for tailoring its optoelectronic properties.[67] However, exfoliated GO usually exhibits irregular size, shape, and wrinkled surface morphology. Therefore, it is extraordinarily challenging to manipulate colloidal GO to form a long-range ordered structure without using complex chemical treatment or confinement. To our knowledge, there is no known literature reporting GO-based photonic structure through direct colloidal self-organization to exhibit tunable structural color over the entire visible light spectrum to date.

Here, we report the preparation of GO photonic crystal dispersions in an aqueous solution *via* a simple self-assembly approach. The light reflection from the GO photonic dispersion can be tuned to cover the entire visible spectrum simply by varying the GO concentration. Various factors that affect the formation of GO photonic structure are discussed. The present findings show feasibility of development of novel graphene-based materials for potential applications in sensors, tunable reflective filters, and many other optoelectronic devices.[68,69]

## **2.2 Experimental**

### **2.2.1 Materials**

Graphite was obtained from Bay Carbon Inc. Hydrogen peroxide ( $\text{H}_2\text{O}_2$ , 30wt.%), potassium permanganate ( $\text{KmnO}_4$ ), barium sulfate ( $\text{BaSO}_4$ ), and sodium nitrate ( $\text{NaNO}_3$ ) were purchased from Aldrich and used as received.

### **2.2.2 Synthesis of Graphene Oxide**

GO was synthesized from purified natural graphite using the modified Hummers method.[70] First, graphite (0.5 g) was added into a 250 mL flask containing 50 mL of concentrated  $\text{H}_2\text{SO}_4$  and 0.5 g of  $\text{NaNO}_3$ . After stirring for 20 min, the flask was immersed in an ice bath and  $\text{KmnO}_4$  (0.3 g) was slowly added during stirring. Upon oxidation for 3 h, 23 mL of deionized (DI) water was heated to 70 °C and slowly added into the mixture. After 30 min, the reaction mixture was diluted with 70 mL of 70 °C DI water, followed by the addition 10 mL of  $\text{H}_2\text{O}_2$  to neutralize excess  $\text{KmnO}_4$ . Then the mixture was washed with DI water and a 5% HCl aqueous solution numerous times to remove the residual metal species.

The GO after washing was dissolved into an aqueous suspension with a concentration of 1.5 mg/mL, followed by mechanical stirring for 2 days. Then, the GO dispersion was subjected to mild centrifugation at 3000 rpm for 7 min to remove a small amount of non-exfoliated GO particles. Subsequently, the pH value of the purified GO

dispersion was adjusted to about 2.5 by using diluted HCl and stirred for 6 h. During this process, a portion of the GO became precipitated. Next, the GO sediments and residual supernatant were separated by centrifugation. The relatively small-sized residual GO in the supernatant was defined as GO-S. The sediment GO with a relatively large size was denoted as GO-L and was redispersed in an aqueous dispersion. The GO-L dispersion was further centrifuged at 12000 rpm for 90 min. Afterwards, the GO-L gelled at the bottom of centrifuge tube, which is designated as GO-L gel. The GO-L gel was then redispersed in water at different concentrations to obtain the GO-L photonic crystal dispersions.

### **2.2.3 Characterization**

Scanning electron microscopy (SEM) images were acquired using a JEOL JSM-7500F Field Emission-SEM (FE-SEM). X-ray diffraction (XRD) patterns were obtained on a Bruker D8 Advanced Power X-ray diffractometer with Cu-K $\alpha$  incident radiation ( $\lambda=1.5418$  Å). Fourier transform infrared spectroscopy under attenuated total reflectance mode (FTIR-ATR) was performed using a Nicolet Avatar 360. Dynamic light scattering (DLS) measurements were conducted on a Brookhaven Instruments (Holtsville, NY). Optical micrographs (OM) were collected using an Olympus BX60 optical microscope. Inductively coupled plasma-mass spectrometry (ICP-MS) was performed using a Perkin Elmer DRCII ICP-MS. X-ray photoelectron spectroscopy (XPS) was performed with a Kratos Axis Ultra Imaging X-ray photoelectron spectrometer. Tapping-mode atomic force microscopy (AFM) was carried out with a Digital Instruments Nanoscope AFM



system. Thermogravimetric analysis (TGA) of samples was carried out on a Q500-TGA from TA instruments. Small-angle x-ray scattering (SAXS) was performed at the Japan Synchrotron Radiation Research Institute (JASRI) Spring-8 facility located in Hyogo, Japan. The scattering vector is defined by  $q = (4\pi/\lambda) \sin \theta$ , where  $\lambda$  is the wavelength of the x-rays, and  $2\theta$  is the angle between the incident x-ray beam and the scattered x-rays.

To demonstrate that the color of iridescence changes at various GO concentrations, reflectance spectroscopy was performed using a Shimadzu 3600 UV-vis-NIR spectrophotometer. The GO dispersions were injected into a cuvette (25.4 mm  $\times$  15.0 mm  $\times$  1.3 mm, 2.0 mm optical path length) made from two thin rectangular glass plates (Fisher-Scientific) that were double-sealed by solvent resistant epoxy (PermaPoxy 5 min) and silicone (Loctite RTV 587 Blue). White BaSO<sub>4</sub> powder was used as a standard for analyzing the reflectance of the samples.

## **2.3 Results and Discussion**

### **2.3.1 Preparation and Exfoliation of Graphene Oxide**

In this work, a facile amphiphilic self-assembly approach to fabricate GO-based photonic crystal with obvious structural coloration under white light is reported. GO can be considered a negatively charged amphiphilic molecule due to its combination of hydrophilic oxygen-containing functional groups and a hydrophobic basal plane. The successful preparation of the unique GO photonic structure does not require complex

procedures. Rather, it is achieved by tailoring GO synthesis and manipulating the colloidal interaction during the self-assembly process.

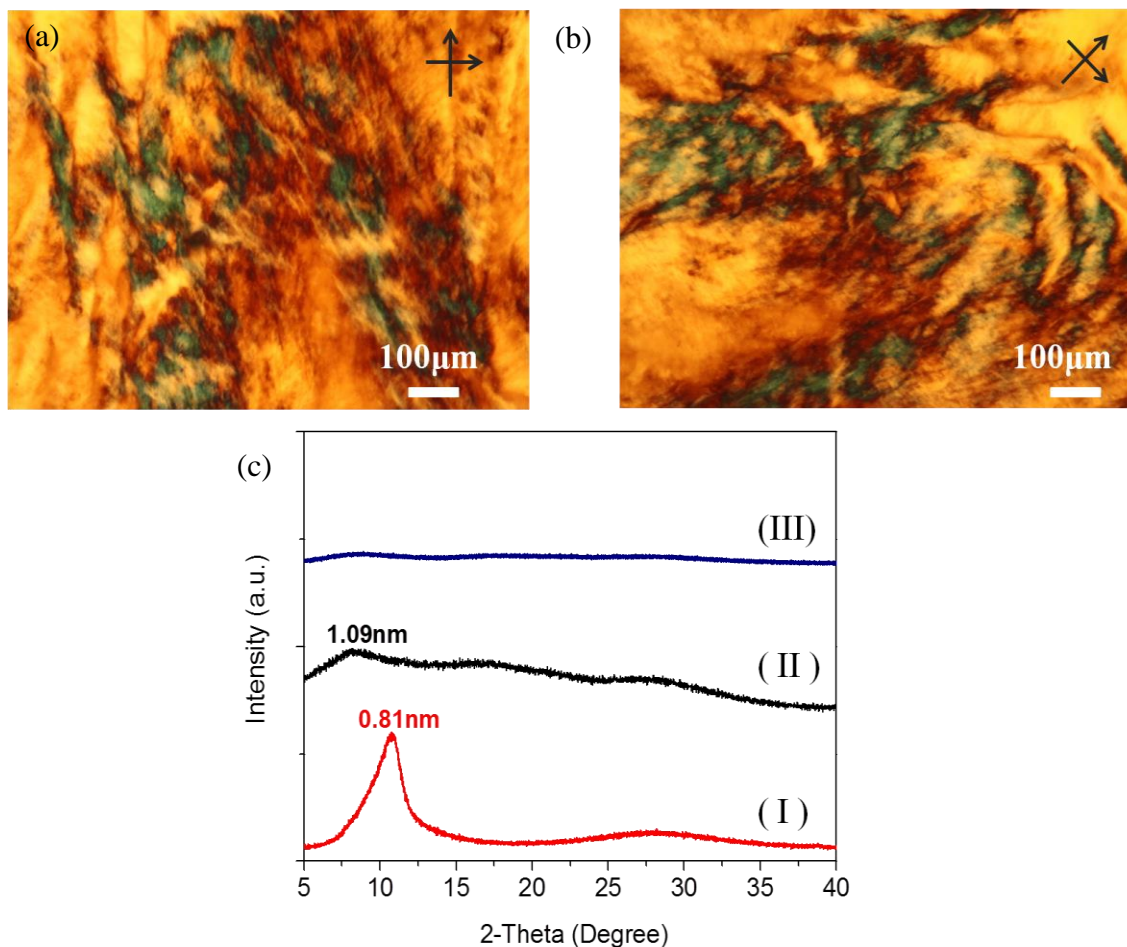


Figure 2.1 Cross-polarized light OM of the GO-L aqueous dispersion (0.4 vol.%) with the sample rotation of (a) 0° and (b) 45°. (c) XRD results of the GO aqueous dispersions. Note that (I) is as-prepared GO, (II) is GO after stirring, and (III) is GO after stirring and removal of unexfoliated particles.

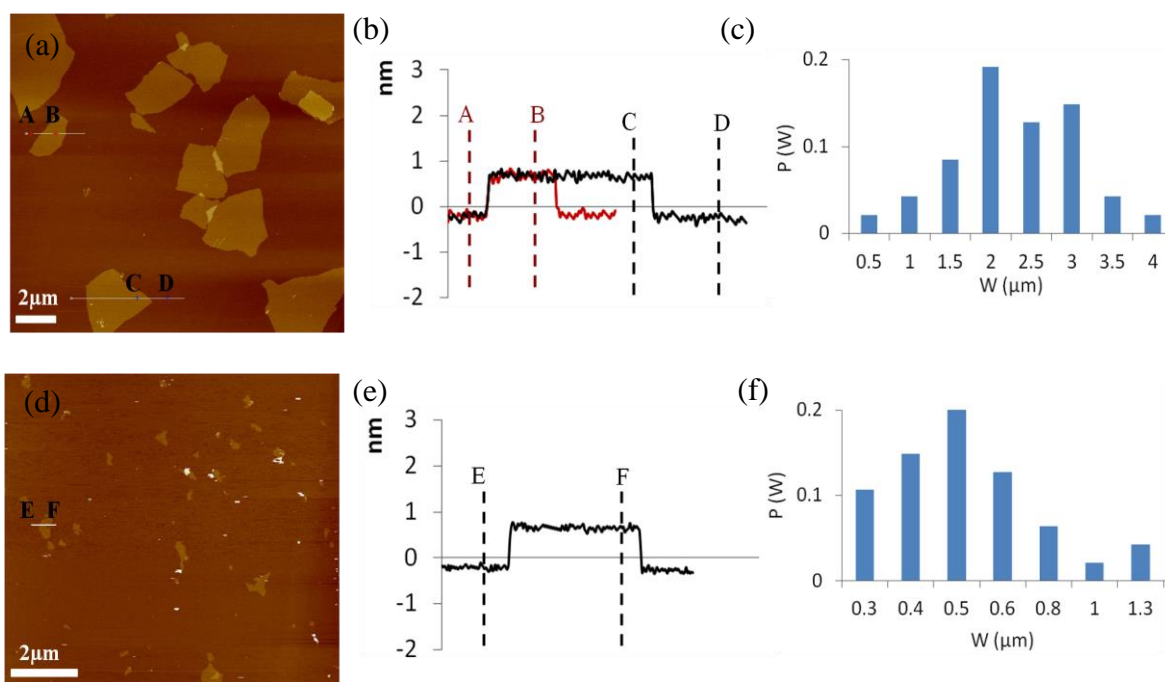


Figure 2.2 (a, d) Tapping-mode AFM images, (b, e) height profiles, and (c, f) width distributions of GO. (a, b, c) are GO-L, while (d, e, f) are GO-S.

The GO utilized in this study was synthesized by a modified Hummers method, then exfoliated in water with an aid of mechanical stirring. As shown in Figure 2.1©, the XRD pattern of as-prepared GO dispersion before exfoliation exhibits a diffraction peak at  $2\theta = 10.8^\circ$ , which corresponds to an interlayer spacing of 0.81 nm. After mechanical stirring, this diffraction peak disappears, suggesting that most of the GO sheets have been exfoliated or intercalated. However, a small peak at  $2\theta = 8.1^\circ$  was still observed, which corresponds to an interlayer d-spacing of 1.09 nm. This indicates the presence of unexfoliated GO residue in the dispersion. The increased d-spacing from 0.81 nm to 1.09 nm is possibly due to the formation of hydrogen-bonded networks, which involve

functional groups on the GO surface and water molecules within the interlayer cavities.[71] A limited amount of unexfoliated GO residue was then carefully removed by centrifugation. After that, no observable XRD diffraction peaks could be detected (Figure 2.1©), indicating the presence of a well-exfoliated GO aqueous dispersion. The GO suspension was further characterized using AFM to confirm its exfoliation state. As shown in Figure 2.2, the GO sheets are indeed exfoliated with a thickness of about 0.9 nm. This thickness is larger than that of an ideal graphene sheet due to the presence of oxygen-containing functional groups on the GO basal plane.[66] Finally, the presence of lyotropic mesophase of GO-L in aqueous solution was demonstrated through cross-polarized light observation (Figure 2.1(a, b)).

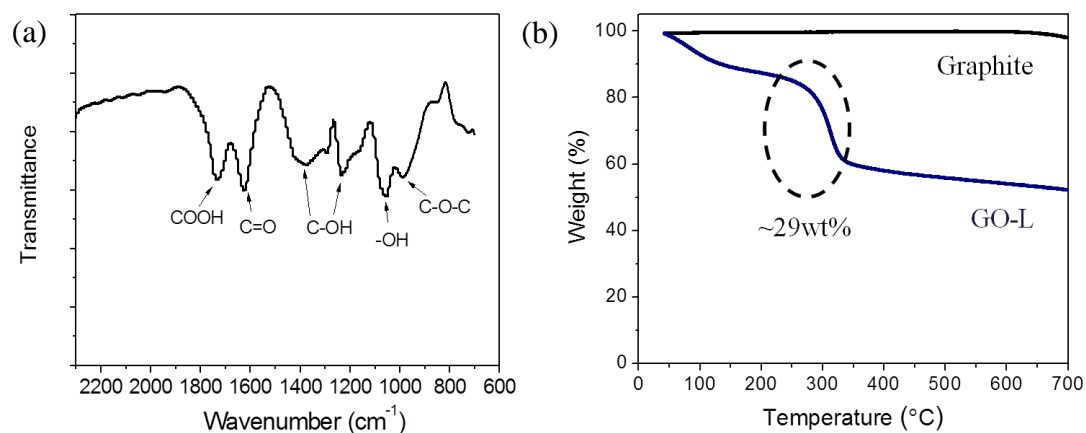


Figure 2.3 (a) FTIR-ATR spectrum of GO-L. (b) TGA spectra of graphite and GO-L. XPS elemental fine scan analysis of GO-L: (c) C1s spectra. (d) O1s spectra.

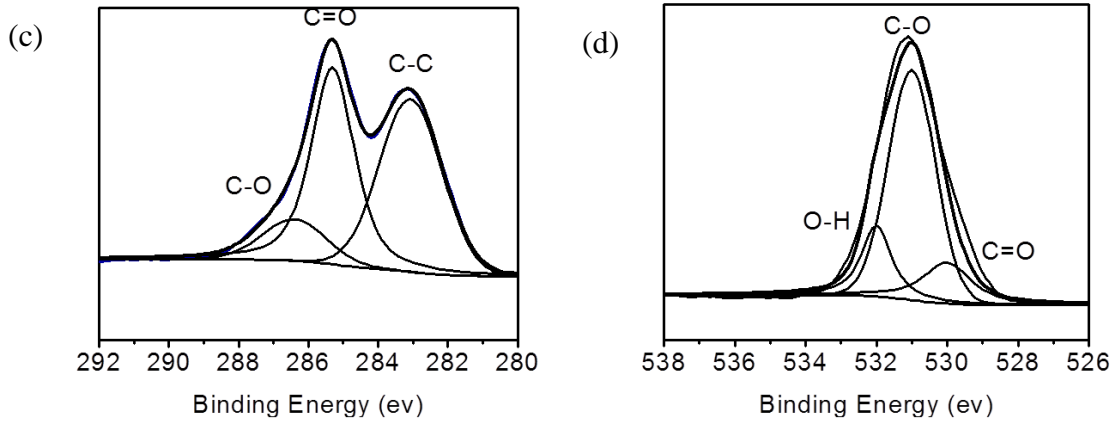


Figure 2.3 Continued.

### 2.3.2 Factors Influencing Stability of 2D Crystals

An obvious factor that influences the formation of GO photonic structure is the aspect ratio ( $\alpha$ ), which is defined as the GO sheet diameter divided by its thickness. It is intuitively clear that the aspect ratio of GO sheets greatly affects their properties.[72,73] However, upon oxidation and sonication, the GO sheets are usually cut into small pieces and exhibit a wide size distribution.[74] To study the effect of GO size on the formation of its photonic structure, both GO-L and GO-S were prepared using a pH-assisted selective sedimentation technique proposed by Shi et al.[74] As shown in Figure 2.2, the AFM results indicate that the average sizes of GO-L and GO-S are about 2.4  $\mu\text{m}$  and 550 nm, respectively. The relative sizes between GO-L and GO-S were assessed by DLS *via* three different measurement modes (Figure 2.4). Interestingly, the GO-L aqueous

dispersion exhibits structural color under natural light. In contrast, the GO-S dispersion does not show a similar iridescent color at any concentrations. Moreover, it is commonly known that upon moderate sonication, the size of GO sheets is usually decreased. When the original GO-L aqueous dispersion that shows structural color was sonicated for 2 h (Branson 2510), its iridescent color would disappear. This confirms that the GO aspect ratio plays an important role in its photonic response to natural light.

The process of amphiphilic GO self-assembly is an interplay of enthalpy change ( $\Delta H$ ) and entropy change ( $\Delta S$ ) as shown in equation below:

$$(2.1) \quad \Delta G_{\text{self-assembly}} = \Delta H_{\text{self-assembly}} - T\Delta S_{\text{self-assembly}}$$

Studies[75,76] into the thermodynamic driving force for amphiphilic self-assembly into liquid crystal phases indicate that the entropic contribution plays a dominant role, while the enthalpy change is unfavorable in most cases. Onsager's theory[77] predicts that high aspect ratio particles can form liquid crystal phases above a critical volume fraction due to a net gain in entropy as the loss of orientational entropy is compensated by an increased translational entropy. Specifically, higher aspect ratio particles favor the formation of long-range liquid crystalline phases. Another possible reason for the GO aspect ratio effect could be the structural corrugation of GO sheets in solvent as the restoring force originated from bending the sheets is much weaker than that along the sheet. It was found that the degree of GO corrugated morphology in solvent could be further enhanced if its aspect ratio is increased.[78,79] This corrugated configuration

will significantly affect both the intra- and inter-molecular interactions of GO in suspension.[80]

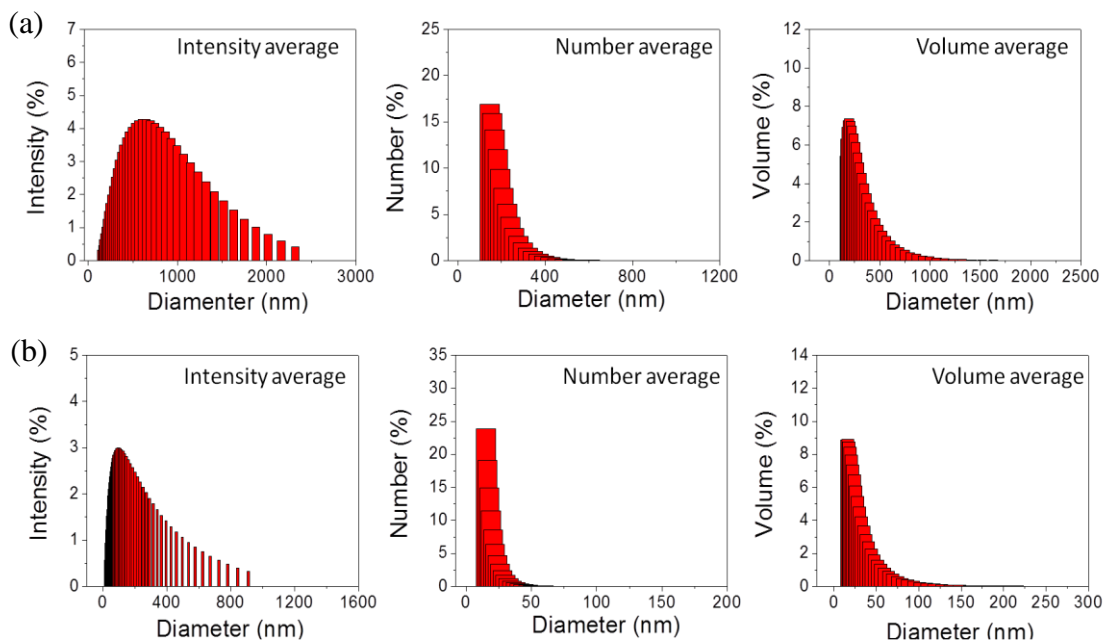


Figure 2.4 Dynamic light scattering (DLS) results of different sized GO aqueous dispersions *via* three different measurement modes: (a) GO-L and (b) GO-S. GO average diameter obtained from DLS is not a true size but rather the effective hydrodynamic diameter of an equivalent sphere described by the tumbling of the platelets. The relative sizes between GO-S and GO-L can be assessed by DLS.

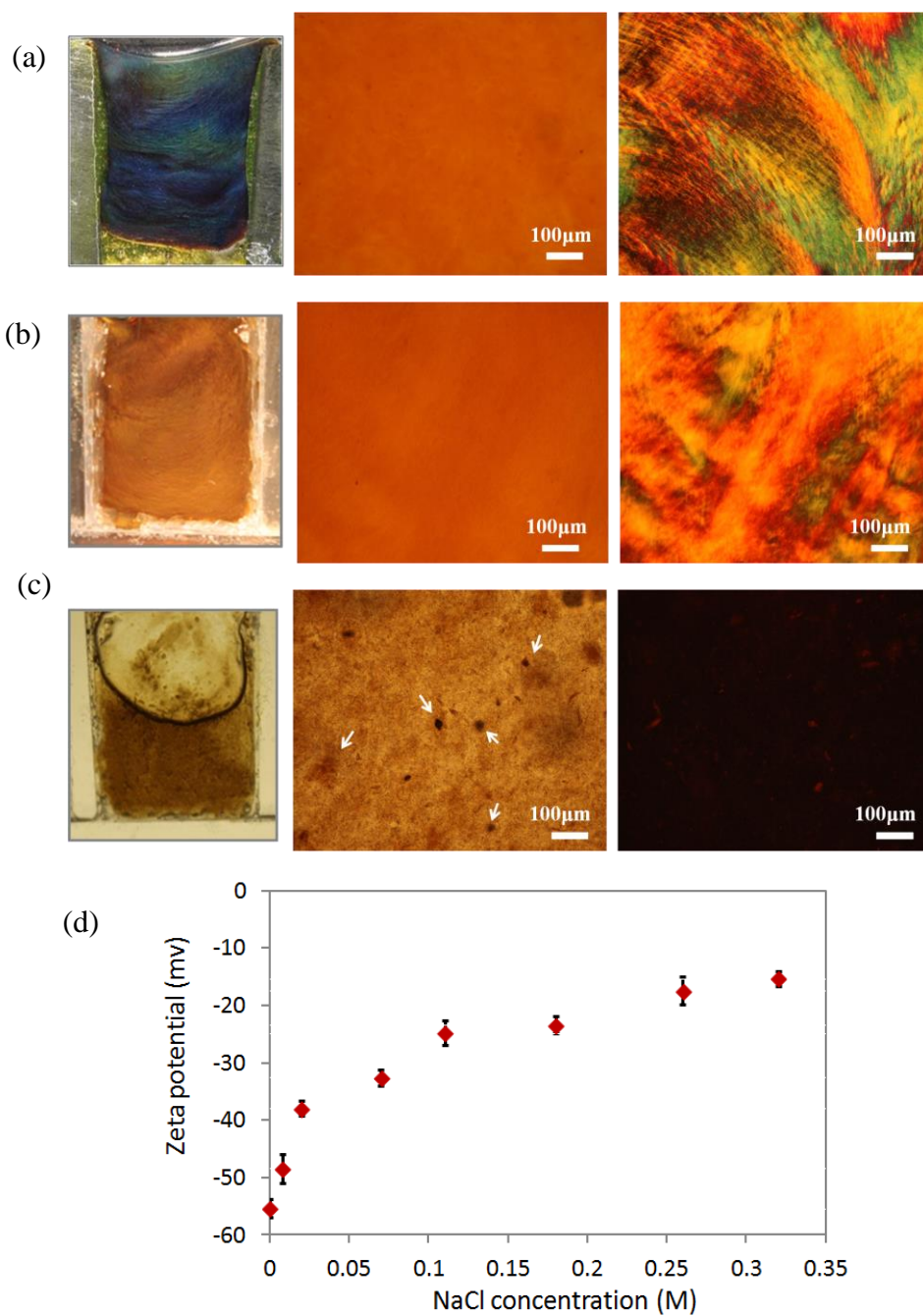


Figure 2.5 Optical images of GO-L aqueous dispersion at NaCl concentrations of (a)  $1.2 \times 10^{-5}$  M, (b) 0.008 M and (c) 0.3 M. (Left: photographical images; middle: OM images; right: cross-polarized OM images). The white arrows in (c) indicate GO-L aggregates. (d) Zeta potential of GO-L aqueous dispersion as a function of NaCl concentration.



To achieve iridescence in aqueous dispersion, well-exfoliated GO sheets with strong long-range electrostatic repulsion are required. Formation of photonic structures out of colloidal particles typically requires a delicate balance of long-range repulsive forces, such as electrostatic forces, and short-range attractive forces, such as van der Waals forces and  $\pi$ - $\pi$  interactions. If the long-range repulsive forces are not strong enough to overcome the short-range attractive forces, aggregation of colloidal particles or formation of lyotropic liquid crystal with small periodicity will inevitably occur. In the GO aqueous dispersion, long-range repulsive interactions are offered by the electrical double layers formed by the ionized oxygen functional groups.[81] Although GO sheets still contain a considerable portion of hydrophobic domains, attractive  $\pi$ - $\pi$  interactions and van der Waals forces can be effectively overcome by adjusting the long-range electrostatic repulsive forces.[81,82]

The chemical composition of GO plays an important role in tailoring the electrostatic interaction in aqueous dispersion. The increase of surface charge density will lead to an increase in the strength of the electrostatic repulsion against the attractive forces. The ratio of the aromatic and oxygenated domains can be easily tuned by the level of graphite oxidation.[83,84] The FTIR-ATR results of the GO-L (Figure 2.3(a)) indicate that oxidized species (hydroxyl, epoxy and carboxyl groups) exist on the GO-L surfaces. As shown in Figure 2.3(b), TGA in nitrogen was used to probe the oxygen functional group density on the GO-L surface. A mass loss of ~29 wt% is found at around 250 °C, and is attributed to the decomposition of labile oxygen-containing species. Below 160

°C, a mass loss of ~17 wt% is observed, corresponding to desorption of physically absorbed water. The XPS result of GO-L (Figure 2.3 (c, d)) shows that an atomic ratio of C/O is about 1.9. It suggests that the GO-L has a relatively higher density of oxygen functional groups compared to that of the GO reported in literature.[72,73,85] In contrast, we also prepared GO containing a lower density of oxygen functional groups by simply reducing the graphite oxidation time. In this case, no iridescent color was observed.

The colloidal interaction between GO sheets can be significantly influenced by the ionic strength, because the Debye screening length can be effectively increased by reducing the concentration of free ions surrounding GO sheets. It was reported that the electrostatic repulsion of the GO liquid crystal in water will decrease as the salt concentration increases.[63] As a result, more water is expelled from the GO interlamellar space with an accompanying reduction in d-spacing. Thus, ionic impurities in the GO dispersions should be sufficiently removed as it is a crucial factor influencing the formation of GO photonic structure. In our experiment, inductively coupled plasma-mass spectrometer (ICP-MS) testing shows that the concentration of the  $[\text{Na}^+]$  in GO-L photonic dispersion after sufficient washing is about  $1.2 \times 10^{-5}$  M. As shown in Figure 2.5(a), the original GO-L photonic liquid with a pH value of 4.5 shows a blue color if no NaCl is added. However, the structural coloration disappears when  $[\text{Na}^+]$  is beyond 0.008 M (Figure 2.5(b)). This is likely due to the screening of electrostatic interactions, and the consequent reduction of interlayer spacing at high ionic strength. Furthermore,

the OM results (Figure 4.5(b)) indicate that the GO-L dispersion at  $[\text{Na}^+] \approx 0.008 \text{ M}$  is stable without detectable precipitation, and its dispersion still exhibits birefringent behavior. As  $[\text{Na}^+]$  rises to 0.3 M, flocculated GO-L aggregates appear (Figure 2.5(c)), implying that an increasing salt content significantly weakens the repulsive force, thereby inducing phase segregation. Such an explanation is confirmed by tracking the zeta potentials of GO-L dispersions with the introduction of NaCl salt (Figure 4.5(d)). The absolute value of the zeta potential decreases from 56 to 15 mV as  $[\text{Na}^+]$  increases, and precipitation occurs due to minimized repulsive forces.

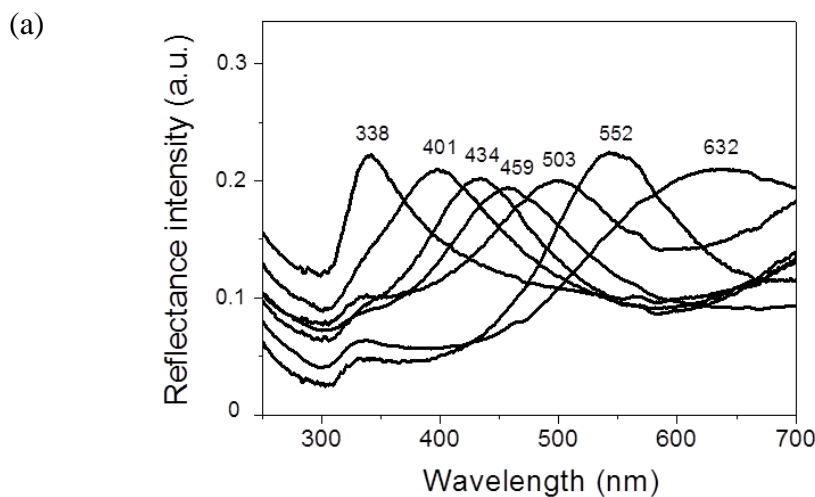


Figure 2.6 (a) Optical reflectance spectra and (b) visual images of GO-L dispersions of different structural colors. From left to right the weight fraction of GO-L is 0.91, 0.75, 0.67, 0.55, 0.51, 0.44 and 0.36 wt%, respectively. (c) Peak positions ( $\lambda_{\text{max}}$ ) of reflectance spectra versus GO-L wt%, demonstrating the dependence of iridescent color on GO-L concentration. (d) d-spacing exhibits a linear dependence on the inverse volume fraction ( $1/\phi$ ). D-spacing was calculated from  $d = \lambda_{\text{max}}/2\eta$ .

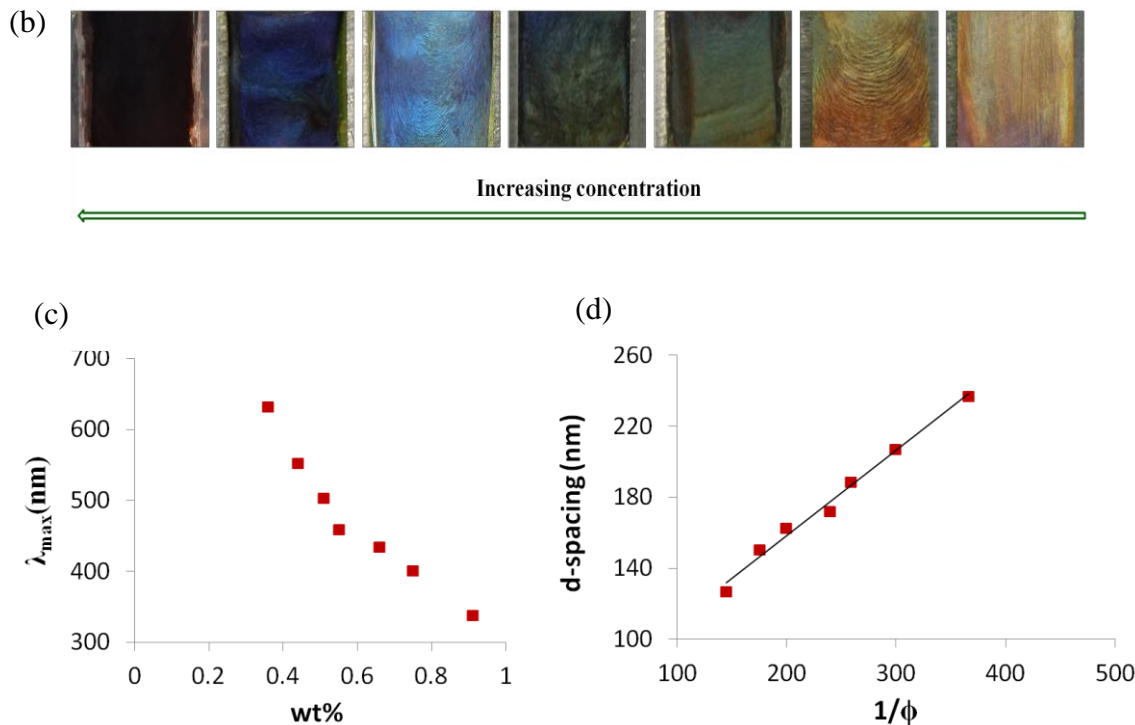


Figure 2.6 Continued.

### 2.3.3 Spectral and Structural Characterization of GO Photonic Crystals

A series of GO-L aqueous dispersions at different concentrations were prepared. As shown in Figure 2.6(a), the reflectance spectra of these solutions display peak shifting from violet to red as the concentration of GO-L was continuously reduced. The possible reason for the change of reflection peak width is likely related to the GO sheets d-spacing distribution range. At low GO concentration, the spacing is relatively larger. As GO concentration increases, the orientation of GO sheets will improve due to the “excluded volume” constrains of neighboring sheets, then resulting to a relatively

smaller reflection peak width. Photographic images (Figure 2.6(b)) of the solutions enclosed in the custom-made glass cells demonstrate the brilliant colors displayed by the suspended GO-L photonic crystals. GO-L concentration ranges from 0.36 to 0.91 wt%, resulting in a shift of the reflectance peak  $\lambda_{\max}$  from 632 to 338 nm (Figure 2.6(c)). According to the equation (i.e.,  $d = \lambda_{\max} / 2\eta$ ) proposed by Platz *et al.*,<sup>[86]</sup> we estimate that in water (refractive index  $\eta = 1.333$ ), a  $d$ -spacing of around 173 nm is required for iridescence to show blue color ( $\lambda_{\max} = 461$  nm). The evolution of interlayer spacing with respect to the inverse volume fraction ( $1/\phi$ ) is shown in Figure 2.6(d). Between  $0.27 \% < \phi < 0.69 \%$ , the  $d$ -spacing exhibits a linear dependence to the inverse of GO-L volume fraction. The thickness of GO-L sheets is estimated from the slope of the trend line to be 0.48 nm, which is close to the thickness of GO-L measured by AFM (0.9 nm), suggesting that GO-L sheets in aqueous dispersion are individually exfoliated.

As shown in Figure 2.7(a), the GO-L aqueous dispersion in gel form inside a centrifuge tube shows brilliant structural colors when exposed to white light, which is caused by Bragg refraction of long-range order of GO-L lyotropic suspension. Meanwhile, as the GO-L gel is transferred onto a glass slide (Figure 2.7(b, c)), its structural color can be clearly observed from different viewing angles. Moreover, the iridescent color of the GO-L gel changes from green to blue, and to black (Figure 2.7(d)), with increasing water evaporation time at room temperature. This occurs because of water evaporation from the GO-L gel that results in a decrease in interlamellar distance.

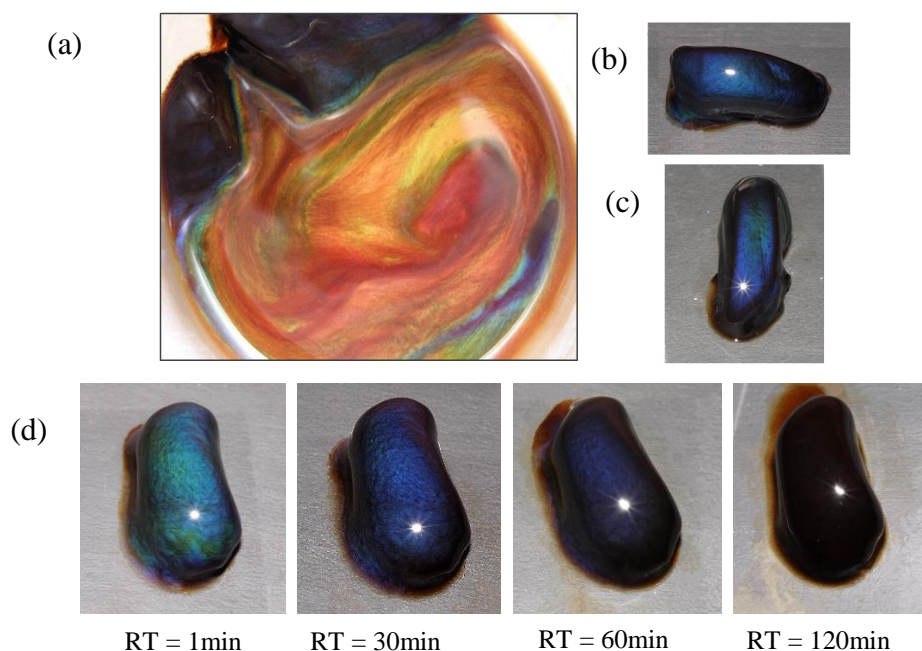


Figure 2.7 (a) Iridescent color of GO-L gel inside a centrifuge tube. (b) and (c) show the color of GO-L gel on a glass slide from different viewing angles. (d) Difference in structural colors of GO-L gel with increasing resting time (RT) at room temperature. All photographs were taken under white light.

SEM and SAXS were carried out to investigate the structure of the GO-L photonic dispersion. The local orientation of the GO-L photonic microstructure is shown in Figure 2.8. The GO-L photonic dispersion at different GO-L concentrations were quenched in liquid nitrogen and subsequently freeze-dried to remove water. The freeze-dried solid surfaces of GO-L photonic dispersion exhibit ordered alignment of GO-L sheets along their planar axes as marked by white lines. Similarly, GO-L ordered texture from the cross-sectional view was also characterized (Figure 2.9).

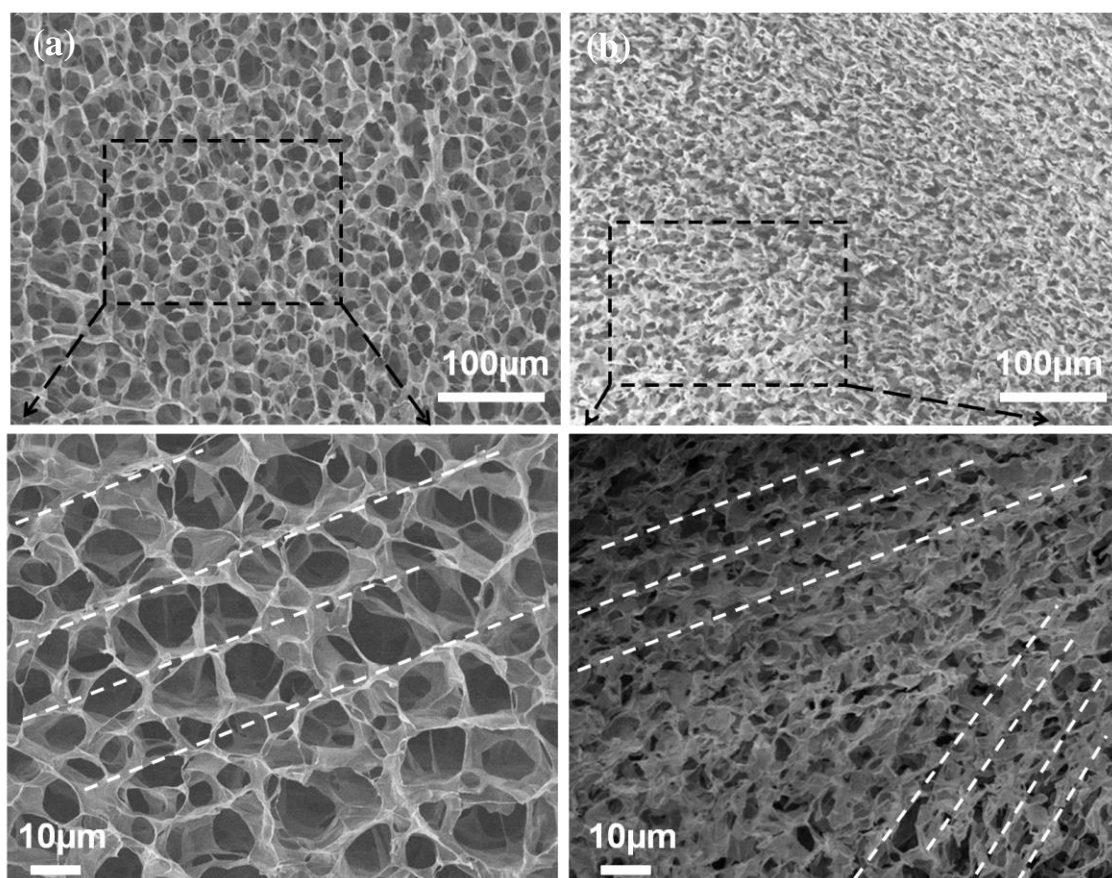


Figure 2.8 SEM images of surface of freeze-dried GO-L photonic structures at GO-L concentrations of (a) 0.36 wt% and (b) 0.91 wt%, respectively. The dashed white lines indicate the alignment direction of the GO-L sheets.

SAXS 2D diffractograms and scattering intensity profiles of GO-L aqueous suspension in the concentration range from 0.36 wt % to 1.3 wt% are shown in Figure 2.10. A strong broad first peak at scattering vector ( $q$ ) =  $0.078 \text{ nm}^{-1}$  and a weak broad secondary peak are observed for the GO-L suspension with a concentration of 1.3 wt%, suggesting that a loosely ordered smectic GO-L structure has been formed in this concentrated suspension. In the case of dilute GO-L suspension with concentrations

from 0.36 wt% to 0.69 wt%, no obvious first order diffraction peaks were detected ( $0.063 \text{ nm}^{-1} < q < 3.9 \text{ nm}^{-1}$ ). This is likely due to either the low level of lamellar positional order or the interlamellar spacing is too large to be detected.

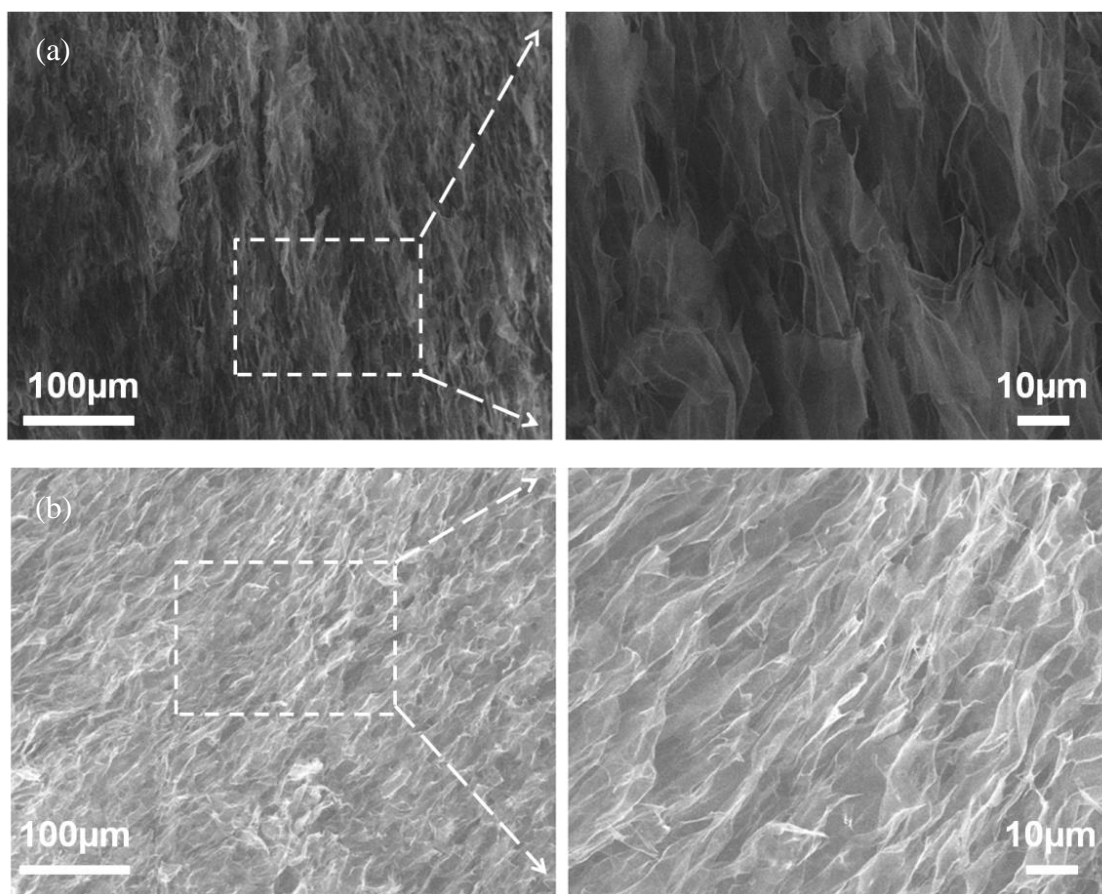


Figure 2.9 SEM images of cross-sectional view of freeze-dried GO-L photonic dispersions at various GO-L concentrations: (a) 0.36 wt% and (b) 0.91 wt%.



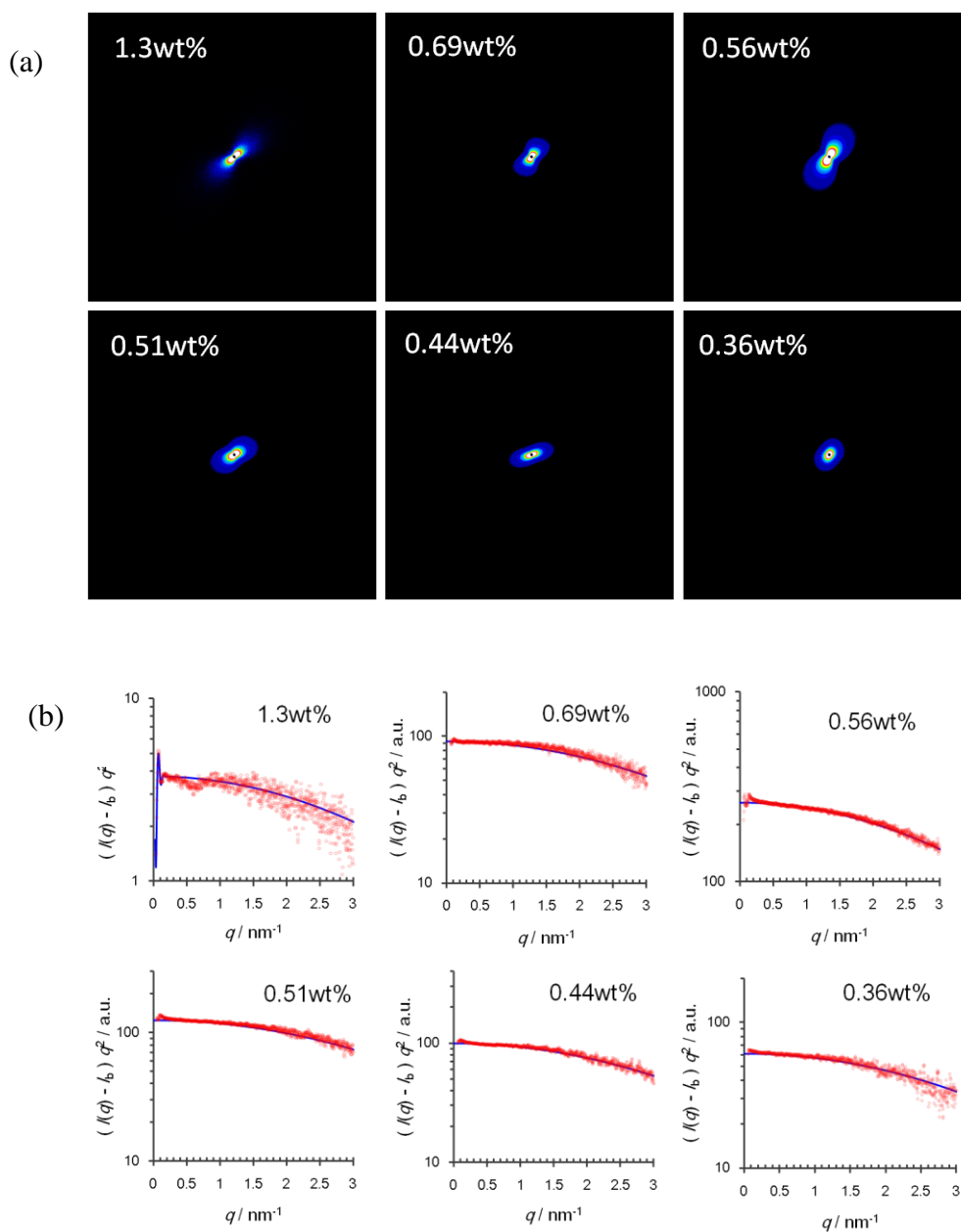


Figure 2.10 (a) SAXS 2D patterns of GO-L aqueous dispersions at various GO-L concentrations. (b) Profiles of scattering intensity  $(I(q)-I_b)q^2$  as a function of scattering vector  $q$  ( $q = 4\pi\sin\theta/\lambda = 2\pi/d$ ) for various GO-L dispersions, including measured data (red line) and calculated profile (blue line) based on the 1D paracrystal model. The numbers labeled on the patterns and profiles are the corresponding GO-L concentrations.

Colloidal self-assembly is an efficient and inexpensive approach for the fabrication of photonic crystal structures, especially for applications where the presence of small defects can be tolerated. The straightforward control of the GO photonic structure by changing GO concentration makes it attractive for many potential applications, such as tunable reflective filters and sensors. The versatility in decoration of chemical functionality on GO surfaces along with its tunable energy band gap offers opportunities for new exciting optoelectronic applications. For instance, magnetically or electrically responsive photonic materials based on GO hybrids will likely exhibit a controllable and reversible photonic response along the direction of external field for energy-efficient color display applications. These possibilities will soon be explored.

## **2.4 Conclusion**

A simple, yet effective self-assembly approach has been developed to fabricate photonic structure based on large-sized amphiphilic GO in aqueous dispersion. Compared to the commonly used sophisticated lithography techniques for the preparation of photonic structures, the present method is more suitable for engineering applications. The color reflection by GO photonic structure can be tuned across the entire visible spectrum through the adjustment of GO concentration. GO aspect ratio and the colloidal interactions between GO sheets are among the important factors that control the formation of GO photonic structure. The current study may significantly broaden the utilization of GO-based materials for advanced device applications.

## CHAPTER III

### SPRAY-COATED EPOXY BARRIER FILMS CONTAINING HIGH ASPECT RATIO FUNCTIONALIZED GRAPHENE NANOSHEETS\*

#### 3.1 Introduction

Because of their relatively low cost, light weight, flexibility, versatility and effectiveness, polymer nanocomposites have long been recognized to be ideal for barrier and protective coating and film applications, such as in food, beverages, pharmaceuticals, and electronics sectors.[87-90] The long-term effectiveness of barrier coatings and films in preventing product degradation is directly dependent upon a variety of factors, including their impermeability to corrosive gases, opacity to high-energy light, thermal stability, and mechanical integrity. Various strategies have been developed to fabricate high-performance, multi-functional polymer nanocomposite barrier films, such as microlayer coextrusion,[91] the Langmuir-Blodgett method,[92,93] spin-coating,[94] and layer-by-layer (LbL) assembly.[95,96] However, most of the above approaches require time-consuming sequential deposition processes or extensive energy consumption, which severely limit commercial attractiveness for large-scale production.

---

\*Reprinted with permission from “Spray-Coated Epoxy Barrier Films Containing High Aspect Ratio Functionalized Graphene Nanosheets” by Peng Li, Tsao-Cheng Huang, Kevin L. White, Spencer Hawkins, Riichi Nishimura, and Hung-Jue Sue.2015, RSC Advances, 5, 102633-102642. Copyright (2015) by Royal Society of Chemistry. <http://pubs.rsc.org/en/content/articlelanding/ra/2015/c5ra15363h#!divAbstract>

Nanoparticles with a 2-dimensional sheet-like geometry, such as natural montmorillonite (MMT) clay and other natural and synthetic analogs with layered structure, like laponite, goethite, and  $\alpha$ -zirconium phosphate (ZrP), have been widely studied as potential fillers to improve the barrier properties of various polymer matrices by forming a “tortuous pathway” to hinder transportation of gas molecules through the polymer.[95,97,98] However, there is still significant challenge to be able to exfoliate and uniformly disperse high concentrations of clay particles a polymer matrix.[2,99,100] Graphene and its derivatives have recently garnered significant attention due to their excellent material characteristics, such as large aspect ratio, impermeability to gases, high electrical and thermal conductivity, good thermal stability with respect to most polymers, and availability for diverse chemical modification approaches.[101-106] Several approaches have been developed to prepare polymer/graphene nanocomposites, and in many cases were found to exhibit not only greatly enhanced gas-barrier properties compared to polymers containing inorganic clays but also improved electrical and thermal conductivity when properly dispersed in a polymer matrix.[107,108] In addition to gas barrier applications, graphene-based materials could potentially be used as molecular gas filters,[109] metal protection layers to prevent corrosion,[110,111] effective surface lubricants,[112,113] and solvated ion separation membranes.[114]

In general, large-scale graphene-based polymer nanocomposites used for barrier properties may be prepared by two approaches. The first is the direct transfer of a few layers of large-size graphene or its derivatives onto a polymeric substrate. A major

challenge with this route is to minimize structural defects during the transfer process.[115,116] The second approach is to disperse the graphene-based filler into a polymer matrix. This approach is simpler and better suited for large-scale industrial applications, but it suffers from limitations in pre-processing steps to effectively exfoliate graphene without compromising intrinsic properties or reduction in size and aspect ratio during preparation. One penalty associated with achieving a high level of exfoliation and good dispersion of nanofillers in a polymer matrix is that there may be an associated increase in viscosity that will hinder processability, particularly at high nanofiller concentrations. Here, we adopt a simple spray coating approach to prepare high-quality, flexible epoxy barrier films based on modified graphene (MG) in epoxy.[117] This method allows for the preparation of nanocomposites containing a large volume fraction of MG without compromising processability. The high aspect ratio MG nanosheets were individually exfoliated and showed liquid-crystalline order when dispersed in an epoxy pre-polymer at high concentrations. After curing, the epoxy/MG nanocomposite films show significantly improved gas barrier properties, along with good electrical conductivity and thermal stability. Implication of the present findings on the fabrication of high-performance barrier films with multifunctionality is discussed.

## **3.2 Experimental**

### **3.2.1 Materials**

Potassium permanganate ( $\text{KmnO}_4$ ), barium sulfate ( $\text{BaSO}_4$ ), and sodium nitrate ( $\text{NaNO}_3$ ) were purchased from Aldrich. Bisphenol-F epoxy (EPON 862) and aromatic diamine curing agent (Epikure W) were purchased from Momentive. Graphite (SP-1) was donated by Bay Carbon Inc. Graphene and its derivatives may be an irritant to eyes, skin or causes respiratory reaction.  $\text{H}_2\text{SO}_4$ ,  $\text{KmnO}_4$ , and  $\text{H}_2\text{O}_2$  could cause severe burn from direct contact. Protection against inhalation and skin contact can be achieved by wearing protective clothes and face mask during use of these chemicals.

### **3.2.2 Synthesis of Modified Graphene**

Graphene oxide (GO) was synthesized and purified according to the method described in Charter II. The GO suspension prepared above was treated with sodium dodecyl benzene sulfonate (SDBS) surfactant by gently stirring 70 mg GO in 140 mL aqueous solution containing 1 wt% SDBS for 4 h. Chemical reduction was carried out by adding 70  $\mu\text{L}$  of hydrazine. The reaction mixture was heated to  $80^\circ\text{C}$  for 12 h with mechanical stirring to obtain reduced GO (rGO). Separately, 3 g of nitroaniline was dissolved in 140 mL acetonitrile solvent to achieve a homogenous solution, following by an addition of 140 mL rGO aqueous solution (0.5 mg/mL). Additionally, 3 mL isoamyl nitrite was added dropwise under nitrogen atmosphere. The reaction mixture was heated

with stirring to 70°C for 12 h. Afterwards, the mixture was filtered under vacuum and washed with DI water and acetone several times. The resulting nitrobenzene functionalized graphene, designated as modified graphene (MG), was redispersed in acetone to reach a concentration of 0.5 mg/mL.

### **3.2.3 Preparation of Epoxy/MG Barrier Film**

Bisphenol-F epoxy (2.4 g EPON 862, Momentive) was dissolved in 5 mL acetone to form a clear solution. The epoxy solution was added dropwise to the MG dispersion (0.5 mg/mL), followed by stirring for 6 h. Then, 0.634 g of diethyltoluenediamine (Epikure W, Momentive) was added to the solution and homogenized by stirring. The solution of epoxy/MG in acetone was loaded into a spray-gun (Master Airbrush G444-SET and Royal Mini Air Compressor) and deposited onto a polyimide (PI) film (Apical, Kaneka). The PI substrate was sprayed multiple times to achieve desired final thickness of the barrier film. The spray-coated film was cured in an oven at 40°C for 1 h, 80°C for 1 h, 120°C for 2 h, and 180°C for 4 h.

### **3.2.4 Characterization**

Transmission electron microscopy (TEM) was performed using a JEOL 2010 high-resolution transmission electron microscope with accelerating voltage of 200 kV. X-ray diffraction (XRD) patterns were obtained using a Bruker D8 Advanced Power X-ray diffractometer with Cu-K $\alpha$  incident radiation ( $\lambda=1.5418 \text{ \AA}$ ). Fourier transform infrared

spectroscopy under attenuated total reflectance mode (FTIR-ATR) was performed using a Nicolet Avatar 360. Optical micrographs (OM) were collected using an Olympus BX60 microscope. Tapping-mode atomic force microscopy (AFM) was carried out with a Digital Instruments Nanoscope AFM system. Thermogravimetric analysis (TGA) was carried out using a Q500-TGA from TA instruments. Grazing-incidence small-angle X-ray scattering (GISAXS) experiments were performed using a Rigaku S-Max 3000 unit at the University of Houston. Data were collected with a grazing incidence angle of  $0.05^\circ$ . The dynamic mechanical behavior was measured using an ARES-G2 (TA Instruments). The oxygen transmission rate (OTR) of the films was evaluated using a MOCON OX-TRAN 2/21 in accordance to ASTM D3985 at Dow Chemical. Small-angle X-ray scattering (SAXS) experiments were performed at the Japan Synchrotron Radiation Research Institute (JASRI) Spring-8 facility located in Hyogo, Japan. The scattering intensity is reported as a function of a scattering vector,  $q$ , which is defined as  $q = (4\pi/\lambda) \sin \theta$ , where  $\lambda = 0.07$  nm is the wavelength of the X-ray and  $2\theta$  is the angle between the incident X-ray beam and the scattered X-rays.

### **3.3 Results and Discussion**

#### **3.3.1 Preparation and Characterization of Modified Graphene in Epoxy**

Direct deposition of large-scale, defect-free sheets of graphene on desirable polymeric substrates for greatly improved barrier properties remains a major challenge. One strategy for fabricating high-performance graphene-based barrier films is to utilize



high-quality graphene derivatives, such as GO, rGO, and MG, which are more easily exfoliated and dispersed in organic solvents and in polymer matrices. In this work, exfoliated epoxy/MG films were prepared *via* a simple and efficient spray-coating method (Figure 3.1). MG was prepared by chemically modifying GO precursors with nitroaniline. GO sheets were individually dispersed in aqueous suspension with a thickness of 0.9 nm (Figure 3.2a), and showed excellent stability at a concentration of 5 mg/mL (Figure 3.2b). Lyotropic liquid crystalline behavior was observed by cross-polarized OM for GO suspensions at 10 mg/mL (Figure 3.2c, d), which indicates the presence of an ordered mesophase. SAXS measurements carried out on aqueous dispersions of GO at 1.3 wt.% showed first and second order peaks corresponding to smectic order with inter-layer d-spacing of  $\sim 80$  nm (Figure 3.2e). We previously used this approach as an efficient method to disperse multi-walled carbon nanotubes (MWCNT) in organic solvents and epoxy without causing significant physical damage to damage to the MWCNT[117]. The MG was well dispersed in acetone at 0.7 mg/ml without any visual evidence of aggregation or precipitation after 2 days of storage (Figure 5.3a). AFM measurements show that MG flakes are individually exfoliated and have an average thickness and diameter of  $\sim 1.1$  nm (Figure 3b, c) and  $1.7 \mu\text{m}$  (Figure 3.3d), respectively. The diameter of an irregular sheet was defined as a circular diameter with an area equivalent to the area of an irregular MG. The aspect ratio of MG, defined as the length to thickness ratio, is about 1500.

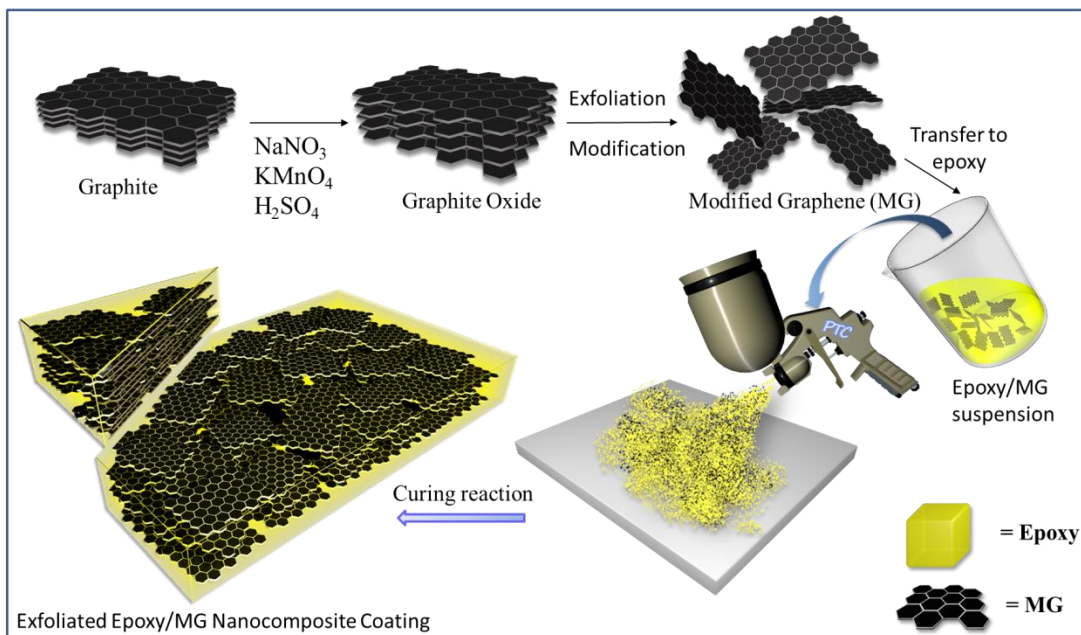


Figure 3.1 Schematic of epoxy/MG nanocomposite films preparation.

The chemical composition of MG was characterized by FTIR-ATR and TGA (Figure 3.4). The FTIR-ATR measurements of the GO show characteristic peaks at  $3500\text{ cm}^{-1}$ ,  $1220\text{ cm}^{-1}$ , and  $1720\text{ cm}^{-1}$ , which are assigned to stretching of O-H, C-O, and C=O functionalities, respectively, and indicate that the presence of oxygen-functional groups attached to surface. The MG shows C-N stretching at  $852\text{ cm}^{-1}$ , and  $\text{NO}_2$  asymmetric and symmetric stretching at  $1520\text{ cm}^{-1}$  and  $1285\text{ cm}^{-1}$ , respectively, which are consistent with the presence of nitrobenzene groups. The XRD pattern of the GO exhibits a diffraction peak at  $2\theta = 10.8^\circ$ , which correspond to an interlayer spacing of  $0.82\text{ nm}$  (Figure 3.4 c). After chemical reduction treatment, the interlayer distance of the rGO decreases to  $0.35$

nm ( $2\theta = 25.6^\circ$ ) indicating that a significant amount of the oxygen species on GO were removed after chemical reduction.

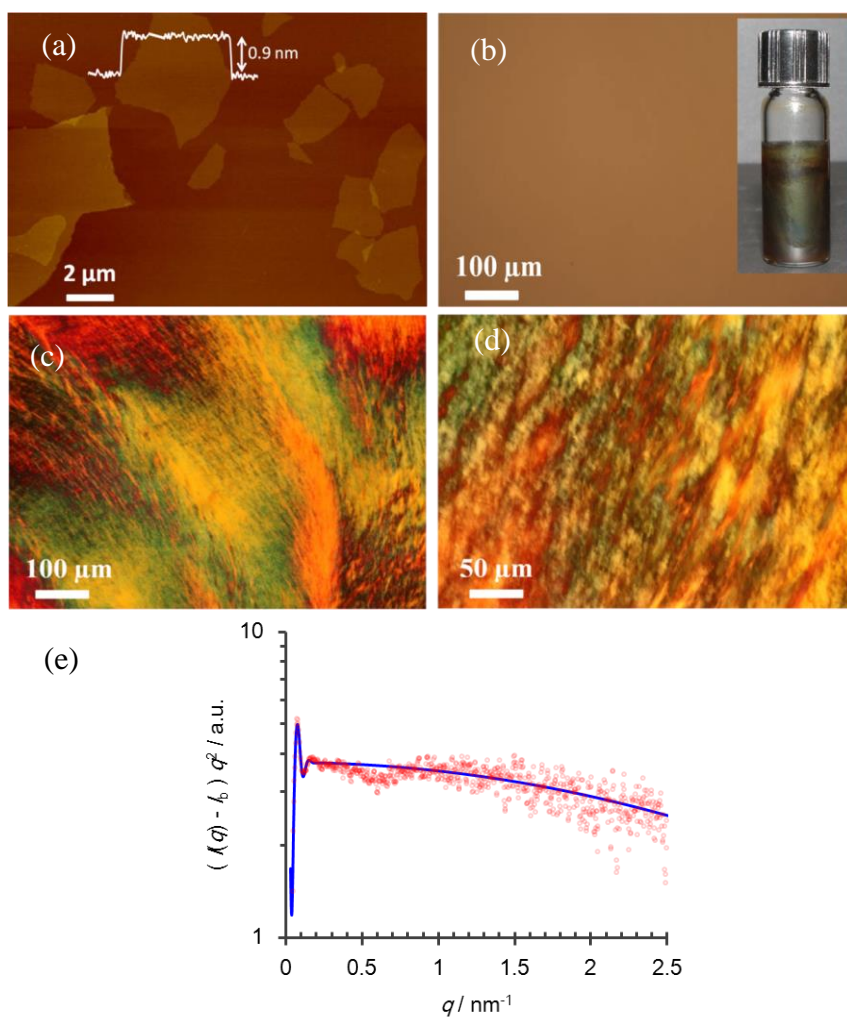


Figure 3.2 Images of GO viewed using (a) AFM, (b) OM, (c, d) cross-polarized light OM, and (e) SAXS of GO aqueous dispersion. Profiles of scattering intensity  $(I(q) - I_b)q^2$  as a function of scattering vector  $q$  ( $q = 4\pi\sin\theta/\lambda = 2\pi/d$ ) for 1.32 wt.% GO dispersion including measured data (red line) and calculated profile (blue line) based on the 1D paracrystal model. Inset in (b) is photograph of GO aqueous suspension.

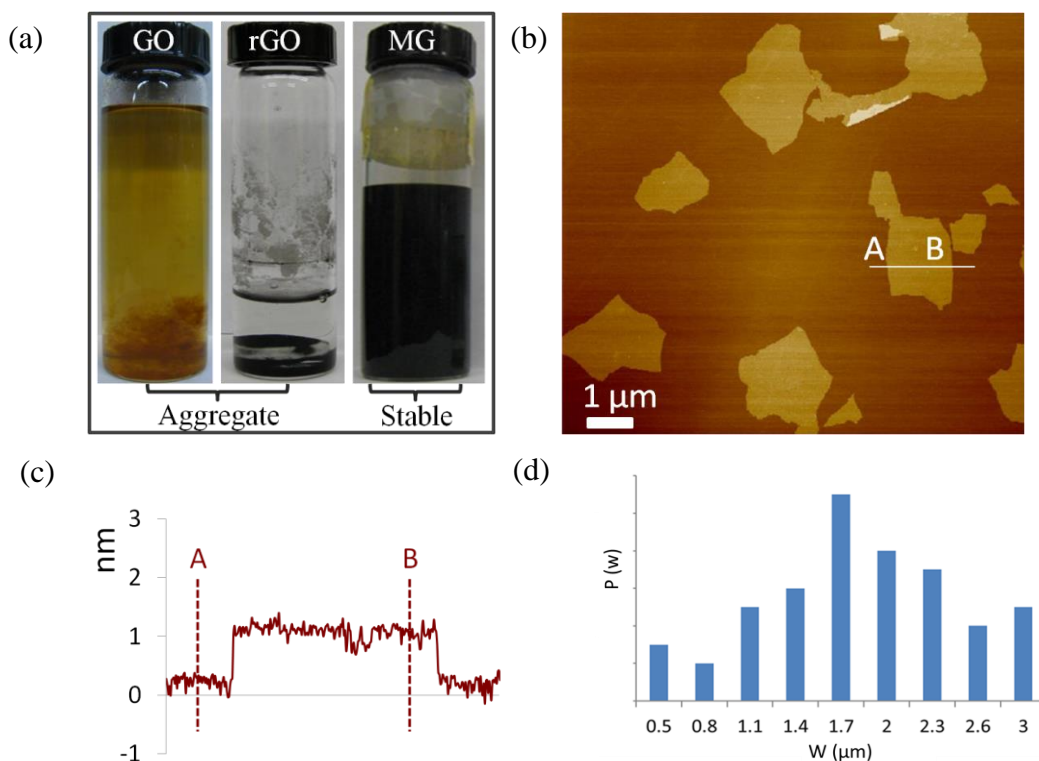


Figure 3.3 (a) Photograph of GO, rGO and MG in acetone having a concentration of 0.7mg/mL. (b) Tapping-mode AFM image, (c) height profile, and (d) size distribution of MG.

The XRD pattern of the MG shifts to  $2\theta = 8.4^\circ$  corresponding to a d-spacing of 1.1 nm, suggesting that the nitrobenzene functional groups are tethered on the MG surfaces. The degree of functionalization was estimated using TGA (Figure 3.4(b)). GO shows a mass loss of  $\sim 27.1$  wt% at around  $220^\circ\text{C}$ , which is attributed to the decomposition of oxidized species. There is no obvious weight loss after hydrazine reduction up to  $220^\circ\text{C}$ . The final weight loss values of GO, rGO and MG at  $700^\circ\text{C}$  were 57.8 wt.%, 20.3 wt.% and 38.2 wt.%, respectively. The weight fraction of nitrobenzene functional groups in MG is 17.9%, which is equal to the difference between 38.2% and 20.3%. It is estimated

that there is approximately 1 nitrobenzene functional group for every 47 carbon atoms in graphene.

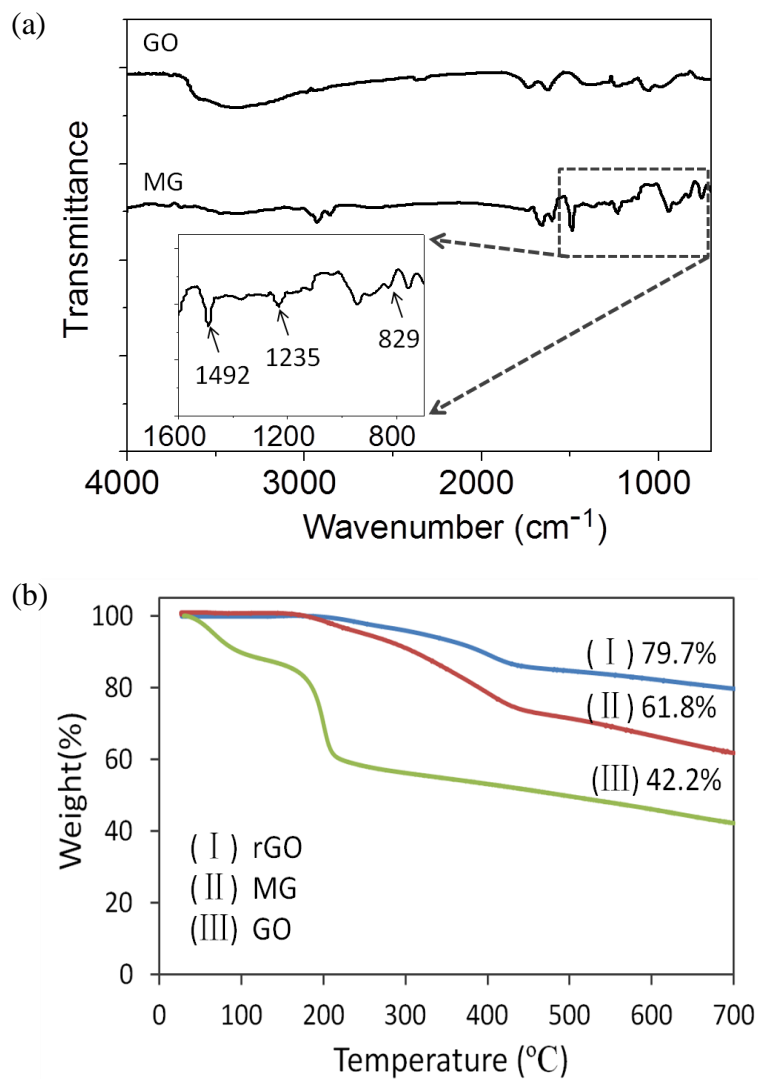


Figure 3.4 (a) FTIR-ATR spectra of GO and MG; inset shows the details of wavenumber region from 1600 to 700 cm<sup>-1</sup>. (b) TGA results of GO, rGO and MG. (c) XRD of graphene oxide (GO), reduced graphene oxide (rGO) and modified graphene (MG).

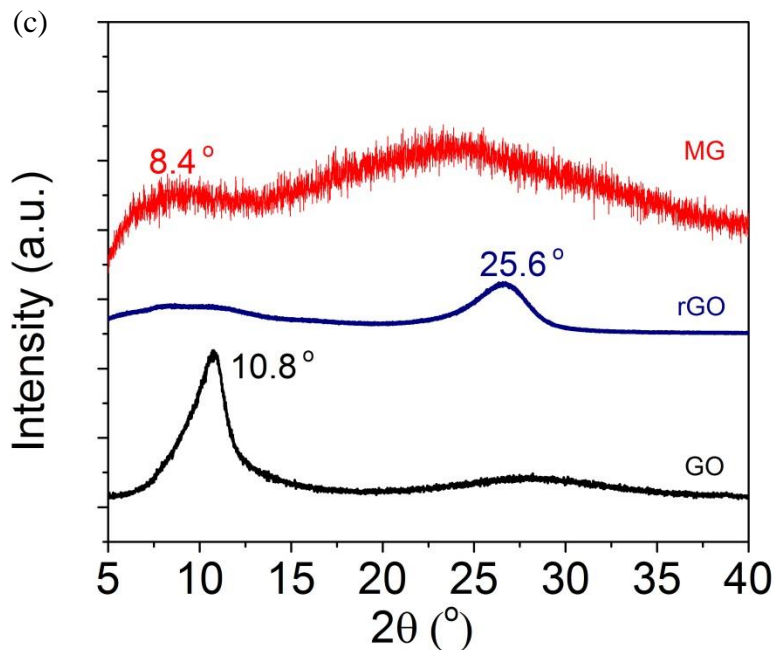


Figure 3.4 Continued.

A high degree of exfoliation is necessary to be benefitted from the high aspect ratio nanofillers in polymer nanocomposites, particularly for barrier properties applications. The degree of exfoliation in epoxy/MG was evaluated using XRD (Figure 3.5a). The pristine graphite exhibits a diffraction peak at  $2\theta=26.5^\circ$ , which corresponds to a basal layer d-spacing of 0.34 nm. Epoxy/MG nanocomposites were prepared with concentration from 0.6 to 7.5 vol.%. For systems containing up to 3.6 vol.% of MG, the XRD patterns show no new peaks. Only a broad hump centered at  $2\theta=19^\circ$  is observed due to the amorphous epoxy structure, which indicates the MG remains well exfoliated in the cured epoxy matrix. TEM micrographs confirm that for concentrations as high as 3.6 vol.%, the MG remains exfoliated and well dispersed (Figure 3.5c). However, when

the MG content was increased to 7.5 vol.%, there is a weak diffraction peak at  $2\theta=7.9^\circ$ , which corresponds to an interlayer d-spacing of 1.12 nm, suggesting some re-stacking of the dispersed MG sheets.

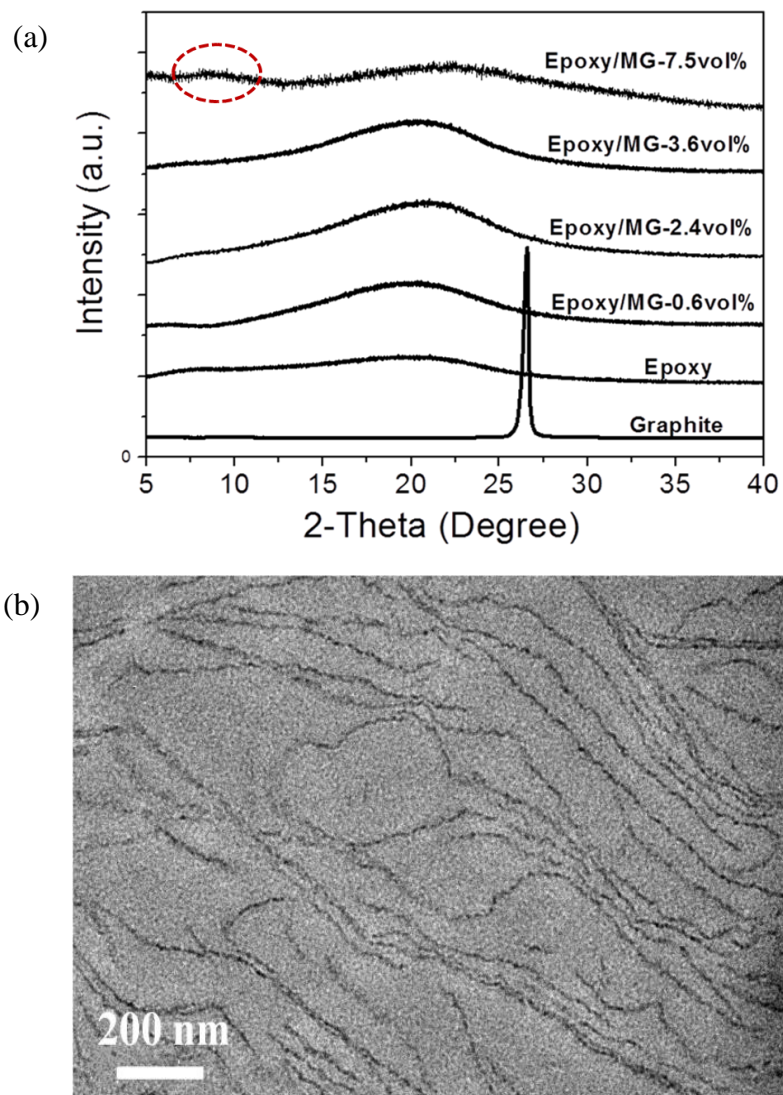


Figure 3.5 (a) XRD results of cured neat epoxy, graphite, and epoxy/MG films at various MG concentrations. TEM of cross-sectional epoxy/MG films at different MG loading: (b) 2.4 vol%, (c) 3.6 vol%.



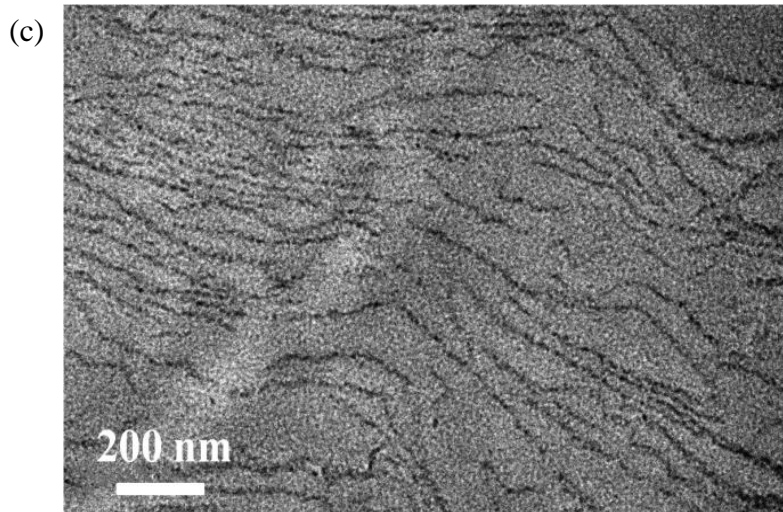


Figure 3.5 Continued.

High-quality epoxy/MG nanocomposites on a polyimide substrate were prepared by spray-coating and show good mechanical flexibility after curing (Figure 3.7a). The dynamic mechanical behavior (Figure 3.6) shows that the storage moduli at 25 °C of neat epoxy and epoxy/MG (1 vol.%) bulk samples are 1.1 and 1.3 Gpa, respectively. Incorporation of MG appears to lower the  $T_g$  of the neat epoxy which may be attributed to the side reactions between the MG surface-tethered carboxylic groups and the epoxy monomers. The surface quality of the films are of significant importance to gas barrier properties, and was analyzed using OM. Films prepared with up to 3.6 vol.% MG show uniform surface morphology (Figure 3.7b-d). At higher MG loadings, void and air bubble formation within the films become inevitable (Figure 3.7(d, e)), which are likely caused by high viscosity of epoxy/MG and incomplete removal of solvent before curing. The epoxy/MG nanocomposite films at 7.5 vol.% still exhibit good mechanical



flexibility. The evaporation of solvent initially takes place on the surface of the coating precursor, thus a concentration gradient will exist within the coating. Since cross-linking reactions of the coatings can drive up the viscosity significantly, it is possible for the coating experiences a rapid increase in viscosity and potentially to act as barrier for solvent to evaporate. Solvent evaporation rate and kinetics of curing reactions are believed to be among the key factors responsible for the rough surface morphology.

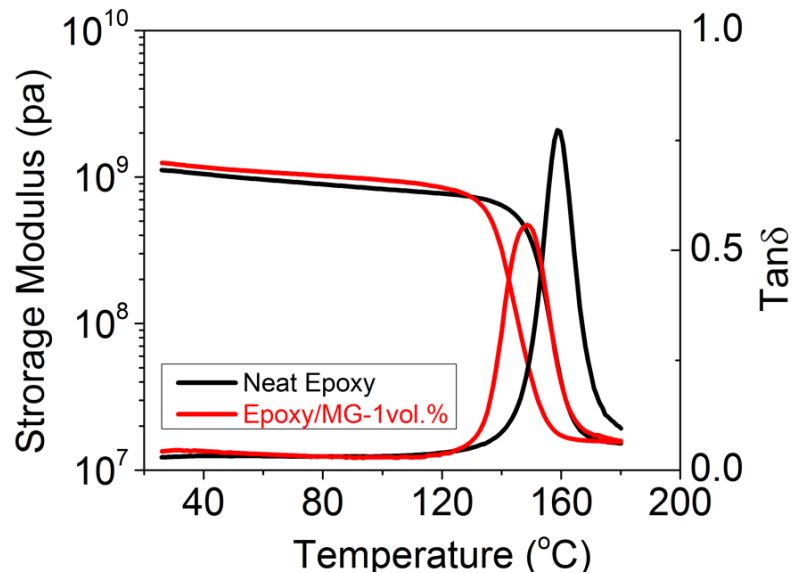


Figure 3.6 DMA of neat epoxy and epoxy/MG (1vol.%) bulk samples.

High aspect ratio nanoplatelets have a tendency to form a long-range liquid crystalline phase at relatively low concentrations, but the order is seldom preserved after curing in thermosetting materials. We recently used a similar spray-coating approach to deposit monoamine oligomer-modified ZrP nanoplatelets in epoxy, and observed a long

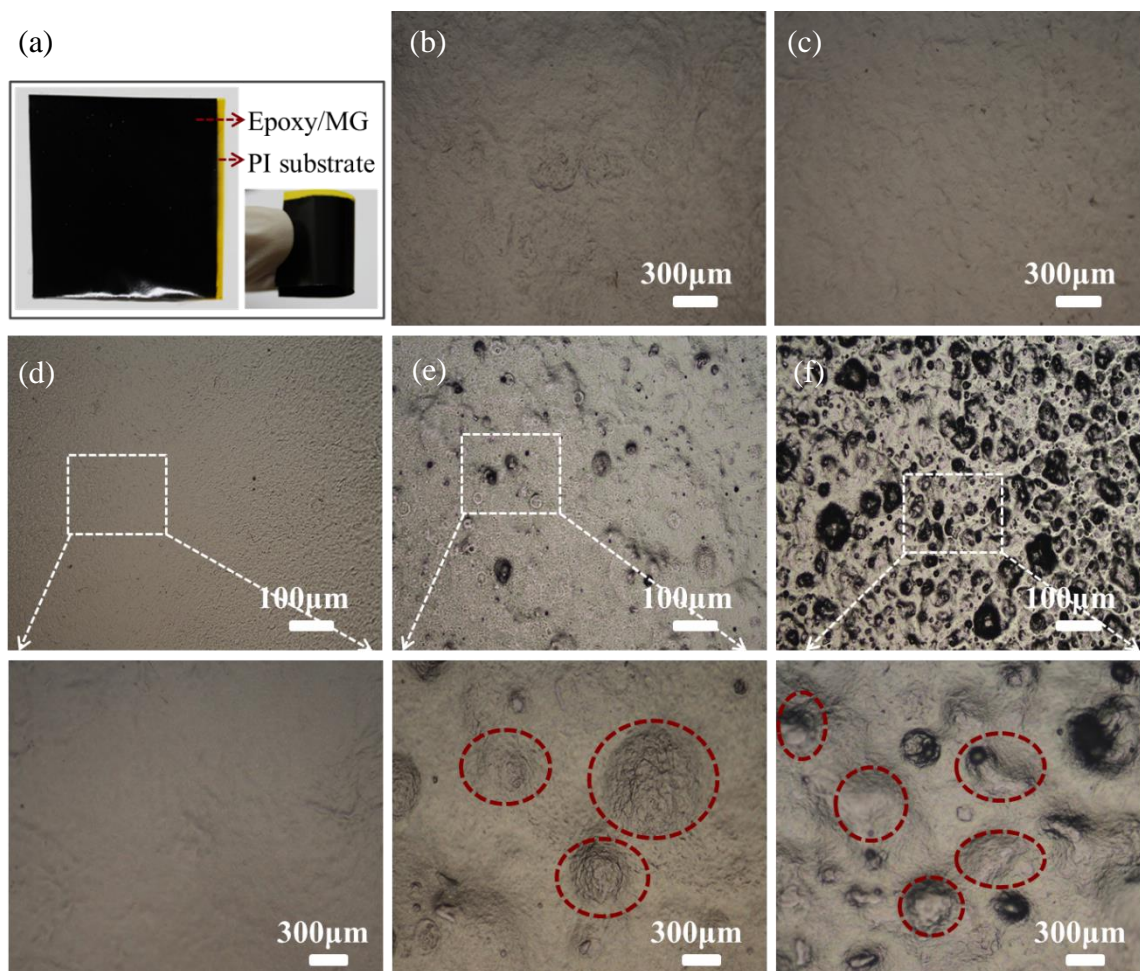


Figure 3.7 (a) Photograph of epoxy/MG (3.6 vol.%) film on PI substrate. OM images of epoxy/MG film surface at various MG concentrations: (b) 0.6 vol%, (c) 2.4 vol%, (d) 3.6 vol%, (e) 5.5 vol%, and (f) 7.5 vol%.

range smectic order after curing. A number of key properties, particularly barrier performance and processability, are benefitted from this type of highly aligned structure.[118,119] The microstructure of MG sheets in epoxy was characterized using OM and GISAXS. Prior to curing, the epoxy/MG (3.6 vol.%) suspension shows a strong birefringence (Figure 3.9), which indicates the presence of mesoscale liquid crystalline

order. The nature of long-range organization was probed at different concentrations using GISAXS (Figure 3.8). The GISAXS measurements did not show Bragg peaks corresponding to mesoscale lamellar organization, which indicates that the MG sheets were assembled in a nematic order.

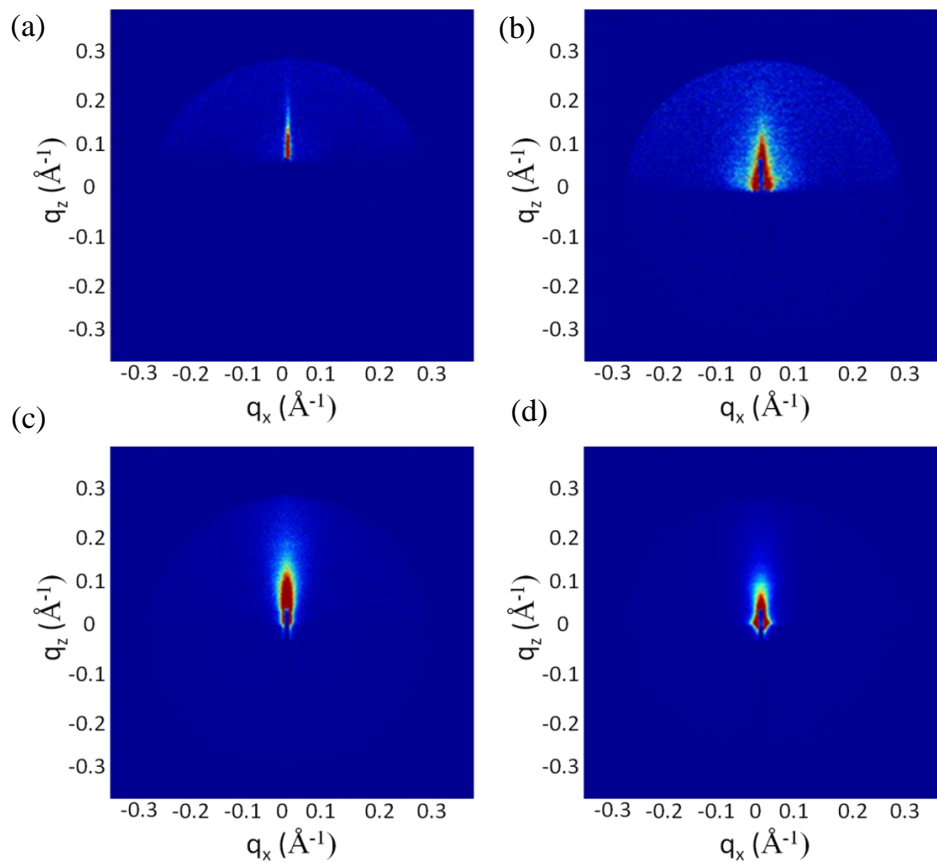


Figure 3.8 GISAXS 2D diffractogram of epoxy/MG nanocomposite films at (a) 0.6 vol. %, (b) 2.4 vol.%, (c) 3.6 vol.%, and (d) 5.5 vol.% ZrP. (e) GISAXS 1D diffractogram spectrum of epoxy/MG films at various concentrations.

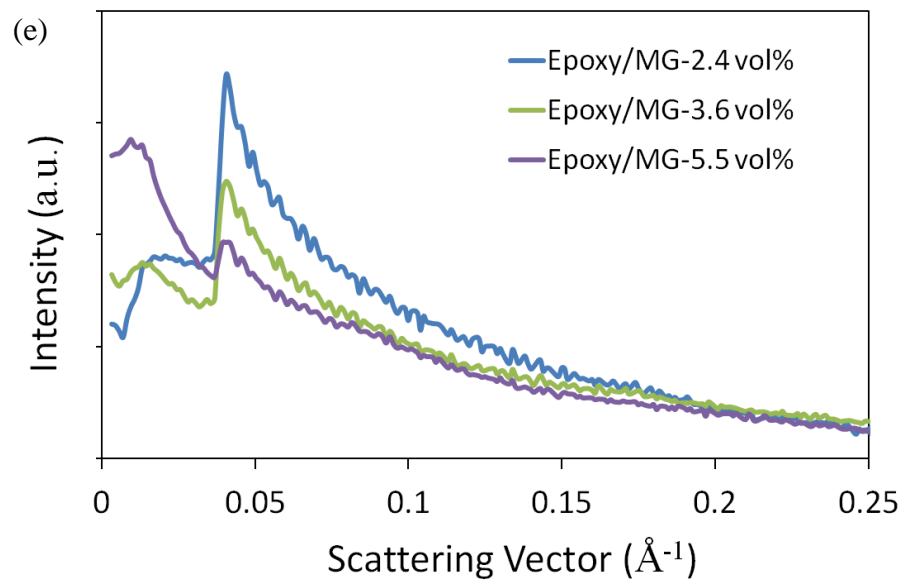


Figure 3.8 Continued.

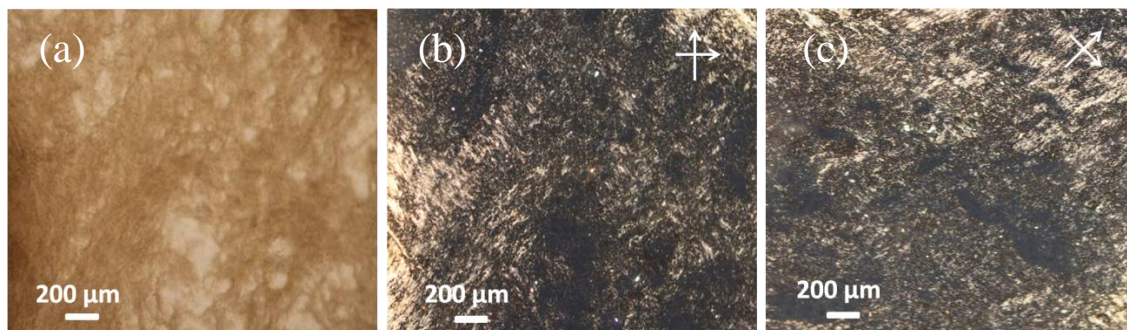


Figure 3.9 (a) OM and (b) cross-polarized light OM of epoxy/MG precursor (3.6 vol. %) before curing reaction.

### 3.3.2 Rheological Behavior of Epoxy/Modified Graphene Suspensions

The rheological behavior of the uncured precursor was characterized to provide insight into the influence of the long-range organization and inter-particle interaction on bulk response. The linear viscoelastic response was strongly dependent on shearing history shown in Figure 3.10(a, b), which is in contrast to our previous investigations of oligomer-modified nanoplatelets with smectic order in epoxy.[120] After loading the sample and allowing the normal force to equilibrate, the storage modulus,  $G'$ , which is a measure of solid-like response, shows a low-frequency plateau that generally indicates a mechanically percolated network. This type of response is typical of high aspect ratio nanoparticles at moderate and high concentrations. The loss modulus,  $G''$ , which describes the dissipative component of response, similarly appears consistent with an inter-connected particle network, but shows a minima and weak increase in the limit of low frequency. This type of behavior suggests a meta-stable microstructure and suggests that, based on the geometry of the filler used here, there is either an increased number of inter-connections with time, or a gradual mis-alignment of the MG sheets on long time scales. We previously modified MWCNTs with nitrobenzene functionalities, and found a transition in relaxation behavior that was attributed to a significant suppression in inter-particle attraction. After steady shear, the magnitude of  $G'$  and  $G''$  were significantly reduced. However, when the suspensions were subjected to large-amplitude oscillatory deformation, both  $G'$  and  $G''$  increased, suggesting either greater connectivity between aligned sheets or alignment of the director out of the flow direction. Changes in

alignment behavior dependent on the size of graphene sheet have been previously reported by Wallace. They demonstrated that large graphene sheets tend to give rise to entropic rearrangement of sheets to form long range liquid crystalline order. The transition from isotropic to nematic phase is due to increased translational entropy. The MG sheets used here have high aspect ratio and any change in orientation must involve a domain-level transition, which suggests a highly cooperative behavior.

The response of the suspension to large amplitude oscillatory deformation is shown in Figure 3.10c. Prior to shear, there is no clearly defined linear region in  $G'$ , but  $G''$  does show a broad region of linear response. At large strain amplitude,  $\gamma \approx 30\%$ , there is a minima in both  $G'$  and  $G''$ , and at larger strains, both components of shear moduli show strain-hardening behavior and reach a maxima. This type of non-linear viscoelastic response is unusual and rarely reported.[120,121] Hyun et al. [122] proposed a network model to account for various modes of non-linear viscoelastic behavior, and suggested that similar LAOS curves were associated with the presence of both attractive and destructive processes that are enhanced by straining. The remarkable feature of the LAOS response here is that despite the substantial decrease in both  $G'$  and  $G''$  after shearing, which is consistent with the SAOS results, their magnitude and position are nearly identical at large strain amplitudes. This suggests that there is a unique microstructural state introduced by large amplitude deformation, and that it is reversible. The reversible nature of the microstructure is supported by steady shear measurements. More detailed work is still necessary to explicitly identify the mechanisms responsible

for the unique behavior observed here, particularly to separate local interaction between MG sheets from longer-range changes in orientation. We modified MWCNTs using nitrobenzene functionalities with similar degree of functionalization compared to the MG used here. The rheological results suggest that despite the observed excellent exfoliation and dispersion, there remains significant interaction between MG nanoplatelets, which stands in contrast with our prior reports on exfoliated MWCNTs with similar surface treatment. The difference in rheological response is more likely a consequence of particle geometry rather than surface chemistry. Both steric interaction between oligomer modified nanoparticles and entropic effects to drive particle orientation significantly depend on nanoparticle geometry.

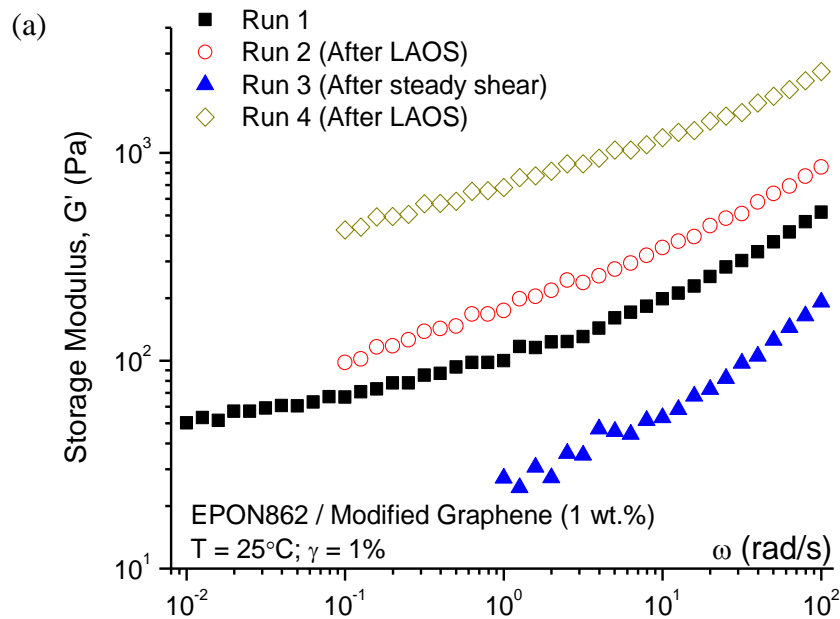


Figure 3.10 The response of the epoxy/MG suspension to (a, b) linear viscoelastic response, and (c) large amplitude oscillatory deformation.

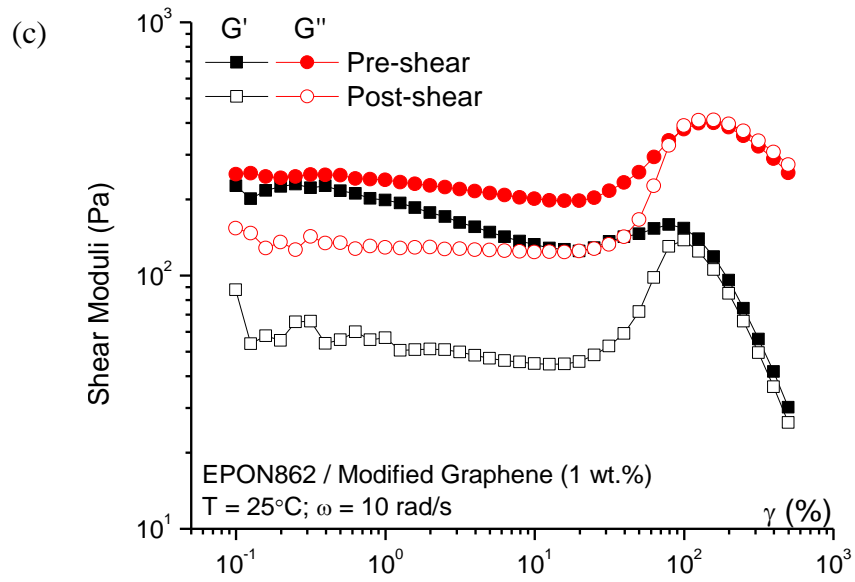
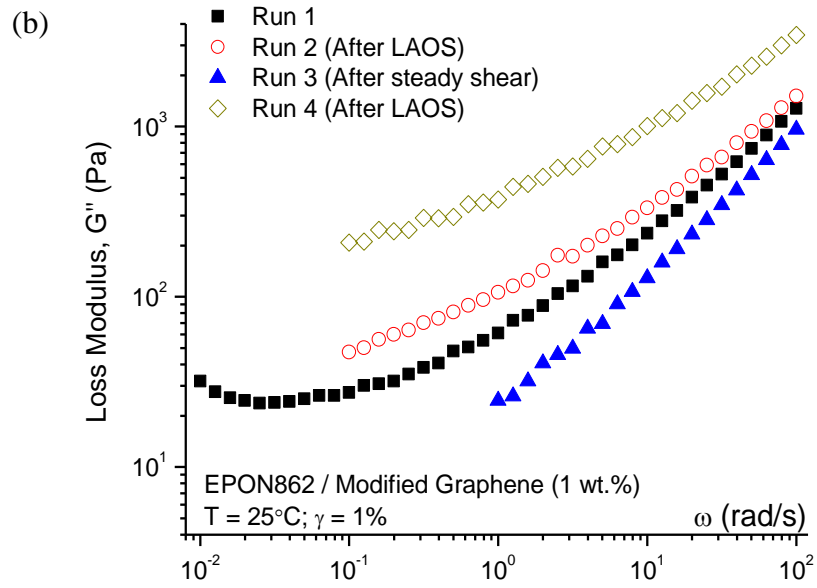


Figure 3.10 Continued.



### 3.3.3 Gas Barrier Properties

The oxygen permeability of epoxy/MG nanocomposite films spray-coated on PI substrates was characterized in accordance to ASTM D3985 (Figure 3.11). Compared to the neat epoxy, the epoxy/MG (3.6 vol.%) nanocomposite films, which are only 21  $\mu\text{m}$  thick, show nearly an order of magnitude decrease in oxygen permeability. At a higher concentration, the barrier performance is reduced, which is likely due to the presence of void defects resulting from incomplete removal of solvent or trapped air bubbles before curing.

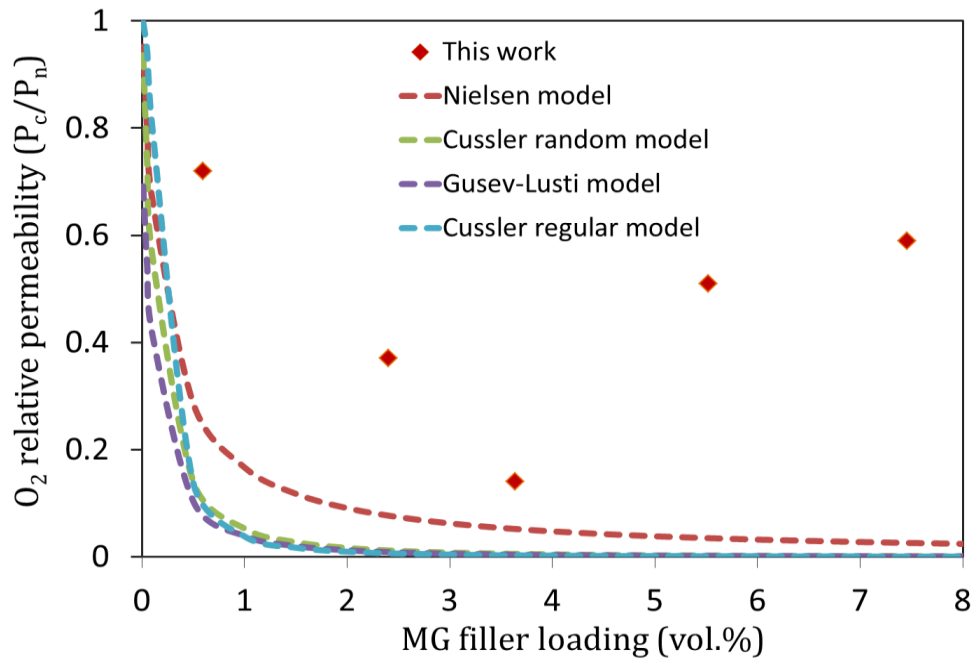
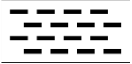


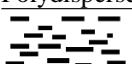



Figure 3.11 Oxygen relative permeability plots of epoxy/MG ( $P_C$ ) at various MG loadings compared to the pristine epoxy ( $P_n$ ). Predicted values from various models are also included for comparison.

Table 3.1 List of permeability models for polymer nanocomposites.

Model	Flake Size, Array Type	Model Dimension	Equation
Nielsen	Monodisperse, Regular Array 	2D	$\frac{P}{P_0} = \frac{1 - \phi}{1 + \frac{\alpha}{2}\phi}$
Cussler Random Array Monodisperse Flakes	Monodisperse, Random Array 	2D	$\frac{P}{P_0} = \frac{1 - \phi}{[1 + \frac{\alpha}{3}\phi]^2}$
Cussler Ideal Regular Array	Monodisperse, Regular Array 	2D	$\frac{P}{P_0} = \left(1 + \frac{\frac{1}{4}\alpha^2\phi^2}{1 - \phi}\right)^{-1}$
Gusev-Lusti	Polydisperse, Random Array 	3D	$\frac{P}{P_0} = e^{-\left(\frac{\alpha\phi}{3.47}\right)^{0.71}}$
Bharadwaj	Random, non-oriented 	2D	$\frac{P}{P_0} = \frac{1 - \phi}{[1 + \alpha\phi(2S + 1)/6]}$

Note: The Nielsen, Cussler and Bharadwaj models can be viewed as 3D models if the fillers are considered to be ribbons with infinite length. The order parameter  $S = -1/2$ , when the ribbons are normal to the membrane;  $S = 1$ , when the ribbons are parallel to the membrane surface;  $S = 0$ , when the ribbons are randomly oriented.

The barrier performance may be compared with existing models to provide some idea on the influence of alignment and aggregation on permeability. Several models used to predict barrier properties, such as those proposed by Neilson, Gusev-Lusti and Cussler, are included in Figure 3.11. The details of various barrier models are summarized in Table 3.1. More detailed information can be found in reviews by Picard and Takahashi et al. Most of the models assume that the nanoplatelets are aligned perfectly parallel to

the barrier film surface, which is not a realistic assumption for most nanocomposite materials, except for films prepared by sequential layer-by-layer deposition. The gas permeability of the epoxy/MG nanocomposites presented here is below the performance expected for individual, perfectly aligned sheets with aspect ratio  $\approx 1500$ . The difference in performance is likely due to non-uniform alignment and dispersion of the MG, and possibly also because of the wrinkled morphology of the MG nanosheets.

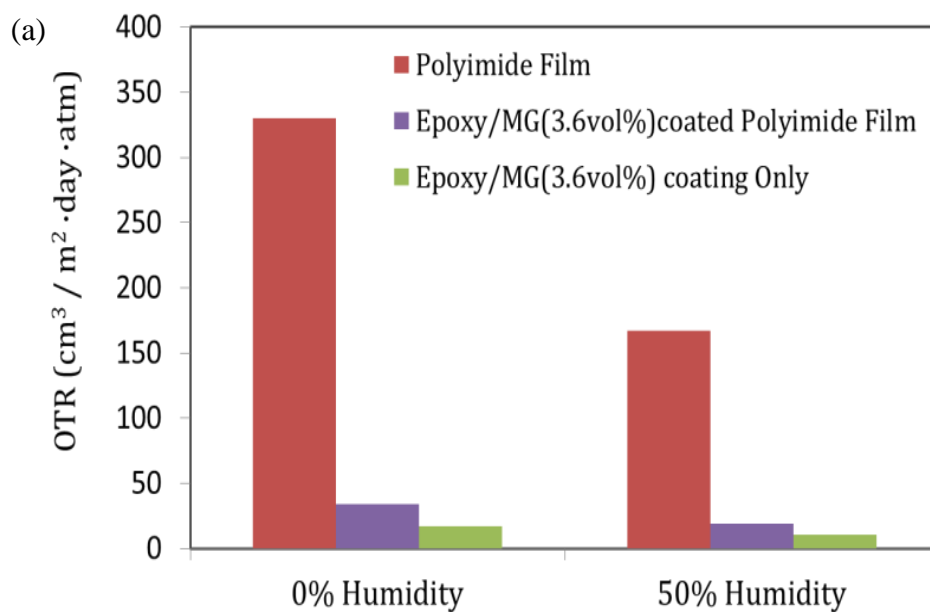


Figure 3.12 (a) Oxygen transmission rate (OTR) and (b) permeability of pure polyimide film, epoxy/MG (3.6 vol.%) coating on polyimide substrate, and epoxy/MG (3.6 vol.%) coating alone at different humidity conditions.

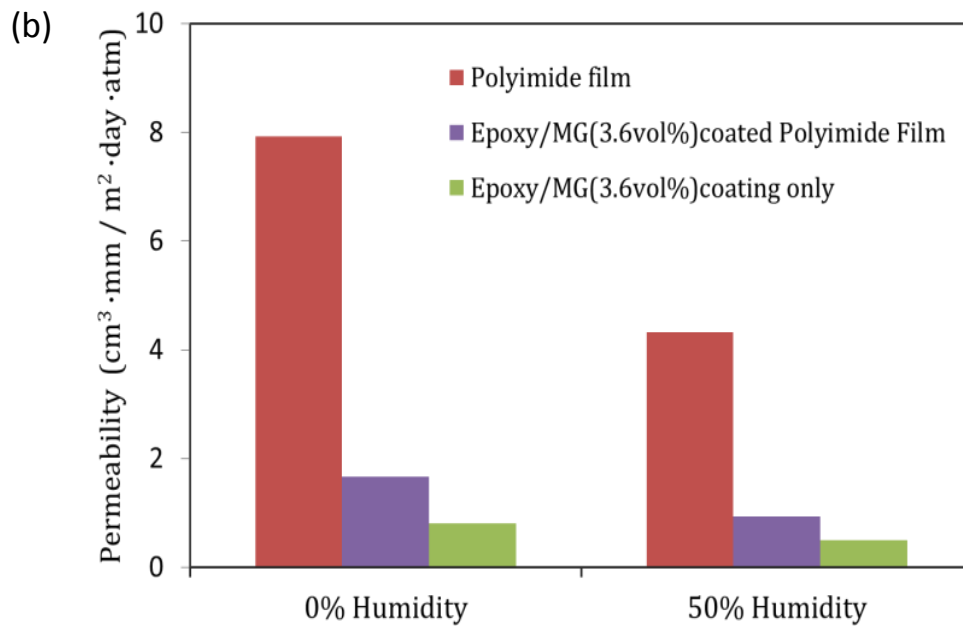


Figure 3.12 Continued.

The oxygen barrier properties at different humidity levels were also evaluated and are shown in Figure 3.12. Both the OTR and oxygen permeability of the epoxy/MG films (3.6 vol.%) show good stability under high humidity conditions (Figure 3.12). Variability in permeability at low and high humidity levels is attributed to water molecules occupying Langmuir sites, which results in a competition in diffusion between water and oxygen molecules, thereby reducing permeation of oxygen. This behavior is in contrast to gas barrier films made by sequential deposition methods, which typically involves hydrophilic polyelectrolytes and show reduced barrier performance in humid environments due to swelling.

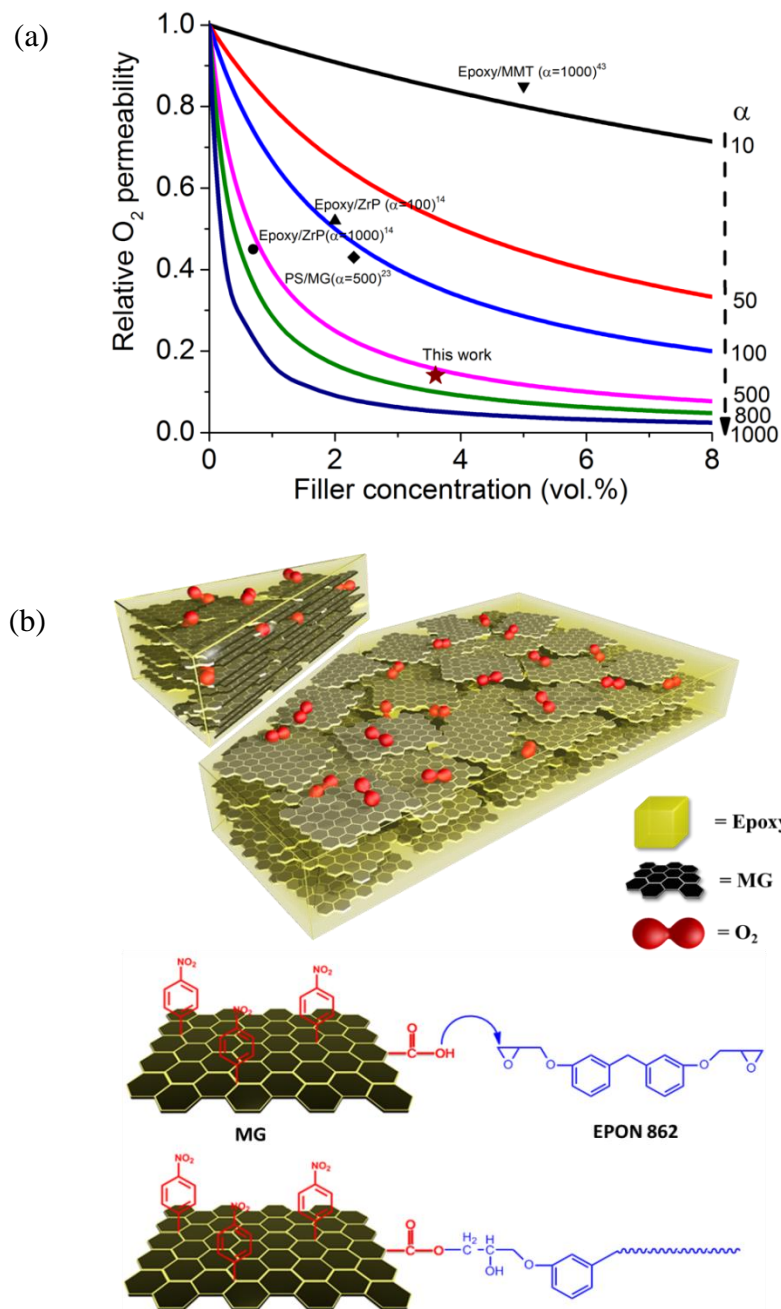


Figure 3.13 (a) Experimental data and Bharadwaj barrier model predictions as a function of nanoplate aspect ratio. (b) Schematic of oxygen barrier mechanism of epoxy/MG nanocomposites.

The barrier performance may be estimated by considering the “tortuosity” of the diffusion pathway for penetrant molecules caused by the impermeable nanoplatelets. The relative permeability can be expressed as[123,124]:

$$(3.1) \quad P_R = \frac{P}{P_0} = \frac{1-\phi}{\tau}$$

where  $P_R$  is relative permeability,  $P$  and  $P_0$  are the permeability coefficients of the polymer nanocomposite and neat polymer, respectively,  $\phi$  is the nanoplatelet volume fraction, and  $\tau$  is the tortuosity factor. The tortuosity factor is conceptually defined as the ratio of actual distance to shortest distance that a penetrant molecule needs to travel to penetrate a surface. In other words, it is the magnitude of perturbation in the pathway followed by a diffusing molecule from the ideal path. The aspect ratio of the nanoplatelets is regarded as one of the most important factors influencing tortuosity. One of the advantages of the MG filler presented here is its high aspect ratio,  $\sim 1500$ , which effectively extends the tortuous pathway of diffusing gas molecules in the composites.

The effect of aspect ratio on the gas permeability is shown in Figure 3.13a. The Bharadwaj model, which developed based on a uniform dispersion state, was used to estimate the “effective” aspect ratio of MG in epoxy. The details about the Bharadwaj model are given in Supplemental Table 1. The effective aspect ratio of MG is estimated to be about 600 (Figure 3.13a). The difference in the expected aspect ratio from that observed experimentally is attributed both to the wrinkled morphology and imperfect alignment of the MG in the polymer matrix. Prior reports have shown that large aspect

ratio nanoplatelets, including ZrP and MMT clay, tend to curl up when imbedded in polymer matrices, which was attributed partially to the residual stress build-up during curing and partially to the presence of defects within the nanosheets structure. The curling of nanoplatelets reduces the effective aspect ratio, thereby reducing the resulting tortuous path experienced by the penetrant molecules. The curling of nanoplatelets obviously complicates the structure–property relationships in polymer nanocomposites.[125]

An additional consideration is the nature of the polymer/nanofiller interface, which is not considered in the available barrier models for rigid 2D fillers. A poor interfacial contact between the nanoplatelets and the matrix will generally diminish barrier properties [126,127]. Owen et al. [108] reported that crumpled graphene sheets can exhibit enhanced interaction with the polymer matrix because the sheets may be more fully “wetted” by the polymer chains. The wrinkled MG sheets in epoxy might favor this interaction more than otherwise. Moreover, the polar functional groups on MG surfaces will likely enhance the compatibility with the epoxy matrix. The chemical reaction mechanism between carboxylic acid-functionalized carbon nanotubes and the epoxide groups of bisphenol-F epoxy resin was reported [128,129]. The formation of covalent bonds leads to a highly cross-linked structure, which efficiently improves load transfer between epoxy and CNTs. As shown in Figure 3.14b, the carboxylic groups on MG surfaces can covalently bond with epoxide groups during epoxy curing. Such a reaction would suppress the formation of interstitial cavities between the MG sheets and the

epoxy matrix, which help maintain oxygen barrier properties in epoxy/MG nanocomposites.

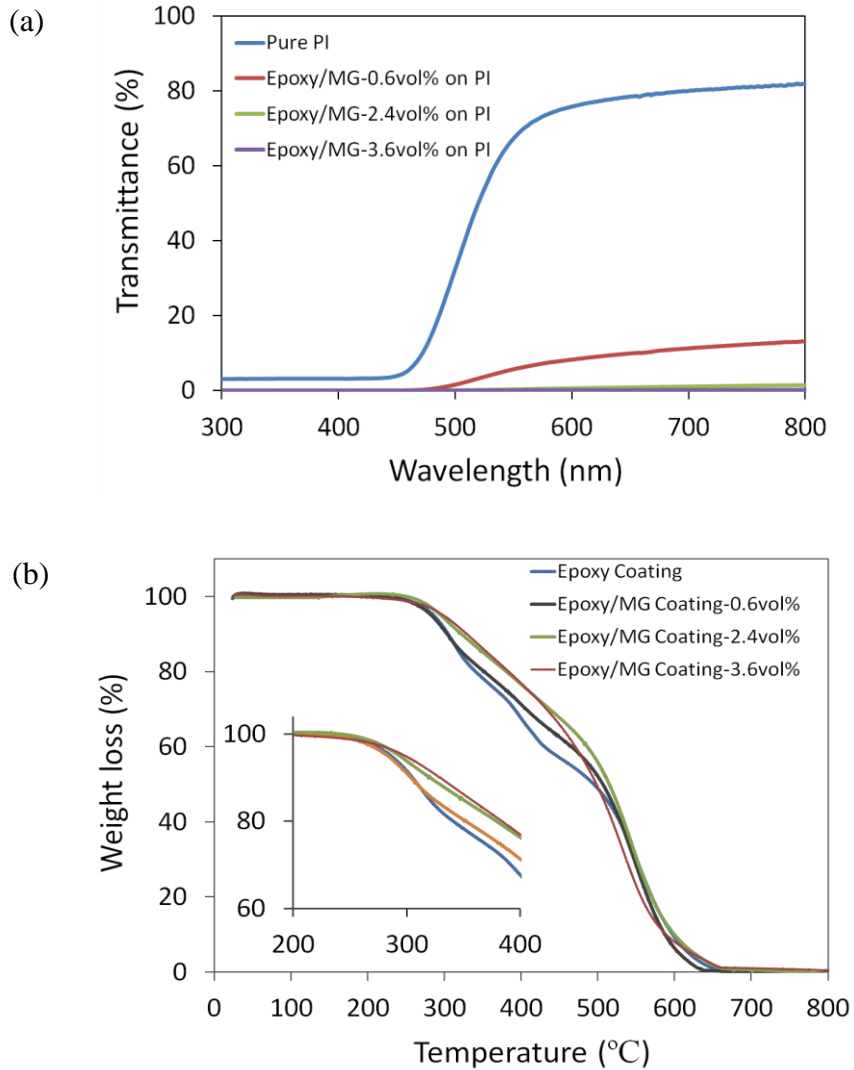


Figure 3.14 (a) Transmittance spectra of epoxy/MG films at various MG concentrations, illustrating a decreased transparency with increased MG loadings. (b) TGA results of epoxy/MG coatings at various MG concentrations.



The shelf life of perishable goods depends on the permeability of gas molecules into products through its outer polymeric packaging materials, along with many other properties. High-energy lighting may degrade light-sensitive food products, vitamins, wines, and electronic devices. The light transmittance of the epoxy/MG films was characterized using UV-vis spectroscopy (Figure 3.15 a), and is significantly reduced compared to that of neat epoxy. The reduction in transmittance is likely due to the good exfoliation of MG within polymer matrix along with its high specific surface area. The MG also improves the thermal stability of epoxy, as shown by the TGA results in Figure 3.15 b. The decomposition temperature of the epoxy/MG nanocomposites is increased compared to the neat epoxy.

Two-dimensional graphene nanosheets and their derivatives have become a versatile building block for fabrication of attractive polymer nanocomposites for structural and functional applications. The gas barrier performance of epoxy/MG nanocomposites is closely related to the MG nanoscale organization and interfacial interaction with the epoxy matrix. In the present work, good-quality epoxy/MG barrier films suitable for large-scale applications were prepared using a simple spray coating method without compromising processability. Entropy-driven nematic phase formation of exfoliated MG nanosheets in epoxy precursor was observed here for the first time. The isotropic-nematic phase transition is originated from a net gain in entropy as the loss of orientational entropy is compensated by the increased translational entropy. Above the critical volume fraction, large aspect ratio MG nanosheets orientate parallel to each other

in order to minimize the excluded volume, thus maximizing the entropy and favoring the nematic order. According to the Onsager' theory, as the aspect ratio increases, the critical volume fraction for mesophase transition decreases. Colloidal self-assembly of nanosheets to form liquid crystalline phase in solvents has been extensively studied. However, fundamental understanding of the same phenomena in polymer matrices is still lacking. Large-scale self-assembly of graphene-based nanosheets in a polymer to form thermodynamically favorable order is challenging. Additional work is currently underway to explore conditions from which liquid crystalline order of MG can be retained and manipulated upon epoxy curing for optimized barrier properties in epoxy/MG nanocomposites.

### **3.4 Conclusion**

Exfoliated epoxy nanocomposites containing large-aspect-ratio MG were prepared via a facile spray coating approach. The MG sheets are individually exfoliated and form liquid crystalline mesophases in epoxy precursor at a low concentration. The spray-coating process allows for the preparation of high MG content nanocomposites without compromising processability. The epoxy/MG nanocomposite films exhibit significantly improved gas barrier properties at different humidity levels. These highly desirable packaging properties make graphene-based epoxy nanocomposites attractive for high performance multifunctional packaging applications.

## CHAPTER IV

### THERMALLY STABLE AND CONDUCTIVE FREE-STANDING HYBRID FILMS BASED ON REDUCED GRAPHENE OXIDE\*

#### 4.1 Introduction

Because Free-standing paper-like materials, such as exfoliated vermiculite platelet film, graphene oxide (GO) film, buckypaper of carbon nanotubes (CNTs), and graphene film, have attracted tremendous research attention for potential applications such as protective layers, sensors/actuators, catalyst supports, and battery components.[107,130-133] Among these, graphene-based materials are especially attractive from both economy and performance perspectives due to their low cost, excellent physical, electrical and mechanical properties.[133-137]

Graphene-based films have been reported to exhibit unique optoelectronic, mechanical and selective barrier properties. Ruoff and his coworkers[135] first prepared GO films with excellent mechanical properties and chemical stability through directed-flow assembly. They have reported that these graphene-based materials could be used as

---

\*Reprinted with permission from “Thermally Stable and Highly Conductive Free-standing Hybrid Films based on Reduced Graphene Oxide” by Peng Li, Haiqing Yao, Minhao Wong, Hiroaki Sugiyama, Xi Zhang, and Hung-Jue Sue. 2014, Journal of Materials Science, 49, 380-391. Copyright (2014) by Springer. <http://link.springer.com/article/10.1007%2Fs10853-013-7715-9>

a light-weight, free-standing and highly conductive ultra-thin foam for applications such as cathodes in lithium ion batteries. These exceptionally light-weight ( $\sim 9.5 \text{ mg/cm}^3$ ) films are unique in that they simultaneously exhibit high specific charge and rate capacity due to their conductive  $\text{sp}^2$  graphenic structure ( $\sim 1.3 \times 10^3 \text{ S/cm}$  at room temperature). Geim and coworkers[133] have developed submicrometer-thick GO membranes, which are completely impermeable to certain gases and liquids, but allowing for unimpeded permeation of water. Kim et al.[138]fabricated transparent conductive films using ultra-large graphene oxide sheets *via* the Langmuir-Blodgett assembly technique. A sheet resistance of about  $500 \text{ } \Omega/\text{sq}$  at 90% transparency was obtained after reduction, which outperforms graphene films directly grown on metal substrate by chemical vapor deposition. These examples feature a common GO synthesis route by oxidizing graphite, which is attractive for industrial large-scale applications. Although the GO film itself is not electrically conductive, most of the conjugated graphene network can be restored by exposing the film to a reduced atmosphere, such as hydrazine vapor exposure or high temperature thermal treatment. However, both of the above reduction methods have their specific drawbacks. The chemical reducing agents can only reduce the outer surfaces of the GO free-standing films. [139]The heat treatment method, which is more efficient and commonly used, often results in the formation of brittle films that can be easily disintegrated into small pieces.[140] Therefore, new methods need to be developed to obtain highly conductive free-standing graphene-based films with good thermal stability.

Assembly of carbon materials (e.g., carbon nanotubes and graphene) and inorganic nanoplatelets presents a new class of hierarchical nanocomposites, which are highly attractive for supercapacitor, electrode, polymer reinforcement, catalysts and chemical sensors applications.[141-143] Zhang et al. [144] reported that graphene/clay hybrid material as a supercapacitor electrode shows better cycling stability, higher rate capability, and superior electrochemical properties at a high current density. It was found that the hybrid of graphene and nickel-layer double hydroxide has good performance for lithium ion battery application: a maximum capacity of 1030 mAh g<sup>-1</sup> during the first discharge, and 400 mAh g<sup>-1</sup> after 10 charge/discharge cycles. There are two common approaches in the preparation of the hybrid systems based on their complex interactions. The first approach involves *in-situ* growth of nanocarbons or nanoclays on the substrate using another type of nanoparticles as the template.[144] The second approach utilizes a strong electrostatic force between negatively charged nanocarbons and positively charged nanoclays, which form a stable dispersion in organic solvents and polymer matrices.[145] In this work, exfoliated nanoclay and GO hybrids were prepared through their electrostatic interactions. De-bundled CNTs, prepared using our previously reported method, were also incorporated to further improve the electrical conductivity of the film.[146] Implication of the present findings for fabrication of strong, sustainable, and electrically conductive films is discussed.

## **4.2 Experimental**

### **4.2.1 Materials**

Graphite material in powder form was donated by Bay Carbon Inc. XD-grade SWCNTs were obtained from Carbon Nanotechnologies, Inc. (Houston, TX). Zirconyl chloride ( $\text{ZrOCl}_2 \cdot 8\text{H}_2\text{O}$ , 98%), potassium permanganate ( $\text{KMnO}_4$ ), barium chloride ( $\text{BaCl}_2$ ), sodium nitrate ( $\text{NaNO}_3$ ) were purchased from Sigma-Aldrich and used as-received.

### **4.2.2 Synthesis and Exfoliation of ZrP Nanoplatelets**

ZrP nanoplatelets were synthesized using a refluxing method. Initially, 15.0 g of zirconyl chloride ( $\text{ZrOCl}_2 \cdot 8\text{H}_2\text{O}$ , 98%) was refluxed in 150.0 mL of 3.0 M  $\text{H}_3\text{PO}_4$  for 24 h. ZrP product was washed three times with de-ionized (DI) water through centrifugation and resuspension, dried at 65 °C in an oven for 24 h, and then gently ground into fine powders with a mortar and pestle. Lastly, the ZrP powder was exfoliated with a commercial monoamine intercalating agent, polyetheramine (Jeffamine<sup>®</sup> M1000), at a molar ratio of ZrP/Jeffamine = 1:0.8 in water.

### **4.2.3 Preparation of De-bundled SWCNTs**

XD-grade SWCNTs were pre-treated in a mixture of concentrated sulfuric and nitric acids (3:1 ratio by volume) in a sonication bath (Branson 2510) for 3 h. DI water was

added to dilute the acid solution and the mixture was sonicated for an additional 3 h. Then, the oxidized SWCNTs were isolated using a polyvinylidene difluoride (PVDF) filter membrane (Millipore, 0.45  $\mu\text{m}$  pore size) under vacuum. After washing with de-ionized water during filtration for several times to remove the acid residue, the SWCNTs were collected and redispersed in water. Next, the solution was mixed directly with fully exfoliated ZrP nanoplatelets (1:5 weight ratio) and sonicated at room temperature for 30 min. During this process, the final SWCNTs are debundled and remain stable in aqueous solution.

#### **4.2.4 Preparation of Graphene Oxide Based Hybrid Films**

Graphene oxide (GO) was synthesized and purified according to the method described in Chapter II. Dispersions of GO, exfoliated ZrP, and de-bundled SWCNTs were directly mixed together at different weight ratios. The weight ratios of GO to ZrP were varied but the ratio between ZrP and SWCNTs was always kept at 5:1 (Table 6.1). The mixture was sonicated (Branson 2510) for 30 min, followed by 6 h of stirring. GO hybrid films were then prepared by filtration of the formed stable colloidal dispersion through a membrane filter (200nm pore size, 47mm in diameter, Whatman). After the filtration, the film was air dried on the filtration membrane. Later, the film samples were peeled off and heated in a tubular furnace from room temperature to 750  $^{\circ}\text{C}$  at a heating rate of 10  $^{\circ}\text{C}/\text{min}$  under argon gas flow. To achieve oxygen reduction reaction, the samples were kept at 750  $^{\circ}\text{C}$  for 2 h.

#### 4.2.5 Characterization

Transmission electron microscopy (TEM) was performed using a JEOL 2010 high-resolution transmission electron microscope, operated at an accelerating voltage of 200 kV. Energy-dispersive spectroscopy (EDS) was conducted in a scanning TEM (FEI Tecnai G2 F20). X-ray diffraction (XRD) patterns were obtained on a Bruker D8 Advanced Power X-ray diffractometer with Cu-K $\alpha$  incident radiation ( $\lambda=1.5418$  Å). Scanning electron microscopy (SEM) images were acquired using a JEOL JSM-7500F Field Emission-SEM (FE-SEM). Optical micrographs (OM) were collected using an Olympus BX60 optical microscope. Electrical conductivity measurements were taken with a custom-built four-point probe apparatus. Raman spectra were acquired on a confocal Raman spectroscope (Horiba Jobin-Yvon LabRam HR system) with 632 nm laser excitation under ambient conditions. XPS analysis was performed with a Kratos Axis Ultra Imaging X-ray photoelectron spectrometer. Tapping-mode atomic force microscopy (AFM) was carried out with a Digital Instruments Nanoscope AFM system. Thermogravimetric analysis (TGA) of film samples was carried out on a Q500-TGA from TA instruments. The annealing process was performed using an atmosphere-controlled furnace (GSL-1700X, MTI Corporation, CA).



## 4.3 Results and Discussion

### 4.3.1 Micromorphology of ZrP/Graphene Composites

Table 4.1. Different samples prepared and their composition.

Sample system	Composition
A	Pure Graphite
B	Pure GO
C	GO(78wt%)/Pristine ZrP(22wt%)
D	GO(88wt%)/Exfoliated ZrP(12wt%)
E	GO(80wt%)/Exfoliated ZrP(20wt%)
F	GO(57wt%)/Exfoliated ZrP(43wt%)
G	GO(76wt%)/Exfoliated ZrP(20wt%)/SWCNTs(4wt%)
H	TRGO
I	TRGO(80wt%)/Exfoliated ZrP(20wt%)
J	TRGO(76wt%)/Exfoliated ZrP(20wt%)/SWCNTs(4wt%)

The incorporation of the exfoliated ZrP nanoplatelets in the GO matrix plays a critical role in the current approach. The thickness of the dispersed GO sheets, synthesized using the modified Hummers' method, was characterized by AFM as shown in Figure 4.1 (a). The measured ~0.9 nm thickness suggested that GO were individually dispersed in water, which was likely due to the long-range electrostatic repulsion between the ionized oxygen-containing functional groups on GO surfaces. The full

exfoliation of the ZrP nanoplatelets in water leads to a transparent suspension even at a high concentration of 10 g/L. The synthetic ZrP platelet has a diameter of about 120 nm and a regular hexagonal shape (Figure 4.1 (c) and (d)). When the exfoliated ZrP and GO solutions are physically mixed, the aqueous suspension (System E) is stable and does not exhibit agglomeration after 48 h storage (Figure 4.1(b)). TEM image of GO/ZrP dispersion (System E) is shown in Figure 4.1 (e). The dark area indicates that the GO sheets are either folded or wrinkled, which is likely caused by the drying process during the TEM sample preparation. The tethering between the ZrP nanoplatelets and GO is highlighted by the arrows, suggesting that there exists a strong electrostatic interaction between them. The corresponding EDS spectrum of TEM image is shown in Figure 4.1(f). All C and Zr elements are spread in the same general area, which means that ZrP nanoplatelets are likely to be intermixed.

It has been reported that<sup>[147-149]</sup> highly ordered 2-D colloids show birefringent liquid crystalline behavior. To determine whether or not the GO/ZrP suspension can self-assemble into birefringent phase, the suspension with a weight ratio of GO and ZrP = 4:1 (System E) was centrifuged at 20,000 RPM (43206 RCF). Then the sediment was collected and redispersed into a high concentration of 7 wt.%. As is shown in Figure 6.2, droplets of the GO/ZrP suspension (System E) were observed under cross-polarized light and the images were recorded as a function of water evaporation time. As expected, the GO/ZrP suspension shows a strong birefringence when dried at room temperature after 2 min and 30 min (Figure 4.2(a, b)), respectively. For reference, the GO/pristine ZrP

suspension (System C) does not exhibit the same characteristics. A possible corresponding mechanism is illustrated in Figure 4.2 (c). Compared to System C, there is a stronger interaction between GO and exfoliated ZrP (System E) due to their mutual

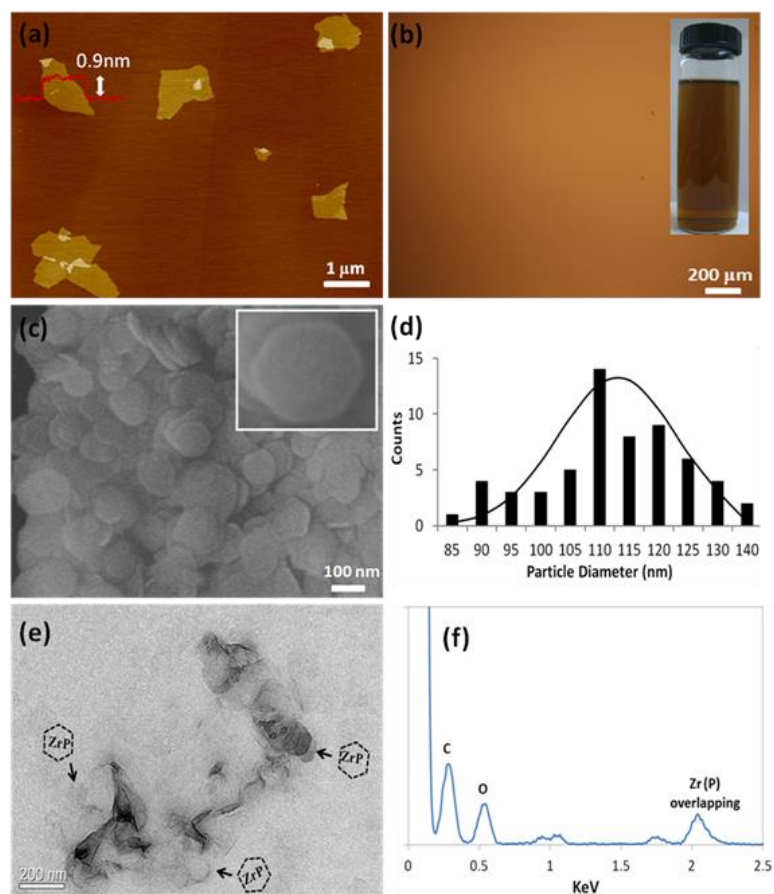


Figure 4.1 (a) Atomic force microscopy (AFM) image of GO deposited on mica surface from aqueous solution (inset: height profile of GO). (b) OM of GO/ZrP (System E) at 10 g/L on a glass slide (inset: photograph of the aqueous suspension). (c) SEM of ZrP (inset: an individual ZrP), (d) size distribution of ZrP particles. (e) TEM of GO/ZrP (System E) dispersion, and (f) its corresponding EDS spectrum.

hydrogen bonding formation. During exfoliation of pristine ZrP, the monoamine intercalation agent migrates into the gallery of ZrP through proton exchange process, leading to the full exfoliation of ZrP in water. The presence of exfoliated nanoplatelets maximizes the exposure of ZrP to GO, thereby enhancing hydrogen bonding between ZrP and the functional groups (e.g., carboxyl, hydroxyl, epoxy groups) on the GO surfaces. This leads to the formation of a highly ordered liquid crystalline structure.

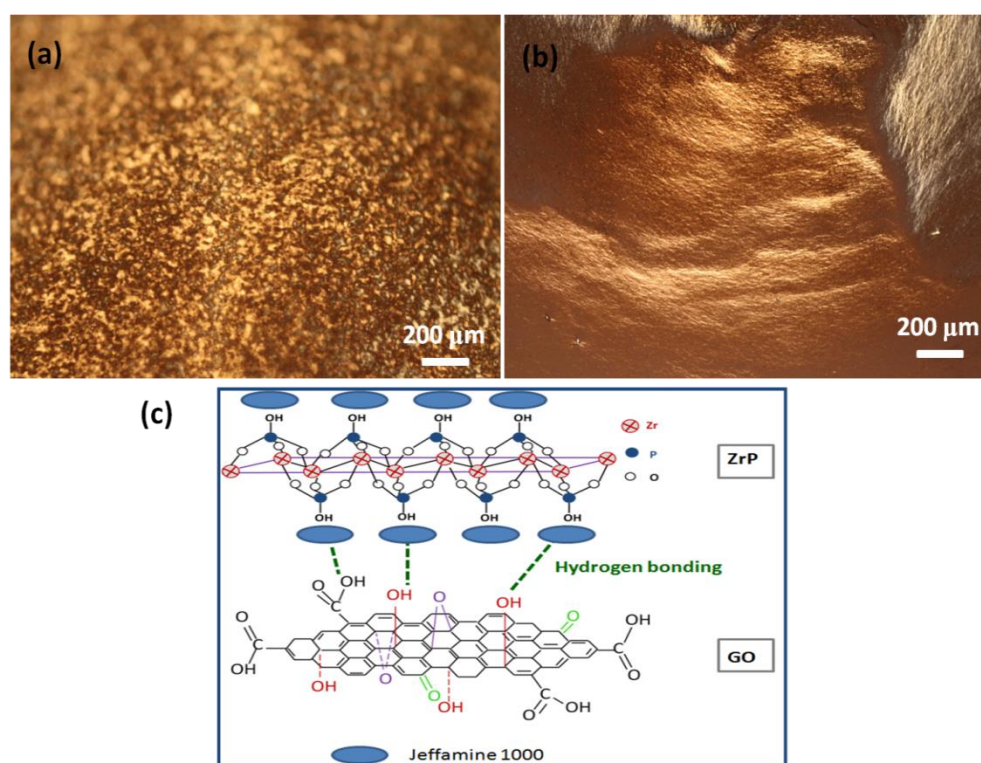


Figure 4.2 Polarized-light optical microscopy images of GO/ZrP (System E) after (a) 2 min and (b) 30 min of solvent evaporation. (c) Schematic of possible interaction between GO and ZrP.

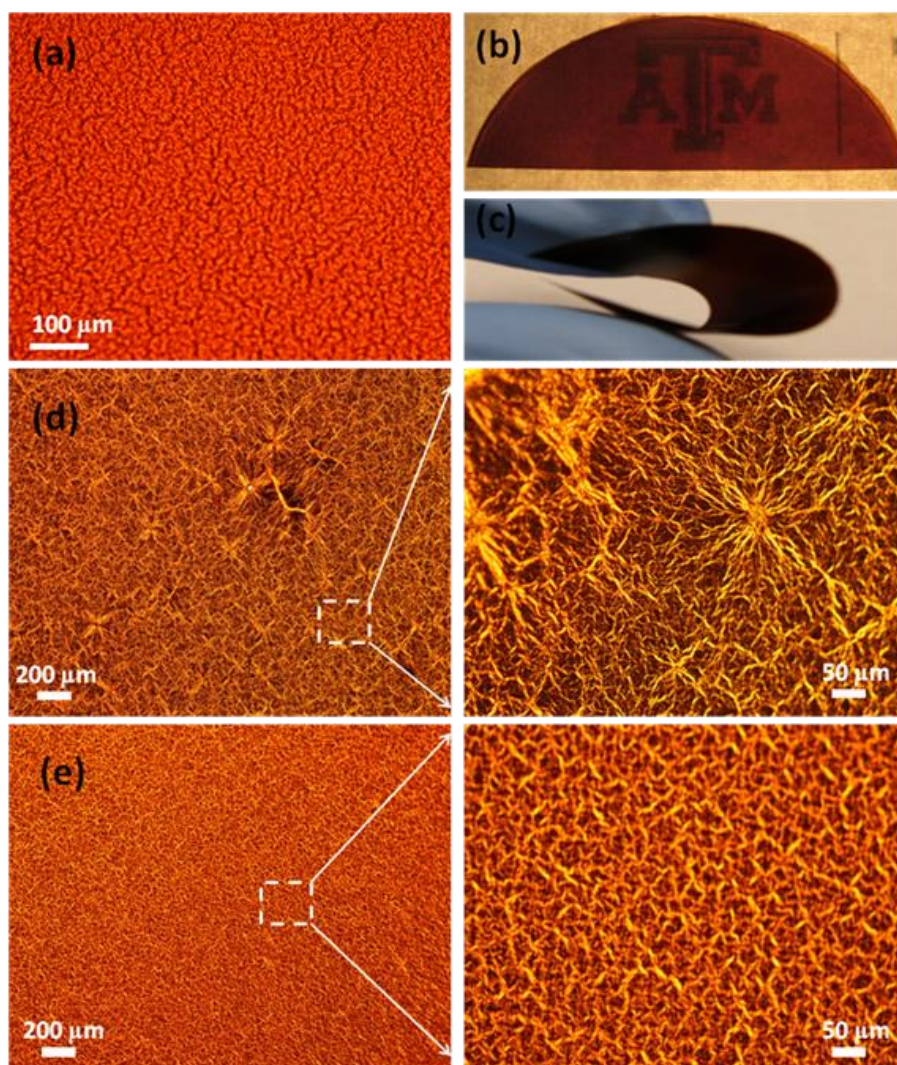


Figure 4.3 (a) – (c) OM images of GO/ZrP film (System E) at various magnifications. Polarized-light OM images of (d) GO film (System B) and (e) GO/ZrP hybrid film (System E).

GO hybrid films were prepared by direct filtration of the colloidal dispersions. These films were air dried and then peeled off from the filter membrane. It is well known that GO could easily form thin films with a smooth surface due to their large aspect ratio.

However, when pristine ZrP is incorporated, the obtained film (Supplemental Figure S2) appears to be rough and contains large particles aggregates (System C). In contrast, the GO/ZrP film prepared from exfoliated ZrP (System E) has a smooth surface (Figure 4.3(b)). Furthermore, the GO/ZrP hybrid film is flexible and could be bent easily without causing crack formation, which implies a good mechanical integrity due to the affinity between the exfoliated ZrP and GO particles (Figure 4.3(c)). With a thickness of 7  $\mu\text{m}$ , the transparency of the GO/ZrP film is still maintained ((Figure 4.3(b). OM image (Figure 4.3 (a)) of the GO/ZrP film surface clearly shows its smooth surface. Under cross-polarized light, the GO/ZrP hybrid film (Figure 4.3(d)) exhibits a more uniform structure when compared to pure GO film (Figure 4.3(e)). It appears that the synergistic interaction between GO and exfoliated ZrP improves the structural integrity of the thin film.

Figure 4.4 presents SEM images which further reveal the surface morphological differences between the films. GO sheets, if freely suspended in solution, are likely to be corrugated. This may result in wrinkling of the GO thin films after drying from SEM, as shown in Figure 4.4(a). GO/pristine ZrP film surface (Figure 4.4(b)) has a rough surface and contains big particle aggregates. However, when exfoliated ZrP were introduced into GO matrix, the GO/ZrP (System E) film exhibits a more smooth morphology (Figure 4.4(c)). From the cross-sectional view, different characteristics of layer structures can be clearly differentiated in the films (Figure 4.5). Delamination between layers is found in the pure GO film (Figure 4.5(a)). Upon introduction of pristine ZrP into the GO matrix



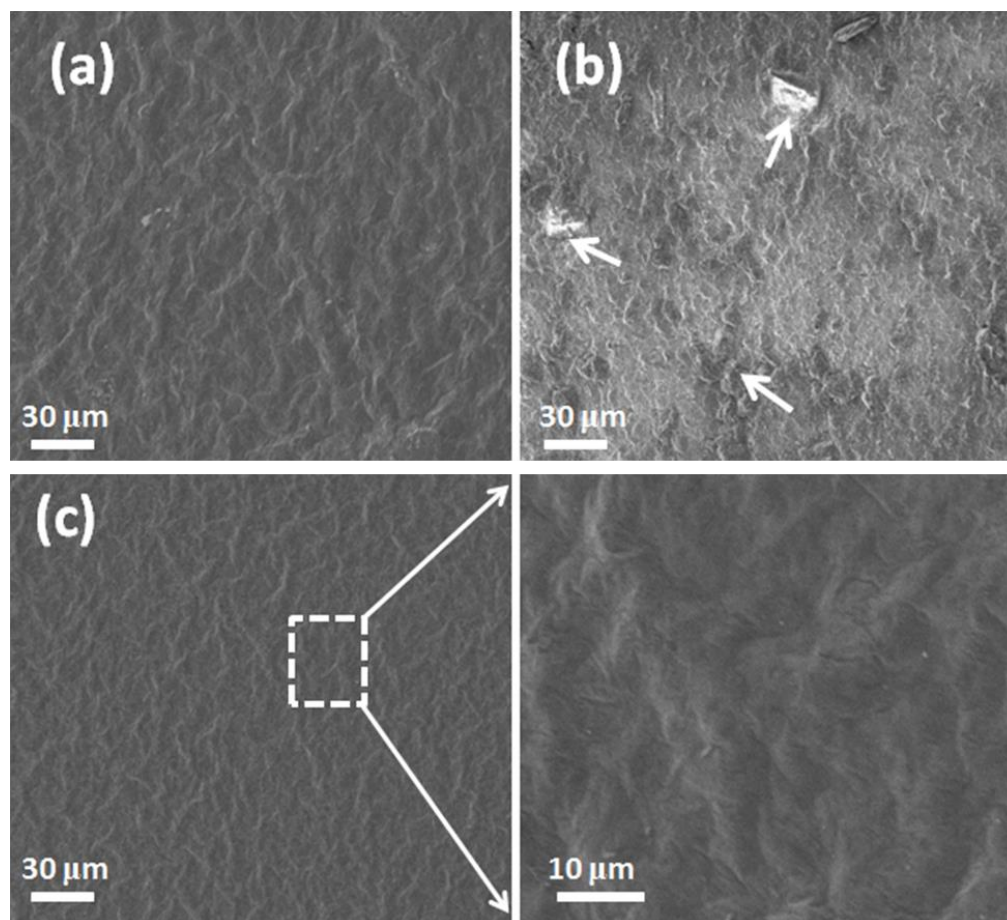


Figure 4.4 SEM images of different free-standing films from surface view of (a) pure GO (System B), (b) GO/pristine ZrP (System C), and (c) GO/ZrP (System E). White arrows indicate big aggregated particles.

(System C), the layer structure appears to be loose and disintegrated (Figure 4.5(b)). However, when exfoliated ZrP is introduced into the GO film matrix (Systems E), the layer structure becomes well integrated and shows no delamination (Figure 4.5(c)). This further implies that there exists a synergistic interaction between the GO and ZrP sheets,

which helps to form a well-integrated layer structure. The EDS elemental mapping of C and Zr of GO/ZrP hybrid film (System E) are shown in Figure 4.5(d) and (e), respectively, indicating that ZrP nanoplatelets are well dispersed within GO matrix.

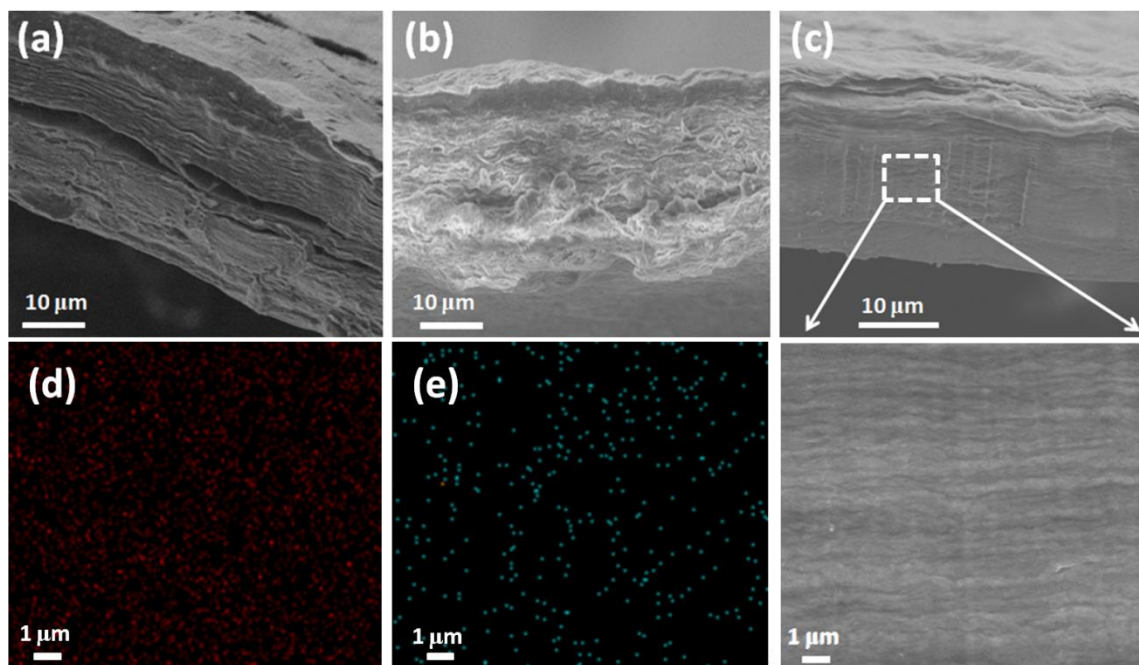


Figure 4.5 SEM images of different free-standing films from cross-sectional view: (a) pure GO, (b) GO/pristine ZrP (System C), and (c) GO/ZrP (System E). EDS mapping of GO/ZrP film (System E) from cross-sectional view showing distribution of different elements: (d) C and (e) Zr.



### 4.3.2 Thermal Stability and Conductivity of Graphene Hybrid Films

TGA was used to evaluate the thermal stability of GO films and the GO/ZrP hybrid films in air. As shown in Figure 4.6, graphite material exhibits excellent thermal stability up to 790 °C, followed by a gradual degradation. The analysis of GO film indicates a typical 3-stage weight loss pattern in air, which is in agreement with literature finding.[150] Below 150 °C, a mass loss of ~13% is observed and can be attributed to desorption of physically absorbed water. A mass loss of ~25% is found at around 200 °C and is ascribed to the decomposition of oxygen-containing functional groups present on the surface of GO. Between 500 °C and 700 °C, a mass loss of ~40% occurs owing to the basal plane decomposition of the sp<sup>2</sup> graphitic lattice. Interestingly, the introduction of exfoliated ZrP into the GO matrix has considerably improved the thermal stability of GO. Table 4.2 lists the concentration dependency of the GO basal plane decomposition temperature with the presence of exfoliated ZrP. The decomposition temperature directly correlates well with the weight percent of exfoliated ZrP incorporated. On the contrary, the introduction of pristine ZrP into the GO hybrid films reduces the decomposition temperature. Therefore, the level of exfoliation of ZrP has a significant effect on the thermal stability of GO hybrid films, possibly due to the lack of diffusion pathway for oxygen to migrate through GO-ZrP hybrid layers.

Upon thermal treatment at 750°C in argon atmosphere, GO hybrid films were effectively reduced to remove a great portion of oxygen-containing functional groups.

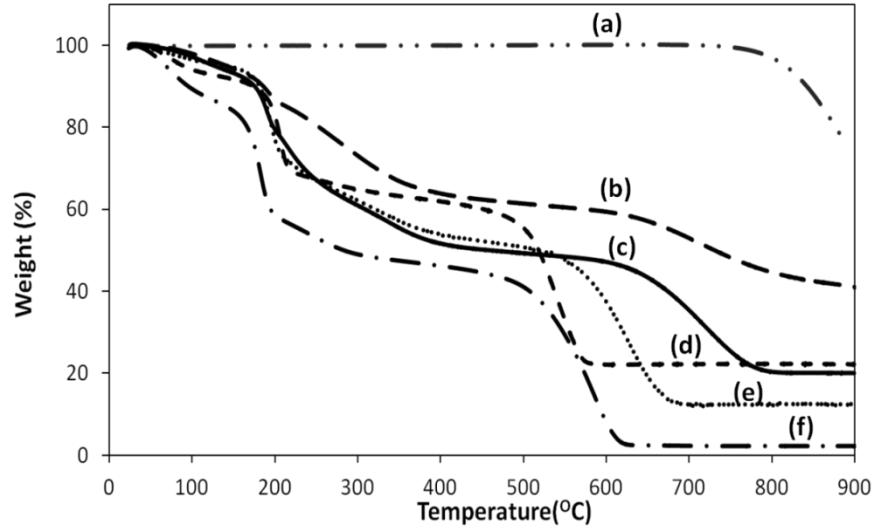


Figure 4.6 TGA study of GO/ZrP films with different ZrP loading. (a) Graphite, (b) GO/ZrP-43% (System F), (c) GO/ZrP-20% (System E), (d) GO/pristine ZrP-22% (System C), (e) GO/ZrP-12% (System D), and (f) GO.

Table 4.2 GO decomposition temperatures of films with different ZrP loading.

Film	System B	System C	System D	System D	System F
T (°C)	532	521	608	646	655

The evolution of the surface functionality of the free-standing films after thermal treatment was determined by XPS. The C 1s fine scan spectra (Figure 4.7) are composed of C-C (~284 eV) and C-O (~287 eV, hydroxyl and epoxy), similar to literature findings.[151] The relative contents of C and O for various films are listed in Table 4.3.

After annealing at 750°C, the total content of oxygen functional groups was observed to decrease dramatically. The increase in the C/O atom ratio after annealing confirms the removal of oxygen functional groups during the thermal treatment (i.e., Systems B vs. System H and Systems E vs. System I shown in Table 4.3). It is noticed that the TRGO/ZrP hybrid film has a lower C/O ratio of 4.1 compared to 5.2 of the TRGO film. This is because ZrP nanoplatelets contain a great amount of oxygen, which impedes the direct C/O ratio comparison between the two types of the films.

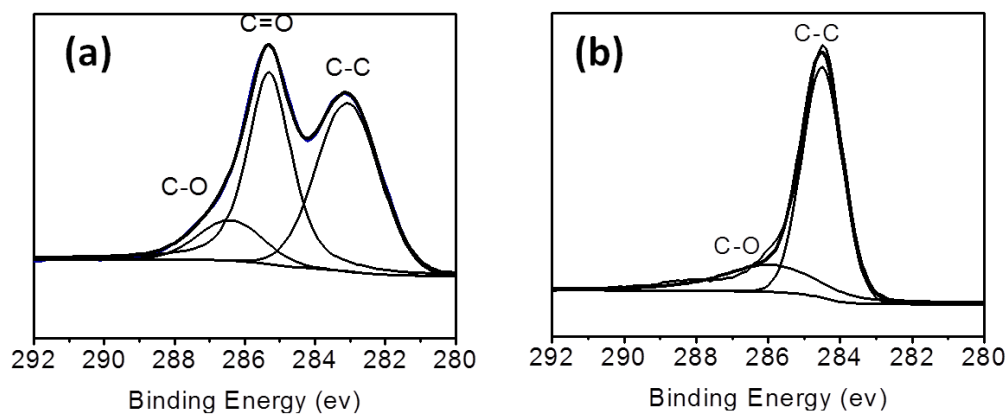


Figure 4.7 XPS elemental analysis: C1s spectra of (a) GO and (b) TRGO.

XRD spectra of prepared free-standing films are illustrated in Figure 4.8. The XRD pattern of GO film exhibits a diffraction peak at  $2\theta=10.7^\circ$ , which corresponds to an interlayer spacing of 0.84 nm, which is much larger to that of pristine graphite (0.34 nm). A possible reason for the discrepancy is the presence of functional groups attached on

Table 4.3 XPS analysis of C, O contents and calculated C/O ratios for different films.

Film	C (atom%)	O(atom%)	C/O
System B	71.72	26.83	2.7
System H	82.87	16.09	5.2
System E	61.45	28.72	2.1
System I	70.37	17.31	4.1

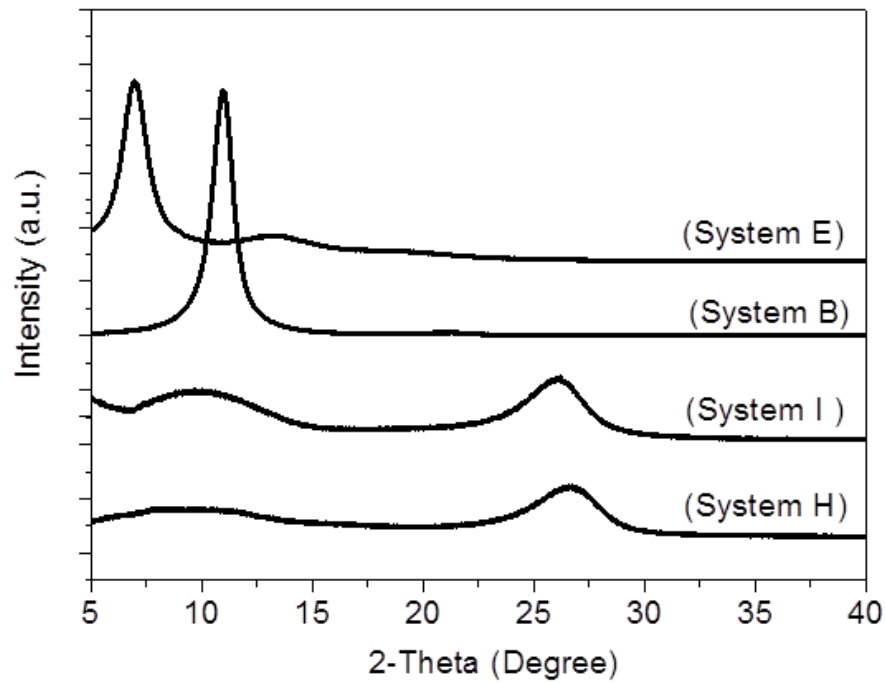


Figure 4.8 XRD patterns of different free-standing film samples before and after thermal annealing process.

GO surfaces. The XRD diffraction peak of GO/ZrP hybrid film (System E) shifts to  $2\theta=6.8^\circ$ , corresponding to an interlayer spacing of 1.29 nm, indicating a further insertion of ZrP to the larger GO layers. After thermal treatment, the interlayer distance of the TRGO film (Systems H) decreases to 0.34 nm ( $2\theta =26.7^\circ$ ), suggesting that a significant amount of the oxygen species on GO were removed after thermal annealing. In the XRD pattern of TRGO/ZrP hybrid film (System I), a similar peak at  $2\theta =25.8^\circ$  was observed, accompanied by an additional peak at  $2\theta = 9.6^\circ$  which corresponds to an interlayer d-spacing of 0.92 nm. This peak is probably due to the presence of thermally reduced graphene layers intercalated by inorganic pyrophosphate. The above XRD results suggest that thermal treatment is effective in reducing GO and GO hybrid films.

SWCNTs and graphene are one-dimensional and two-dimensional carbon materials, respectively. With certain property similarities, the two forms of carbon materials differ in many other aspects due to their different structural characteristics. Many attempts have been made to integrate these two materials and achieve synergized benefits. Here, exfoliated SWCNTs were prepared using the previously established nanoplatelet-dispersion method. GO/ZrP/SWCNT and TRGO/ZrP/SWCNT hybrid films were prepared using the same method described above. OM of GO/ZrP/SWCNT hybrid film (System G) shows again that the film is smooth with great mechanical flexibility (Figure 4.9(a)). SEM characterization from both surface and cross-sectional view confirm the surface smoothness and well-integrated layer structure (Figure 4.9(b) and (c)).

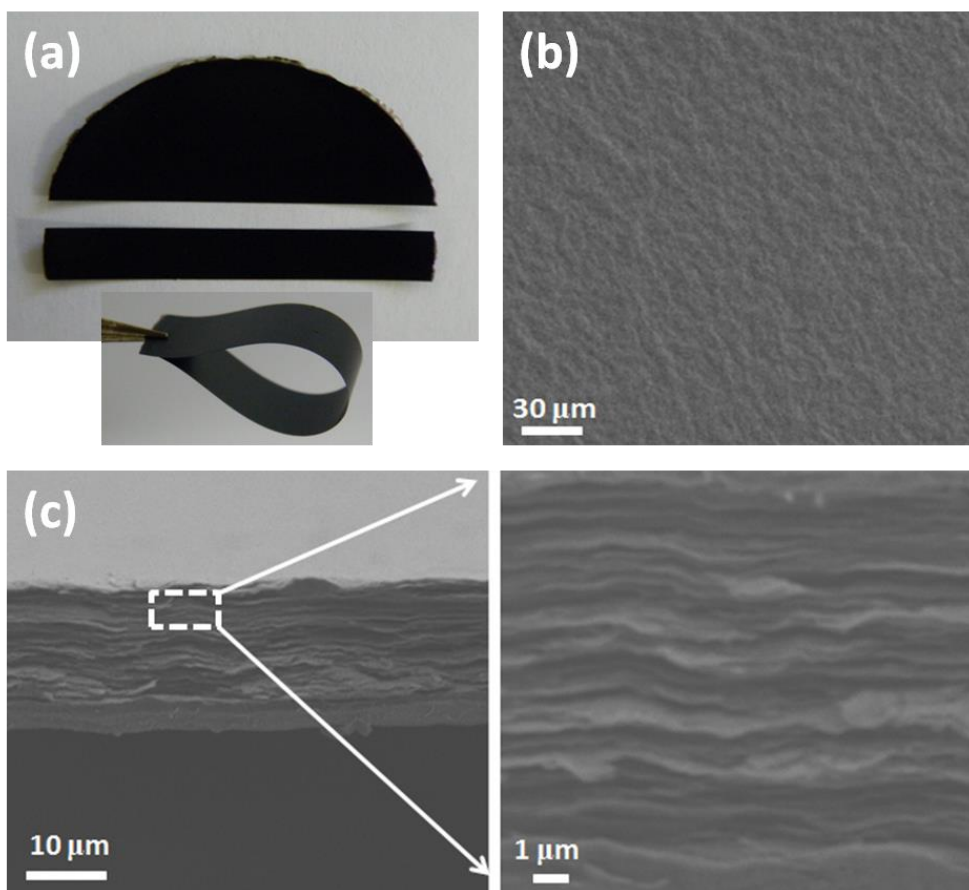


Figure 4.9 (a) Visual images, (b) SEM surface view, and (c) SEM cross-sectional view of GO/ZrP/SWCNTs (System G) film.

Thermal annealing is an easy and effective approach to reduce GO free-standing films. However, the high temperature annealing would alter the structural integrity of the free-standing films. To examine the structural integrity, the morphology of the free-standing films after annealing is characterized. Figure 4.10(a) shows that pure TRGO film (System H) forms a lot of cracks and is easy to disintegrate. The absence of cracks on the surface of the TRGO hybrid films, i.e., Systems I and J, qualitatively indicates

improved structural integrity. This improvement could be partially due to the increased thermal stability of GO as a result of the introduction of exfoliated ZrP into the GO matrix.

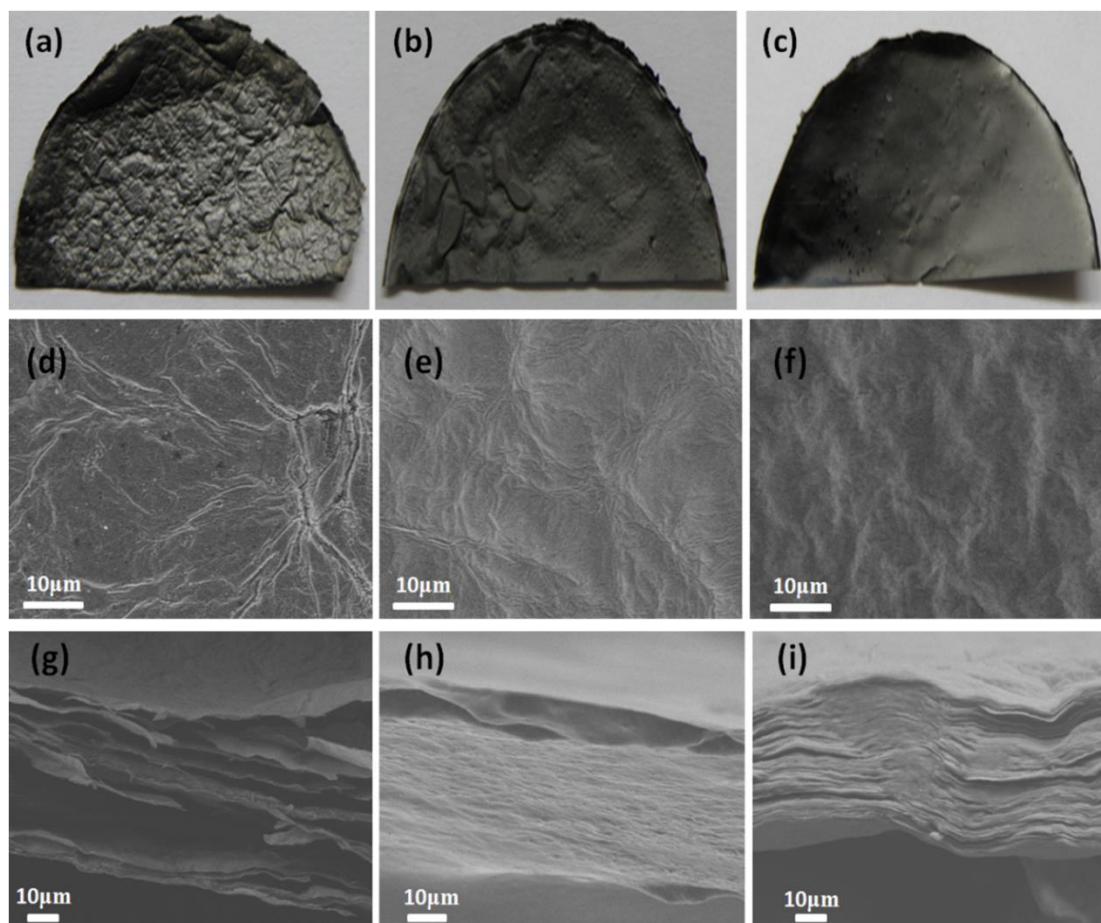


Figure 4.10 Photographs of various free-standing films (35 mm in diameter): (a) TRGO (System H), (b) TRGO/ZrP (System I), and (c) TRGO/ZrP/SWCNTs (System J). SEM surface and cross sectional views of: (d, g) TRGO, (e,h) TRGO/ZrP, and (f, i) TRGO/ZrP/SWCNTs.

The proposed role for ZrP during the GO thermal reduction process is schematically illustrated in Figure 4.11. During the annealing process, the oxygen-containing functional groups (e.g., hydroxyl, epoxy groups) on the GO surface will be removed as CO or CO under argon atmosphere. Moreover, further removal of carbon atoms from the GO plane is more likely to happen when the initial epoxy and hydroxyl groups on the GO surface are in close proximity to each other. The loss of carbon atoms and oxygen species would cause a shrink in the size of sp<sup>2</sup> domains, leading to internal stress buildup on the TRGO basal plane. Therefore, cracking or delamination on neat TRGO films will take place during annealing (Figure 4.11a). However, upon introduction of ZrP nanoplatelets into the GO matrix, the individually exfoliated ZrP would be tethered on GO surfaces due to their mutual strong electrostatic interaction. Consequently, the possible crack formation of GO sheets in the hybrid film was inhibited by the presence of ZrP nanoplatelets to preserve structural integrity during annealing (Figure 4.11b).

To verify the recovery of the sp<sup>2</sup> structure in TRGO films, the electrical conductivity of the various film systems was measured. Before high temperature thermal annealing, pure GO film and GO/ZrP hybrid film exhibit low electrical conductivity. After thermal treatment, sp<sup>3</sup> structures transform into a more perfect sp<sup>2</sup> structure upon removal of oxygen functional groups. As illustrated in Table 4.4, all three films exhibit high electrical conductivity after annealing. It should be noted that the TRGO/ZrP film (System I) displays a lower conductivity than the pure TRGO because ZrP is not electrically conductive and might have disrupted a portion of conductive pathways. To



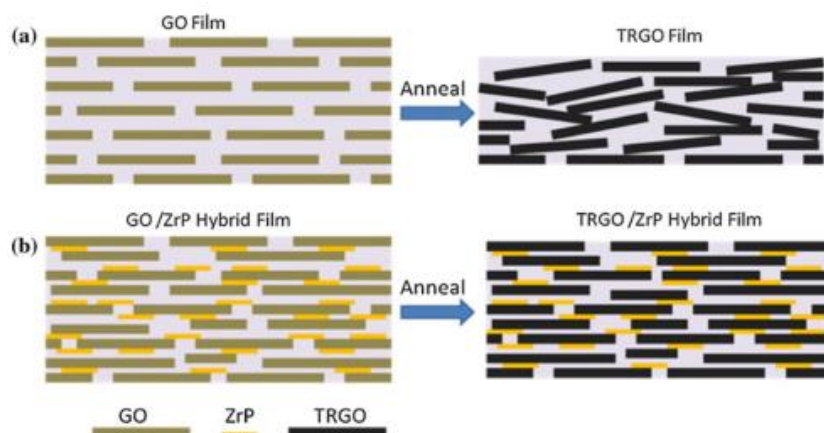


Figure 4.11 Illustration of thermal reduction process of (a) GO film and (b) GO/ZrP hybrid film during annealing.

Table 4.4 Electrical conductivity of different free-standing films.

Film	Electrical conductivity (S/m)
System B	$1.3 \times 10^{-2}$
System H	10760
System I	5510
System J	6420

improve structural integrity and electrical conductivity, exfoliated SWCNTs were introduced into the GO/ZrP film. As expected, the hybrid TRGO/ZrP/SWCNTs film (System J) exhibits an improved electrical conductivity over the TRGO/ZrP film, probably because of the increased conductive pathways by SWCNTs.

Graphene based hybrid films containing inorganic nanoplatelets were successfully prepared to simultaneously exhibit good structural integrity, great thermal stability, and high electrical conductivity. These hybrid films have potential for applications including protective layers, supercapacitors, electronic components, etc. The introduction of SWCNT into TRGO/ZrP structure further improves structural integrity and electrical conductivity of the films. It is highly possible that an optimized formulation can be achieved to prepare hybrid films with maximum electrical conductivity and structural integrity for various device applications. These possibilities will soon be explored.

#### **4.4 Conclusion**

Thermally stable and highly conductive graphene-based hybrid films containing exfoliated ZrP nanoplatelets were prepared. GO/ZrP hybrid films exhibit a better mechanical integrity and thermal stability than the pure GO film due to synergistic interaction between the GO and ZrP nanoplatelets. In contrast, the introduction of pristine ZrP alone decreases the decomposition temperature of GO hybrid film, indicating the importance of ZrP exfoliation for thermal degradation stability of GO. Oxygen-containing functional groups from GO surfaces were effectively removed during high temperature thermal annealing under an argon atmosphere, resulting in dramatic recovery of the graphene sp<sup>2</sup> network structure. This study demonstrates an easy and effective method to fabricate highly conductive free-standing films with good thermal stability, which can be used in various engineering and device applications.

**CHAPTER V**  
**HIGH-PERFORMANCE EPOXY NANOCOMPOSITE COATINGS**  
**CONTAINING SELF-ASSEMBLED CLAY IN SMECTIC ORDER\***

**5.1 Introduction**

Polymer/clay nanocomposites have received tremendous attention in recent years due to their low cost, excellent performance at much lower concentrations than needed with conventional, micron-diameter fillers and potential for expanding the application space of polymers.[25-27] However, there remain significant challenges to achieving high-volume production of high-performance polymer/clay nanocomposites for commercial applications, particularly due to current limitations in the incorporation of high levels of clay in polymer matrices without causing clay agglomeration or requiring sophisticated, and energy intensive, sample preparation steps. Biological materials such as nacre have outstanding properties due to their robust brick-and-mortar architecture, which consists of alternating layers of soft proteins and aligned calcium carbonate platelets.[28] The performance of polymer/clay nanocomposites may potentially be significantly improved by achieving similar nacre-inspired architecture.

---

\*Reprinted with permission from “Highly Effective Anti-corrosion Epoxy Spray Coatings Containing Self-assembled Clay in Smectic Order” by Peng Li, Xingliang He, Tsao-Cheng Huang, Kevin. White, Xi Zhang, Hong Liang, and Hung-Jue Sue. 2015, *J. Mater. Chem. A*, 3, 2669-2676 Copyright (2015) by Royal Society of Chemistry. <http://pubs.rsc.org/en/content/articlelanding/2015/ta/c4ta06221c#!divAbstract>

Transferring these highly regular and organized structures into a structural polymeric system will yield commercially viable materials suitable for a variety of high performance engineering applications, such as light-weight vehicles, high-performance packaging materials, aerospace structures, and biomedical implants, but must be achieved in an efficient and scalable manner.

Crystalline plate-like nanostructures, such as graphene and clays, are excellent barrier materials to gases and moisture[152,153] and have been integrated with polymeric binding resins and applied as nanocomposite coatings to improve the corrosion resistance of metals.[36,37,154] The barrier properties of these protective coatings strongly depend on the aspect ratio, volume fraction, dispersion level, and, in particular, degree of alignment of the fillers. Inspired by highly aligned platelet-based lamellar structures observed in natural materials such as nacre, several assembly techniques have been developed to fabricate polymer/clay nanocomposites with lamellar structure, such as layer-by-layer (LbL) assembly, ice templating and sintering of ceramics, vacuum-assisted self-assembly, electrophoretic deposition, and air/water interface assembly.[40,42,155,156] However, the above approaches typically share the limitations of requiring time-consuming sequential depositions or extensive energy consumption, and suffer from limited robustness and poor stability in humid or aqueous environments, which severely limit large-scale applications.

Here we reported a facile and scalable spray-coating approach to prepare epoxy coatings that contain self-assembled  $\alpha$ -zirconium phosphate (ZrP) nanoplatelets in

smectic order. These ZrP-containing epoxy coatings exhibit long-range order with platelets organized in discrete layers aligned parallel to the substrate. In the present work, we demonstrate that the spray-coating approach can be used to deposit an ordered mesophase of ZrP nanoplatelets on a metal substrate. Electrochemical analyses reveal an order of magnitude improvement in corrosion resistance when compared with an Al substrate coated with the unfilled epoxy alone. Cross-polarized light optical microscopy and small-angle X-ray scattering (SAXS) show that the exfoliated ZrP could form a highly oriented smectic phase in various solvents, which further broadens the practical application of the present approach.

## **5.2 Experimental**

### **5.2.1 Materials**

Zirconyl chloride (98%, Aldrich) and phosphoric acid (85%, EM Science) were used as received. A commercial polyoxyalkyleneamine, Jeffamine® M1000, M600 and M2000 were obtained from Huntsman Chemical Corporation. Bisphenol F epoxy resin and Epikure W curing agent were purchased from Momentive. Aluminium alloy (6061) was purchased from McMaster-Carr.

### **5.2.2 Synthesis and Functionalization of ZrP Nanoplatelets**

ZrP nanoplatelets were synthesized using a previously reported refluxing method.<sup>35</sup> Zirconyl chloride (15 g) was refluxed in 3.0 M H<sub>3</sub>PO<sub>4</sub> (150 mL) for 24

h. The ZrP product was washed three times with de-ionized (DI) water through centrifugation and resuspension, dried at 65 °C in an oven for 24 h, and subsequently ground into a fine powder with a mortar and pestle. The recovered ZrP powder was exfoliated with a commercial monoamine intercalating agent (Jeffamine® M1000) in acetone.

### **5.2.3 Preparation of Epoxy/ZrP Coatings in Smectic Order**

5 g of bisphenol F epoxy was dissolved in 10 mL of acetone to form a clear solution. The epoxy solution was added dropwise to a dispersion of ZrP in acetone (20 mg/mL), and was mechanically stirred for 6 h to achieve a homogenous dispersion. The solvent was removed using a rotary evaporator. Then, 1.33 g of Epikure W curing agent was added and homogenized by mechanical mixing. The epoxy/ZrP liquid mixture was applied to a metal substrate by a spray-coating method. The coatings were cured under nitrogen atmosphere at 50 °C for 1 hr, 90 °C for 2 h, 120 °C for 1 h, and 190 °C for 6 h.

### **5.2.4 Characterization**

Transmission electron microscopy (TEM) was performed using a JEOL 2010 high-resolution transmission electron microscope operating at an accelerating voltage of 200 kV. Energy-dispersive spectroscopy (EDS) was conducted on a scanning FE-SEM (JEOL JSM-7500F). Optical micrographs (OM) were collected

using an Olympus BX60 optical microscope. Small-angle X-ray scattering (SAXS) and grazing-incidence experiments were performed on a Rigaku S-Max 3000 unit at the University of Houston. Data were collected at a grazing incidence angle of  $0.05^\circ$  (Cu  $K_\alpha$  radiation,  $\lambda = 1.54056 \text{ \AA}$ ). Before coating and corrosion testing, the Al surfaces were electrochemically polished in a solution of 10 vol.%  $\text{HClO}_4$  and 90 vol.% ethanol at  $0^\circ\text{C}$  using graphite as the counter electrode under an applied voltage of 23 V for 3 min. A three-electrode electrochemical cell was employed for potentiodynamic and electrochemical impedance spectroscopy (EIS) measurements. A platinum filament and a standard saturated calomel electrode (SCE,  $\text{Hg}/\text{Hg}_2\text{Cl}_2$ ) served as counter electrode and reference electrode, respectively. The exposed testing surface area (diameter of 5 mm) was kept constant for all tests. During the EIS experiments, a sinusoidal signal (5 mV of amplitude and 100 kHz to 0.1 Hz of frequencies) was applied to the working electrode. The step width was selected to be 10 s per decade. Potentiodynamic testing was performed over a voltage range from -1.5V to 2.0 V at a scanning rate of 1mV/s. The electrochemical measurements were conducted using a Gamry Reference 600™ Potentiostat in 7 wt.% NaCl solution. GamryEchem Analyst™ software was used to analyse potentiodynamic and EIS data.

### **5.3 Preparation of Smectic ZrP Nanoplatelets in Solvents and Epoxy**

Layered ZrP,  $\text{Zr}(\text{HPO}_4)_2 \cdot \text{H}_2\text{O}$ , (Figure 5.1), was synthesized with an average lateral diameter of 110 nm using a hydrothermal method. The hexagonal ZrP nanoplatelets have

strong covalent bonding along the primary plane, but interact with neighbouring platelets through weak out-of-plane van der Waals (vdW) and hydrogen bonding. These interactions result in the formation of layered tactoids with regular d-spacing of 0.76 nm prior to intercalation or exfoliation. The surface of each ZrP layer contains densely packed P-OH functional groups that interact strongly with proton-accepting functional groups (e.g., amines). As a result, the as-synthesized tactoids can be exfoliated or intercalated using various guest molecules. Here, the ZrP tactoids were exfoliated by proton exchange reaction with a commercially available polyoxyalkyleneamine in acetone.

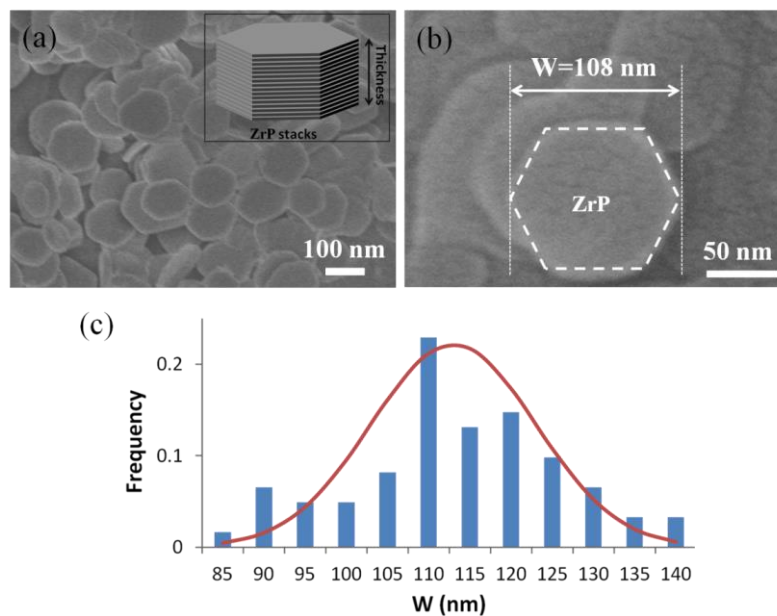


Figure 5.1 (a, b) SEM images and (c) size distribution of as-prepared ZrP nanoplatelets.



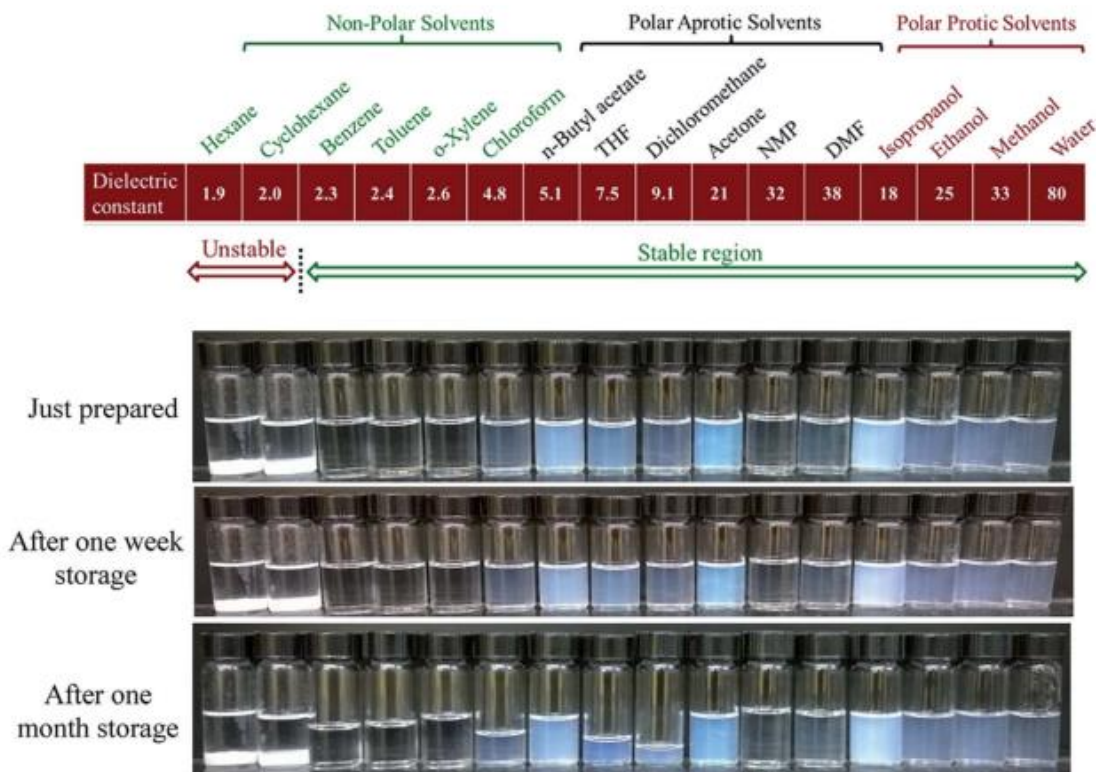


Figure 5.2 Stability of the Jeffamine M1000 modified ZrP with a concentration of 10 mg/mL in different solvents.

The oligomer modified ZrP were shown to be stable in most solvents investigated, with the exceptions of hexane and cyclohexane, which have extremely low dielectric constants (Figure 5.2). Amphiphilic Jeffamine M1000 is composed of hydrophobic propyleneoxide and hydrophilic ethyleneoxide blocks, which makes the Jeffamine M1000-modified ZrP stable in both organic and aqueous solvents. The liquid crystal behavior of ZrP in solvents with a concentration of 5.2 wt.% was studied using cross-polarized optical microscopy and SAXS. The strong birefringence indicates that there is long-range organization of the ZrP nanoplatelets into a liquid crystalline mesophase

(Figure 5.3). As shown in Figure 5.4, the microstructure of oligomer modified ZrP suspensions was characterized using SAXS. The results show a clear anisotropic scattering pattern, suggesting presence of lamellar organization of ZrP in both organic and aqueous solvents.

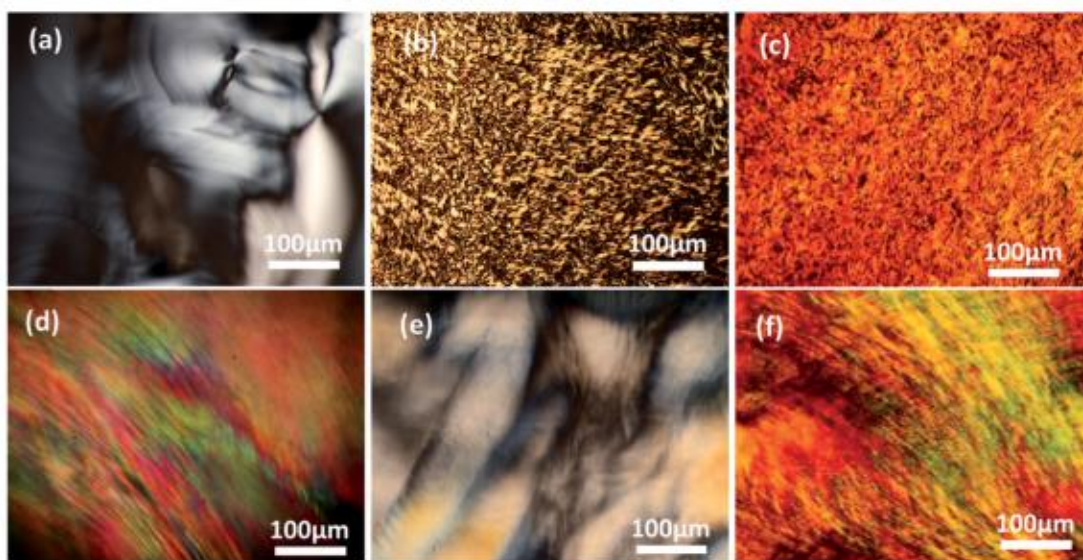


Figure 5.3 Cross-polarized light optical micrographs of the oligomer modified ZrP in various solvents showing strong birefringence including: (a) xylene, (b) water, (c) acetone, (d) ethanol, (e) DMF, and (f) THF, respectively.

The microstructure of the epoxy/ZrP liquids was quantitatively investigated using SAXS. SAXS measurements (Figure 5.5 (a, b)) on suspensions containing 4.5 vol.% ZrP show a strong anisotropic scattering pattern that suggests lamellar organization of ZrP in epoxy. The liquid crystal behavior of epoxy/ZrP liquid before addition of curing agent was investigated using cross-polarized light OM (Figure 5c). The epoxy/ZrP suspension

shows band-like birefringent features that are similar to Grandjean textures associated with a twisted-grain-boundary phase. The optical texture confirms that there is long-range organization of the ZrP nanoplatelets self-assembled into liquid crystalline mesophases.

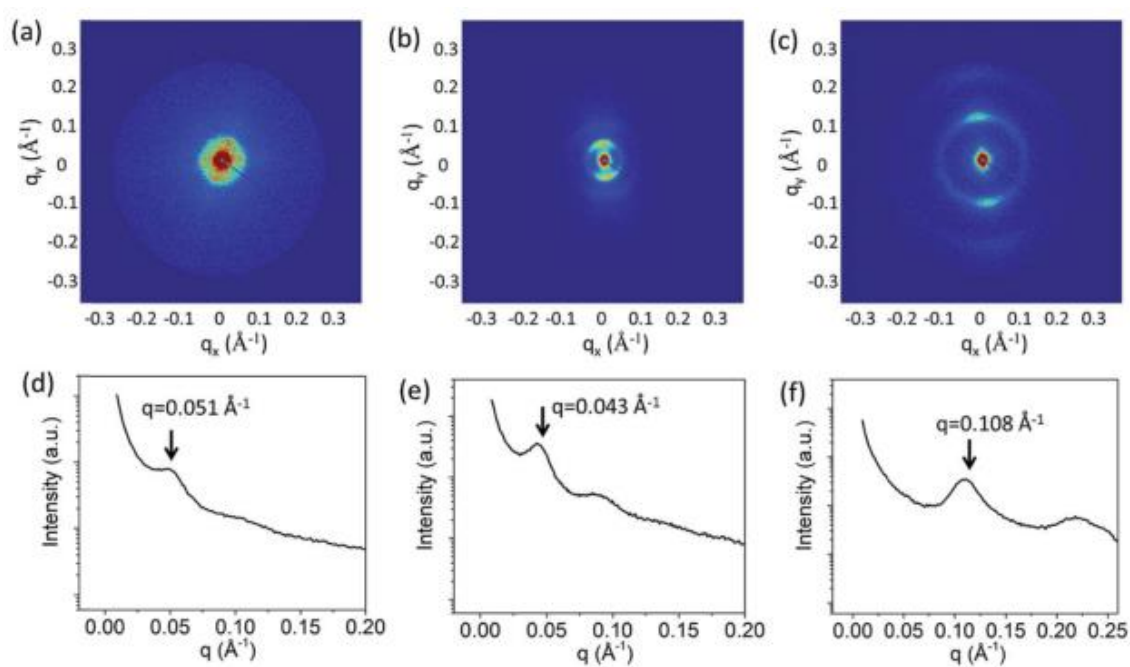


Figure 5.4 SAXS 2D and 1D diffractograms of the oligomer modified ZrP in various solvents including (a, d) xylene, (b,e) water, and (c,f)THF, respectively.

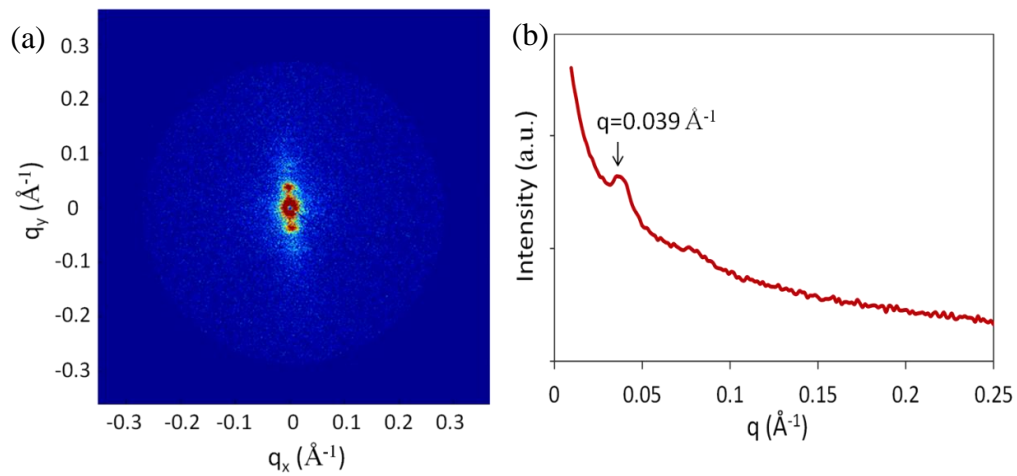


Figure 5.5 (a, b) SAXS 2D and 1D diffractograms of smectic epoxy/ZrP suspension.

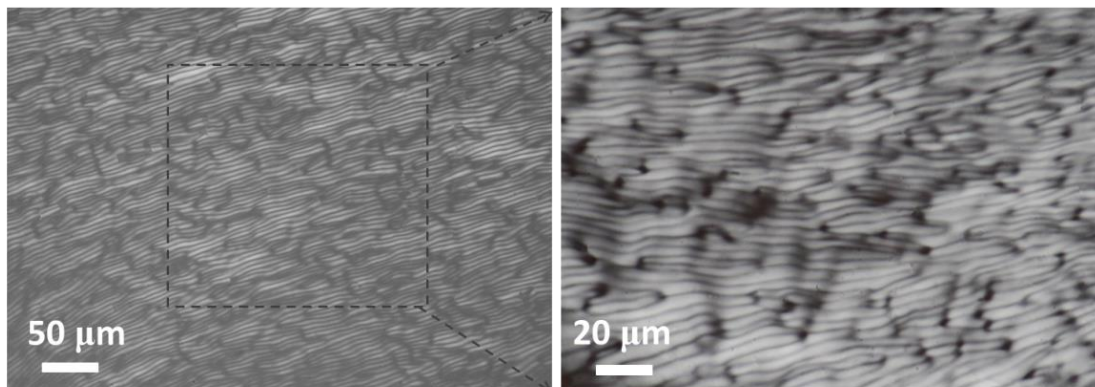


Figure 5.6 Cross-polarized light OM of epoxy/ZrP liquids at two magnifications.

#### **5.4 Anti-corrosion Epoxy Spray Coatings Containing Smectic ZrP**

The cost of metal corrosion in the United States in 2013 was estimated to exceed \$1 trillion.[157] A wide variety of anti-corrosion coating technologies have been developed to prevent or delay the damage, but are typically highly specific to certain substrates and alloys, costly, show limited robustness and stability, require extensive surface treatment, and contain materials damaging to the environment. For example, chromate-based coatings are a class of highly successful surface coatings for several corrosion-sensitive metals, but have been banned from use in many applications because of their toxicity and carcinogenic properties.[158] Zinc-based coatings are effective at preventing corrosion and are environmentally friendly, but are brittle and expensive. Zeolites, ceramics, and graphene[38,159-163] have been explored as corrosion-resistant coating materials, but have so far shown only limited success. Recently, a new generation of organic coatings has attracted significant attention due to the potential for facile fabrication and functionalization, and eco-friendly nature. Strategies[38,41,44,164-166] employed to prepare these new organic-based coatings include, but are not limited to, hydrophobic coatings to reduce accessibility of water to the metal surface, passive oxidation-enabled metal protection, and deposition of corrosion-inhibiting or ion-reactive nanoparticles. Several successful strategies have been reported, but often require extensive pre-treatment to promote adequate adhesion and corrosion resistance, and involve complex chemistries and processes. New anti-corrosion coatings that are able to

utilize existing industrial processing approaches, such as spray-coating, are in great demand.

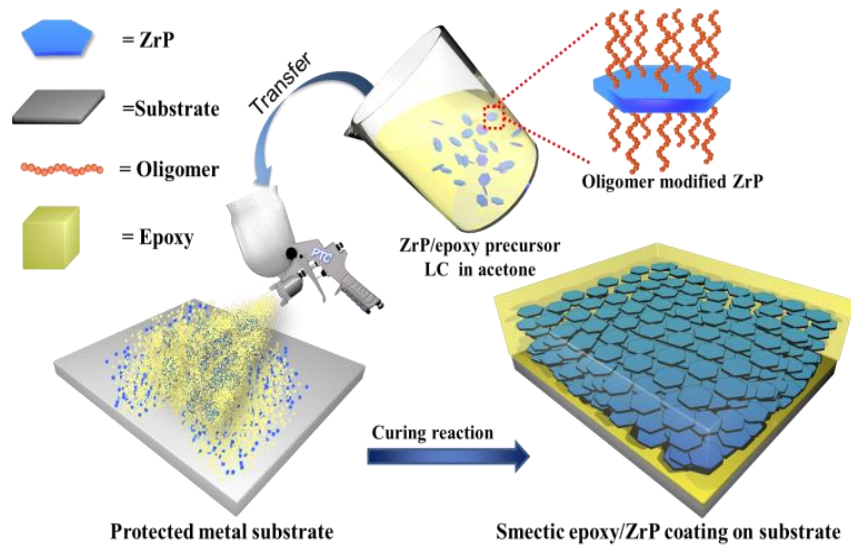


Figure 5.7 Schematic of the process used to prepare the smectic epoxy/ZrP coatings on a metal substrate.

A schematic showing the method to deposit 2D lamellar-like nanostructures consisting of exfoliated ZrP nanoplatelets on a metal substrate is shown in Figure 5.7. The mesoscale organization of the epoxy/ZrP coating on Al was investigated using GISAXS (Figure 5.8) and TEM (Figure 5.9). The high degree of order in the cured epoxy/ZrP (11 wt.%) coating on a metal substrate is supported by TEM images, which show long-range orientational and positional organization of the self-assembled ZrP nanoplatelets in smectic order. GISAXS measurements were carried out to quantitatively determine the orientation of the organized lamellar mesophase with respect to the metal



substrate. Lamellar structures aligned parallel to the substrate will display Bragg peaks along the vertical axis ( $q_z$ -axis). Peaks present along the horizontal plane ( $q_x$ -axis) indicate perpendicular alignment to the substrate. The Bragg peaks obtained from GISAXS 2D pattern (Figure 5.8) appear exclusively in the  $q_z$ -axis, indicating that the smectic ZrP nanoplatelets are predominantly aligned parallel to the substrate. The GISAXS 1D spectrum of the smectic epoxy/ZrP (11 wt.%) coating shows characteristic peaks corresponding to a lamellar phase with d-spacing of 6.1 nm.

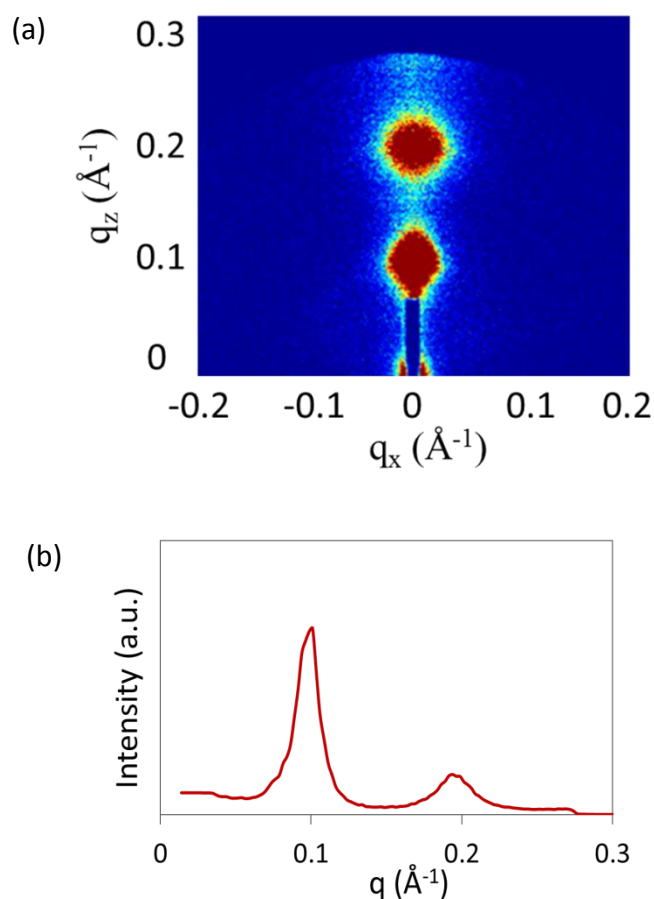


Figure 5.8 (a) 2D and (b) 1D diffractograms of GISAXS, suggesting ZrP nanoplatelets are aligned parallel to the metal substrate.

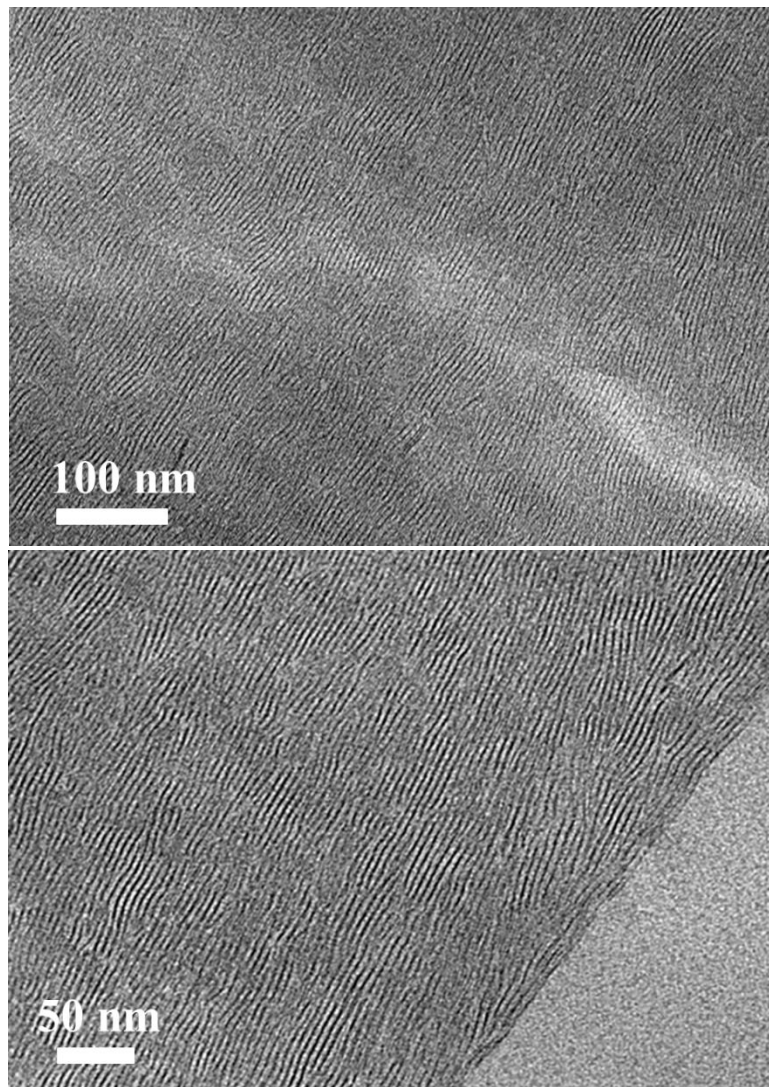


Figure 5.9 TEM of cross-section of smectic epoxy/ZrP coating.

The corrosion resistance of the coatings was investigated with potentiodynamic measurements (Figure 5.10). Two important parameters, corrosion potential ( $E_{\text{corr}}$ ) and corrosion current density ( $I_{\text{corr}}$ ), were measured to determine the corrosion resistance of the coated metal surfaces. The susceptibility of a surface to corrosion is typically



expressed by  $E_{\text{corr}}$ , and a positive shift in  $E_{\text{corr}}$  indicates an increase in corrosion resistance. The corrosion current density,  $I_{\text{corr}}$ , represents the intensity of the cathodic

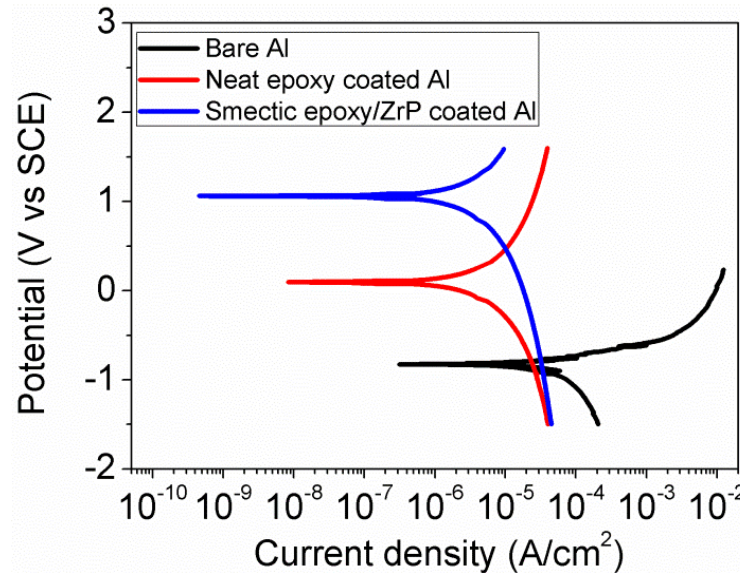


Figure 5.10 Potentiodynamic polarization results of bare Al alloy, neat epoxy, and smectic epoxy/ZrP-coated Al alloy.

oxygen reduction and anodic dissolution of metal ions.[158,167] The uncoated aluminum alloy (Al) substrate had an  $E_{\text{corr}}$  of -0.825 V. Coating the Al substrate with epoxy and epoxy/ZrP increased  $E_{\text{corr}}$  to 0.102 V and 1.068 V, respectively. At the same time,  $I_{\text{corr}}$  decreased from 29.41  $\mu\text{A}/\text{cm}^2$  for the bare Al, to 1.98  $\mu\text{A}/\text{cm}^2$  for the neat epoxy-coated Al, and finally to 0.36  $\mu\text{A}/\text{cm}^2$  for the smectic epoxy/ZrP-coated Al. Compared to the neat epoxy-coated Al, the smectic epoxy/ZrP-coated Al shows a 9.5 times increase in  $E_{\text{corr}}$  and an 80% reduction in  $I_{\text{corr}}$ . Previous reports indicate that at

low concentration of inorganic filler, most polymer/clay nanocomposites show very limited improvement in resistance to corrosion. In most cases, the limited performance is likely due to incomplete exfoliation, agglomeration, poor alignment, and low achievable volume fraction of the plate-like fillers. The present work is the first report of anti-corrosion properties of large-scale polymer/clay nanocomposites at high loadings that show liquid crystalline organization. The results show that the smectic epoxy/ZrP coatings fabricated here have excellent potential for anti-corrosion applications.

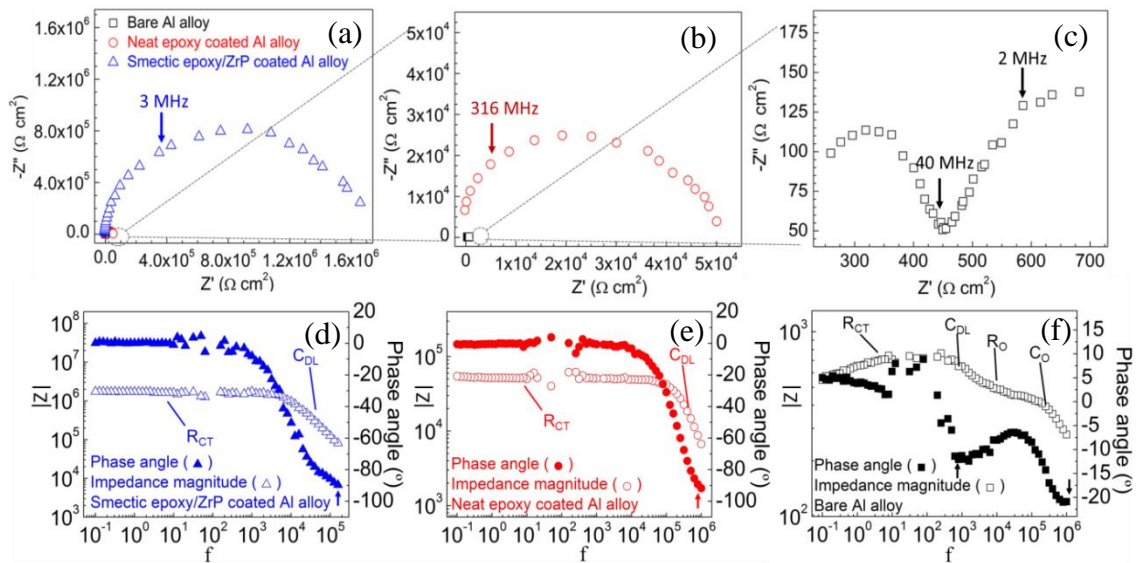


Figure 5.11 (a,b,c) Nyquist plots, and (d,e,f) Bode plots of bare Al alloy, neat epoxy, and smectic epoxy/ZrP-coated Al alloy.

Electrochemical impedance spectroscopy (EIS) experiments were carried out to better understand the underlying mechanisms responsible for the improved corrosion

resistance. The magnitude of the impedance was used to determine the resistance of the coating to the transportation of electrons and charges. Differences of several orders of magnitude in impedance were observed from the Nyquist plots (Figure 5.11 (a,b,c)), which clearly show that the impedance of smectic epoxy/ZrP coating is about 100-fold and 10,000-fold larger than those of the neat epoxy coating and bare Al substrate, respectively. The corresponding Bode plots are shown in Figure 5.11(d,e,f). Charge transfer ( $R_{CT}$ ) and double layer charging ( $C_{DL}$ ) are the two major electrochemical processes that occur during the corrosion of organic coatings protected Al. The Faradic current-induced charge transfer can be represented by the resistor component ( $R_{CT}$ ) without phase delay (phase angle = 0), which is shown in Figure 5.11(d,e). Surface charging due to the formation of a double layer (DL) can be denoted by the capacitor component ( $C_{DL}$ ) with a negative phase angle (see arrows in Figure 5.11(d,e)). On the bare Al surface, extra oxide components of resistor ( $R_O$ ) and capacitor ( $C_O$ ) are observed from the Bode plots (Figure 5.11(f)), in addition to the  $R_{CT}$  and  $C_{DL}$ . This is consistent with the two continuous semicircles in the corresponding Nyquist plot (Figure 5.11(c)). The phase delays associated with the two capacitor components are indicated by the two arrows in Figure 5.11(f). Impedance is inversely proportional to the surface charging capacitance. The highly aligned smectic epoxy/ZrP coating has a closely packed structure of inorganic platelets, which individually show favorable corrosion resistance. The low porosity of the smectic epoxy/ZrP coating reduces the extent of surface charging, which may contribute to the observed increase in impedance. The EIS results

indicate that the effective corrosion protection for the smectic epoxy/ZrP coating is primarily due to repression of both charge transfer and surface charging.

Metal corrosion involves destructive oxidative attacks caused by electrochemical reactions. In the case of the Al substrate, the corrosion process comprises anodic metal oxidation that releases soluble  $\text{Al}^{3+}$  ions and cathodic  $\text{O}_2$  reduction reactions that consume the electrons created from the anodic reaction. These two reactions complement each other. Inhibition of one of the two reactions will prevent or slow down the overall corrosion process. For metal corrosion to take place, electroactive species must penetrate through the coating. Therefore, a coating that inhibits oxygen permeation may lead to significantly improved corrosion resistance.

The oxygen transmission rate (OTR) and permeability of the neat epoxy and smectic epoxy/ZrP films are shown in Figure 5.12(a). The significant reduction of oxygen permeability was observed for the spray-coated smectic ZrP/epoxy film. Compared with the neat epoxy film with a thickness of  $\sim 130 \mu\text{m}$ , a 20-fold reduction in oxygen permeability is achieved with only a  $\sim 12 \mu\text{m}$  thick smectic ZrP/epoxy film at a relative humidity of 50%. According to the “tortuous pathway” concept, polymer composites containing impermeable platelets generate a brick wall structure. The penetrant can only wiggle through the permeable polymer gaps between the platelet layers. Thus, an increased aspect ratio and improved alignment of the nanoplatelets will significantly improve the gas barrier properties, leading to a greatly enhanced anti-corrosion performance (Figure 5.12(b)).

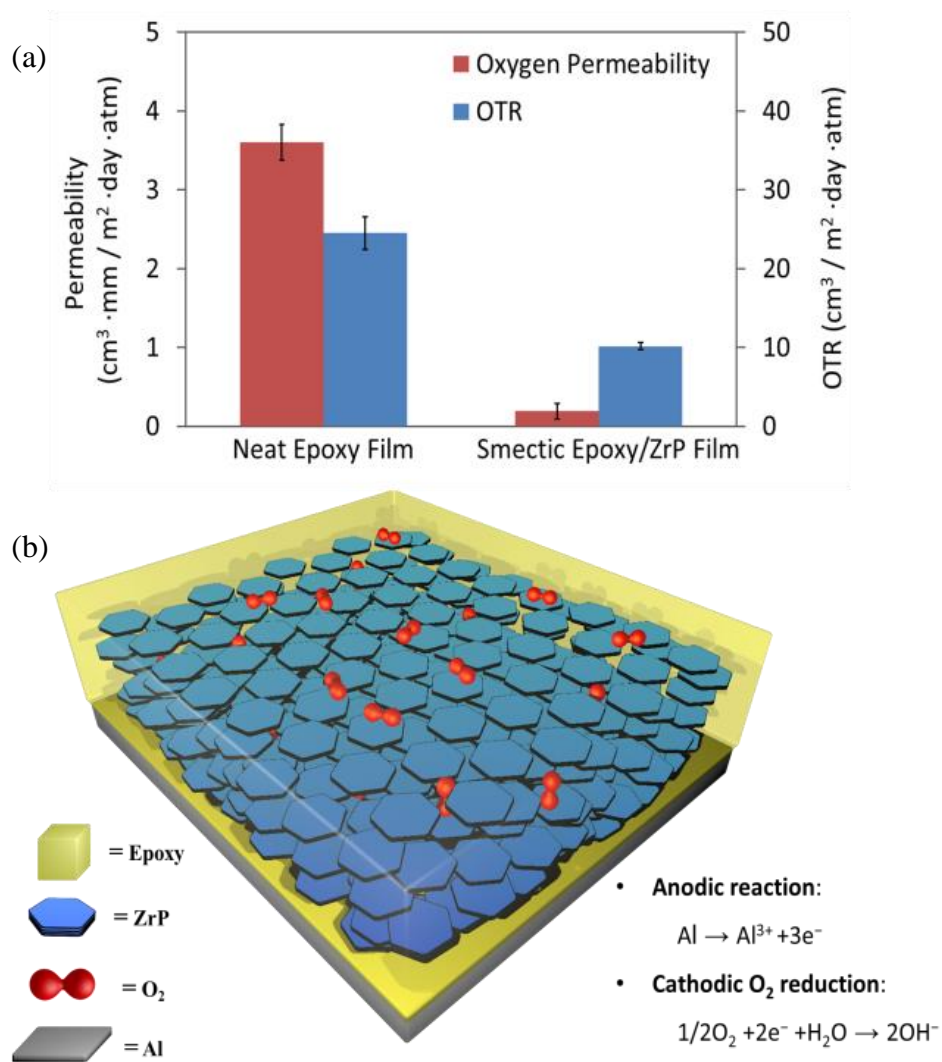


Figure 5.12 (a) Oxygen transmission rate (OTR) and permeability of neat epoxy and smectic epoxy/ZrP films tested under relative humidity of 50 RH% at 23°C. (b) Schematic of the improved barrier performance of aggressive oxygen.

The adhesion of anticorrosion coatings to metal substrates is of critical importance. The adhesion of the coatings were evaluated based on a standard method (ASTM D

3359-02). There was no detectable peeling of the smectic epoxy/ZrP coatings (Figure 5.13), indicating its good adhesion to the metal surface. After curing, there will be numerous ether and hydroxyl groups in unreacted epoxy segments, which may form hydrogen bonding with the available hydroxyl-terminated functional groups on the ZrP surface. Evidence for hydrogen bonding between ZrP and epoxy was found by comparing the FTIR spectra of neat epoxy and epoxy/ZrP nanocomposites (Figure 5.14). In the epoxy/ZrP nanocomposite, the absorption peak of -OH stretching is shifted from 3389cm<sup>-1</sup> to 3362cm<sup>-1</sup>. In general, a lower wavenumber in FTIR indicates strong hydrogen bonding interaction. The observed improvement in Ecorr for the smectic epoxy/ZrP coating is likely due to both the electrochemical stability and molecularly impermeable nature of the highly crystalline individual ZrP nanoplatelets, the strong interaction between the ZrP and the epoxy, and the high degree of alignment of alignment resulting from the self-assembled smectic mesoscale architecture.

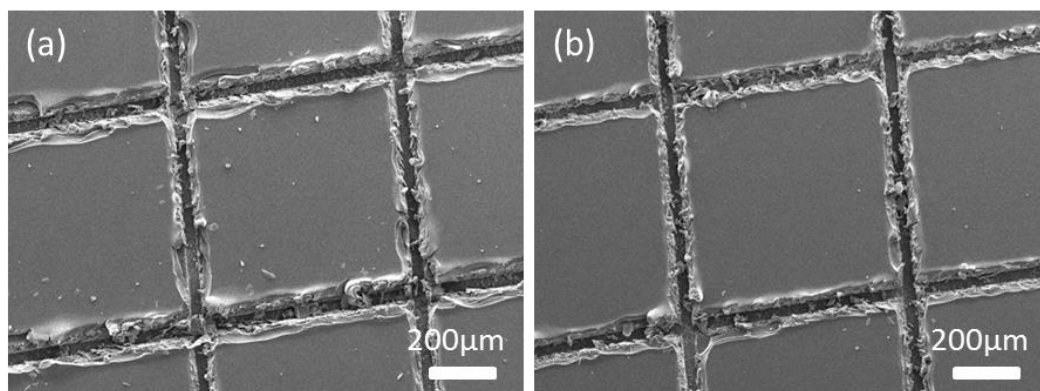


Figure 5.13 SEM images of (a) neat epoxy coating and (b) smectic epoxy/ZrP coating on the aluminum substrates after testing for evaluating adhesion according to ASTM standard D 3359-02.

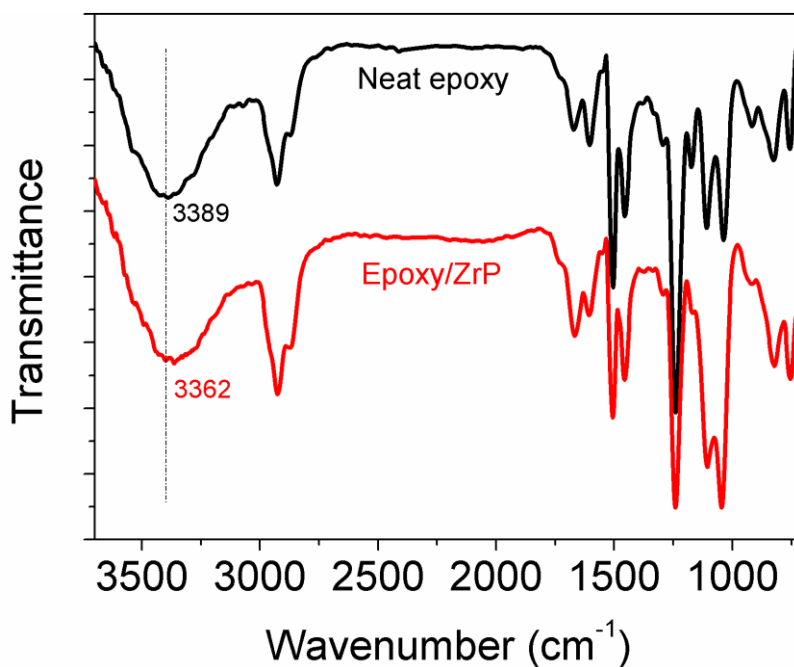


Figure 5.14 Fourier-Transform Infrared spectra (FTIR) of neat epoxy and smectic epoxy/ZrP nanocomposites.

One inherent limitation of the present spray-coating method is the use of a large amount of acetone as solvent, which has obvious environmental and health concerns. This concern may potentially be addressed by development of a water-borne coating system. To investigate the suitability of our oligomer modified ZrP for a different coating system, a series of Jeffamine M1000 exfoliated ZrP in various solvents were prepared (Figure 5.2-5.4). The oligomer modified ZrP were shown to be stable in most solvents investigated, with the exceptions of hexane and cyclohexane, which have extremely low dielectric constants. Amphiphilic Jeffamine M1000 is composed of hydrophobic propyleneoxide and hydrophilic ethyleneoxide blocks, which makes the

Jeffamine M1000-modified ZrP stable in both organic and aqueous solvents. The results show a clear anisotropic scattering pattern, suggesting presence of lamellar organization of ZrP in both organic and aqueous solvents. Further corrosion studies are being pursued to determine fundamental structure-property relationship on various coating systems that contain 2D layer structure with liquid crystalline order. Development of commercially viable coating systems for other applications, such as microelectronics encapsulation, food packaging, and infrastructure protection, will also be actively pursued.

## 5.5 Self-assembly Behavior of Oligomer Modified ZrP Nanoplatelets

### 5.5.1 Effect of Oligomers Tethered on ZrP Surfaces

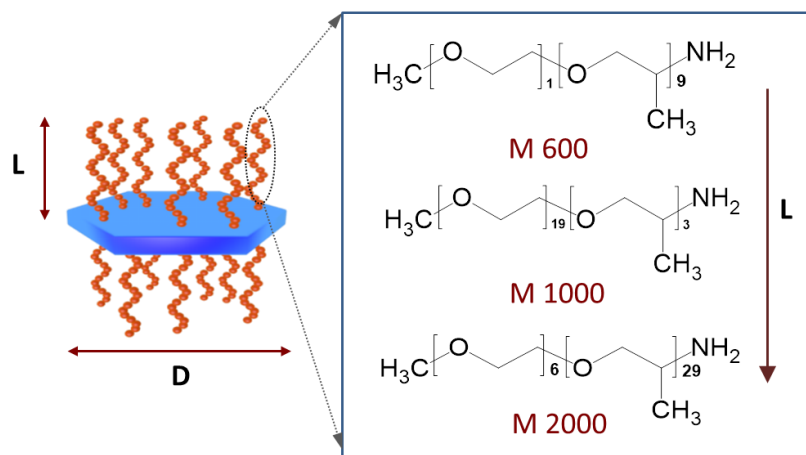


Figure 5.15 Schematic of surface modified ZrP nanoplatelets with various oligomers

There remain significant challenges is to understand the mechanism achieving large-scale highly ordered polymer/clay nanocomposites with multifunctionality, particularly



due to current limitations in the incorporation of high levels of nanoplatelets in polymer matrices without causing clay agglomeration or requiring sophisticated preparation process. In this section, we probe the effect of steric repulsion on the self-assembly behavior of ZrP nanoplatelet in polymeric matrix. Two parameters are considered here in order to vary the steric effect on the ZrP surface, i.e. oligomer grafting density and oligomer size. For this purpose, ZrP nanoplatelets with aspect ratio of 160 were functionalized using different oligomers. Three types of oligomers, namely Jeffamine M600 ( $M_w=600$ ), M1000 ( $M_w=1000$ ), and M2000 ( $M_w=2000$ ) (in Figure 5.15) are selected for the investigation of the effect of tethered oligomers on ZrP self-assembly behavior in an epoxy matrix. Long-range smectic phases are rarely seen and tend to be present only at high volume fractions, when there are long range repulsive interactions between nanoplatelets. We previously reported that M1000 modified ZrP formed long-range smectic order in epoxy matrix above the critical volume fraction of 2.9 vol%. Based on those previous work, we prepare the samples with volume fraction above the critical value, characterize the grafting density and hydrodynamic size by TGA and DLS and investigate the corresponding self-assembly behavior by TEM. Through the comparison of self-assembly behavior using ZrP/M600 and ZrP/M2000 with the reported behavior using ZrP/M1000 in the same polymer matrix, the effect of steric repulsion will be elucidated.

TEM results in Figure 5.16 indicate that M600-ZrP with a concentration of 4.1 vol% forms aggregated local domains in epoxy. From a higher magnification TEM image,

each local domain contains several individual ZrP layers to tens of layers. Such micromorphology demonstrates that the self-assembly of M600-ZrP individual layers in epoxy forms aggregated microphases without the presence of long-range ordering. . As a comparison, micromorphology of oligomer M2000 modified ZrP in epoxy is characterized by cross-polarized light OM, SAXS, and TEM (in Figure 5.17). The lyotropic behavior of the M2000-ZrP /epoxy suspension sample, which is prepared without adding curing agent and sandwiched between two glass plates, can be observed under cross-polarized light (Figure 5.17a). The obvious birefringent behavior in such sample demonstrates the existence of orientation of ZrP nanoplatelets in epoxy precursor. The band-like birefringent features are similar to Grandjean textures associated with a twisted-grain-boundary phase. The SAXS results in Figure 5.17b confirm the smectic characteristics of the M2000-ZrP /epoxy composites. Micromorphology of oligomer M2000 modified ZrP in epoxy with a concentration of 3.6vol% is characterized by TEM (Figure 5.17c) in which exfoliated M2000-ZrP exhibit long-range smectic order. According to the anticipated scaling for a lamellar system with infinite aspect ratio, as concentration increases, the distance between layers (D) decreases and roughly follows:  $D = T_{zrp} / \text{vol}\%$  Where  $T_{zrp}$  is the thickness of an individual ZrP nanoplatelet ( $\sim 0.69$  nm) and vol% is the volume fraction of ZrP. The measurements show a smaller d-spacing than predicted value, which is attributed to the finite lateral separation between platelets within layers.

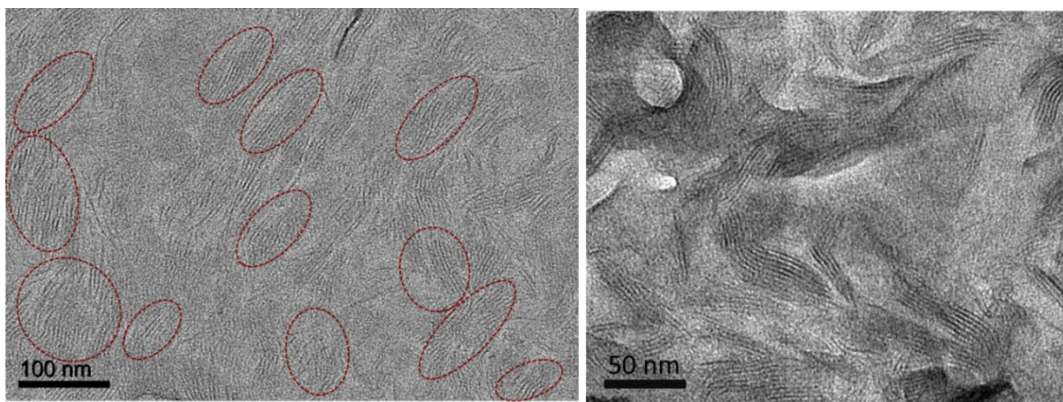
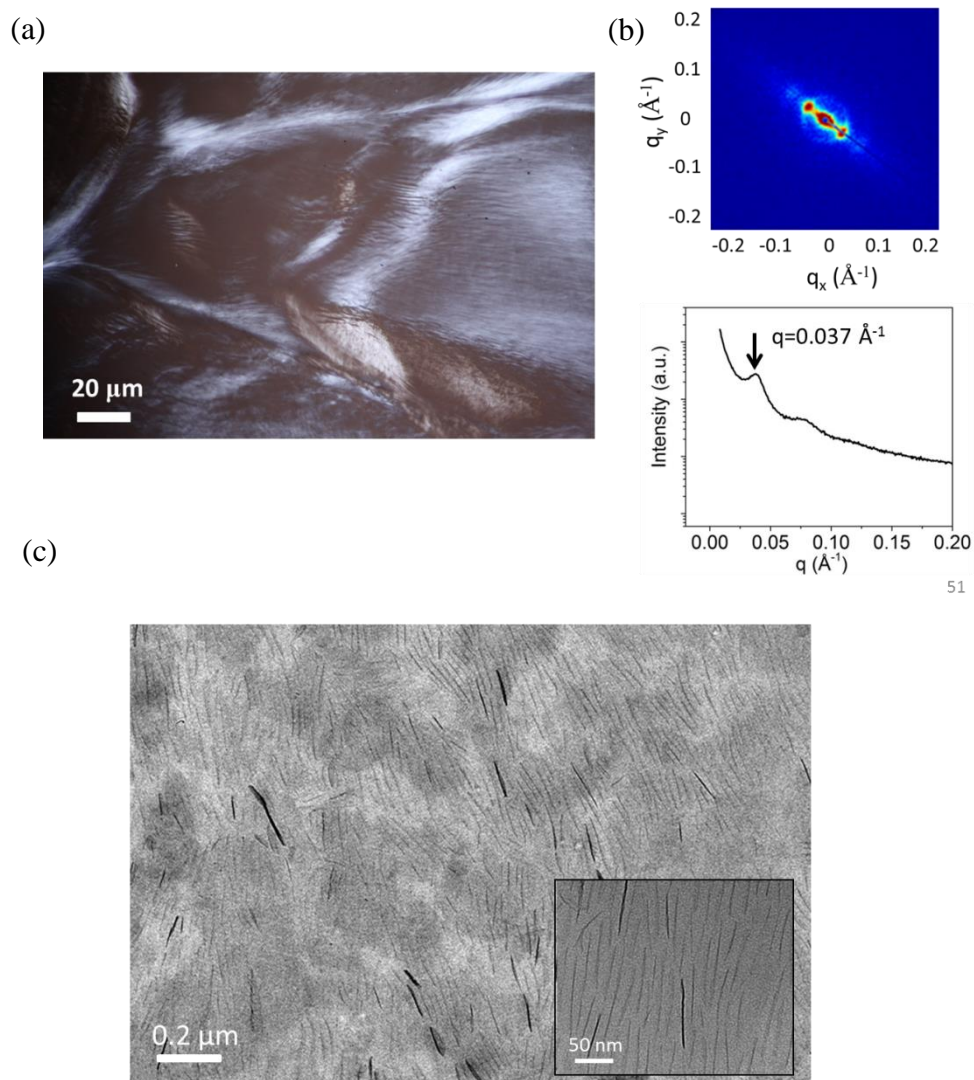


Figure 5.16 TEM of oligomer M600 modified ZrP in an epoxy matrix. Red circles show the ZrP local domain.

In order to qualitatively characterize the oligomer size on ZrP surfaces, dynamic light scattering (DLS) were carried out based on exfoliated ZrP modified by various oligomers including M600, M1000, and M2000. DLS results (Figure 5.18) suggest the hydrodynamic size ( $D$ ) of oligomer modified ZrP gradually increases from using M600 to M1000 to M2000 ( $D_{M600} < D_{M1000} < D_{M2000}$ ). As our synthesis method provides a well controlled aspect ratio and the ZrP individual layer thickness is the same 0.69 nm for all the three types of samples, it is obvious that the trend of hydrodynamic size from  $D_{M600}$  to  $D_{M2000}$  is due to the change of oligomer size grafted on the ZrP surface, which follow the same trend with oligomer molecular weights. Furthermore, the grafting density of oligomers tethered on ZrP surfaces was characterized using thermogravimetric analysis (TGA). TGA measurements of neat oligomers and oligomer modified ZrP were carried out in air testing conditions. Figure 5.19 (a) shows that the three types of neat oligomers are all completely decomposed without any residents after



51

Figure 5.17 (a) cross-polarized light OM and (b) SAXS of ZrP-M2000/epoxy suspensions (c) TEM of oligomer M2000 modified ZrP in an epoxy matrix after curing.

heating up to 600°C. In the case of oligomer-functionalized ZrP system (Figure 5.19 b), the weight fraction of oligomers on ZrP is determined from solid residue after high temperature treatment. The solid residue of oligomer-modified ZrP at 800 oC treatment

is zirconium pyrophosphate ( $\text{ZrP}_2\text{O}_7$ ). The equivalent ZrP mass fraction was converted according to the stoichiometric ratio of  $\text{ZrP}/\text{ZrP}_2\text{O}_7 = 1.136$ . Oligomer grafting density ( $\tau$ ) is expressed in unit of  $1/\text{nm}^2$  and defined as following:

$$(5.1) \quad \tau = \frac{(m_{\text{oligomer}}/M_{\text{oligomer}}) \times N_A}{(m_{\text{ZrP}}/(\rho_{\text{ZrP}} \times T_{\text{ZrP}})) \times 2}$$

where  $m_{\text{oligomer}}$  and  $M_{\text{oligomer}}$  is the mass and molecular weight of oligomers, respectively;  $m_{\text{ZrP}}$ ,  $\rho_{\text{ZrP}}$  ( $2.76\text{g}/\text{cm}^3$ ) and  $T_{\text{ZrP}}$  ( $0.69\text{ nm}$ ) is the mass, density, and thickness of ZrP;  $N_A$  is Avogadro constant. The detailed information is summary in Table 1. It suggests that oligomer grafting density ( $\tau$ ) decreases as the oligomer molecular weight increases ( $\tau_{M2000} < \tau_{M1000} < \tau_{M600}$ ). This phenomenon could be explained as large-sized oligomers limit contact opportunities between intercalating oligomers and active functional groups on ZrP surface.

Steric effect is one of the effective tools applied to govern the colloidal self-organization process of colloidal nanoplatelets. Factors such as an increase in the density of grafted oligomers or the size of the oligomer chains, which produce an effective steric repulsion between the particles, contribute to the stabilization of the colloidal suspension. Theoretically, it has been demonstrated that by increasing the length of the oligomer chains tethered on nanoparticle surfaces with fixed number of chains per unit area on the particles, the steric repulsion increases. Also, if the length of the chains is kept fixed but the grafting density of chains per particle increases, the repulsive steric interaction is enhanced. In our systems, there is significant steric interaction between oligomer

modified ZrP nanoplatelets. Our results indicate that larger oligomer size ( $D_{M2000}$ ) with less grafting density ( $\tau_{M2000}$ ) may provide sufficient steric repulsion than the case in which the grafting density is higher ( $\tau_{M600}$ ) but the size is smaller ( $D_{M600}$ ). In other words, the oligomer size effect could act as a predominant factor for the steric repulsion which affects the self-assembly behavior of 2D platelet.

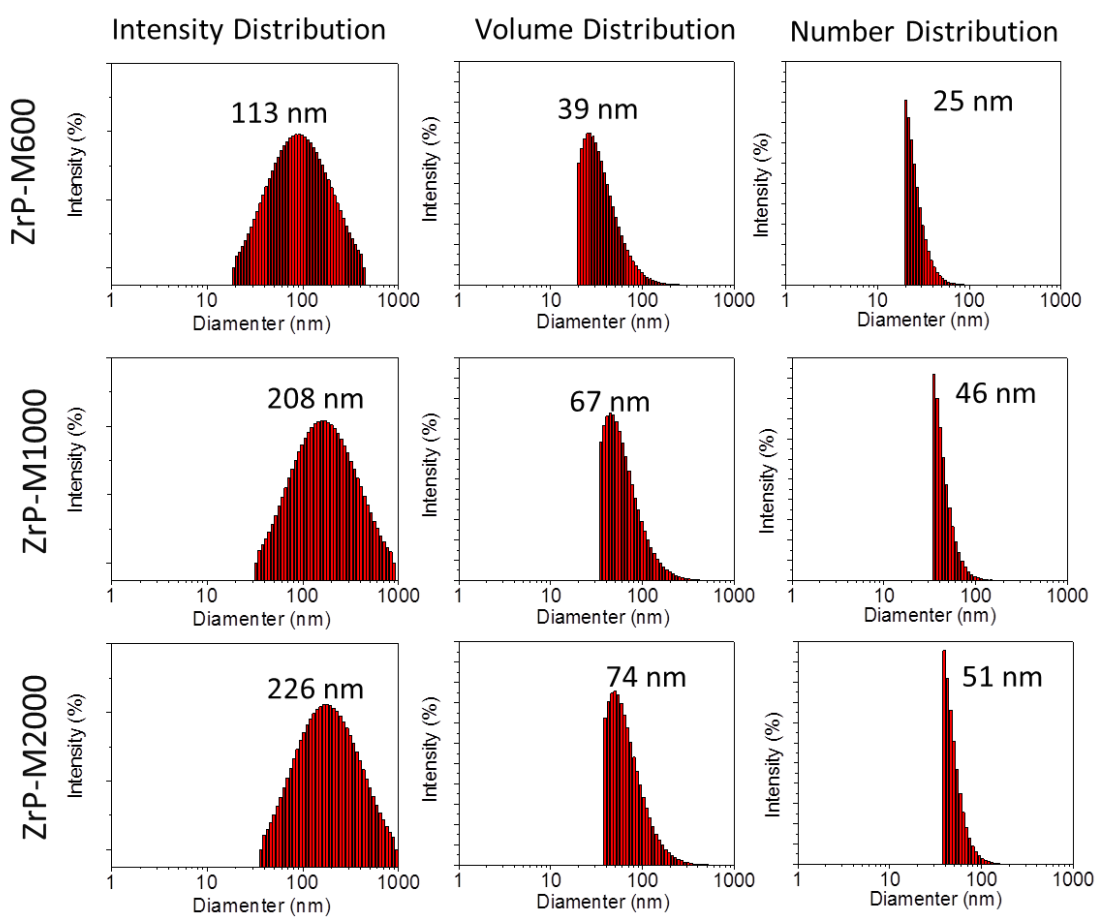


Figure 5.18 DLS of ZrP nanoplatelets modified by various oligomers including M600, M1000 and M2000.

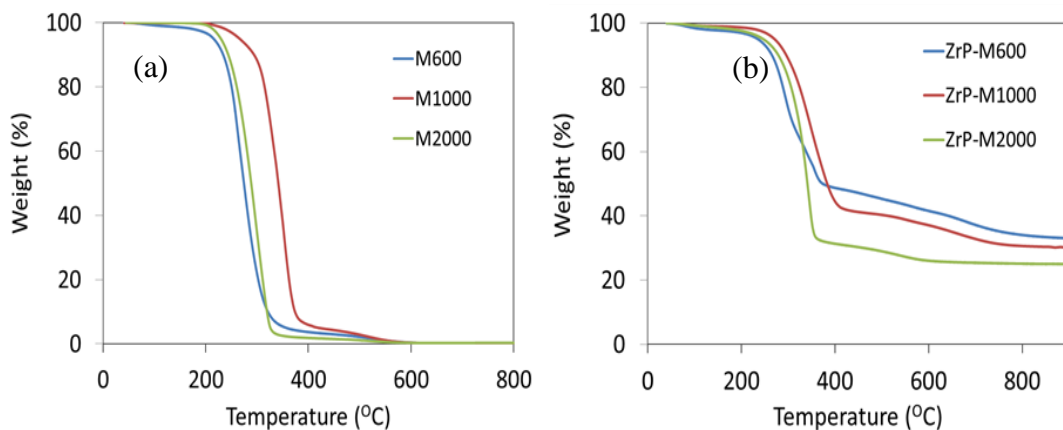


Figure 5.19 TGA results of neat oligomers (a) and oligomer modified ZrP (b) under air flow condition.

Table 5.1 TGA summary information of ZrP ( $\alpha=160$ ) modified by various oligomers.

	ZrP-M600	ZrP-M1000	ZrP-M2000
ZrP <sub>2</sub> O <sub>7</sub> (wt.%)	32.8%	30.1%	25.1%
ZrP (wt.%)	37.3%	34.2%	28.5%
Oligomer (wt.%)	62.7%	66.8%	71.5%
$\tau$ (chains/nm <sup>2</sup> )	1.19	0.77	0.41

### 5.5.2 Effect of ZrP Aspect Ratio

The effect of ZrP aspect ratio is investigated in this part in order to vary the nanoscale interaction between the ZrP platelet. We choose to use the same oligomer (M1000) to modify different sized ZrP surfaces. According to Onsager's theory [9], high aspect ratio particles tend to form liquid crystal phases above a critical volume fraction due to a net gain in entropy as the loss of orientational entropy is compensated by an increase in translational entropy. It was reported that large-sized ZrP exfoliated with M1000 oligomers self-assemble into a long-range smectic liquid crystal mesophase in solvents. The interlayer d-spacing is in the range of 120 nm to 240nm corresponding to the ZrP volume fraction from 0.11% to 0.45%. However, the phase transition of large-aspect-ratio ZrP nanoplatelets in a polymer matrix is less understood especially at high ZrP loadings.

In the present work the surface of large-sized ZrP with an aspect ratio ( $\alpha$ ) of 850, functionalized using exactly the same oligomers M1000 as small-sized ZrP ( $\alpha=160$ ) (Figure 5.20 a,b) that is discussed in the previous section. The micromorphology of high-aspect-ratio ZrP in epoxy was characterized by TEM and XRD as shown in Figure 5.20c. It shows that large-sized ZrP with a filler concentration of 3.5 vol% form obvious aggregated phases in an epoxy matrix. The grafting density of oligomers tethered on high-aspect-ratio ZrP surfaces was characterized using TGA (Figure 5.21). Interestingly, the TGA results indicate that the grafting density ( $\tau$ ) of M1000-oligomers retain similar



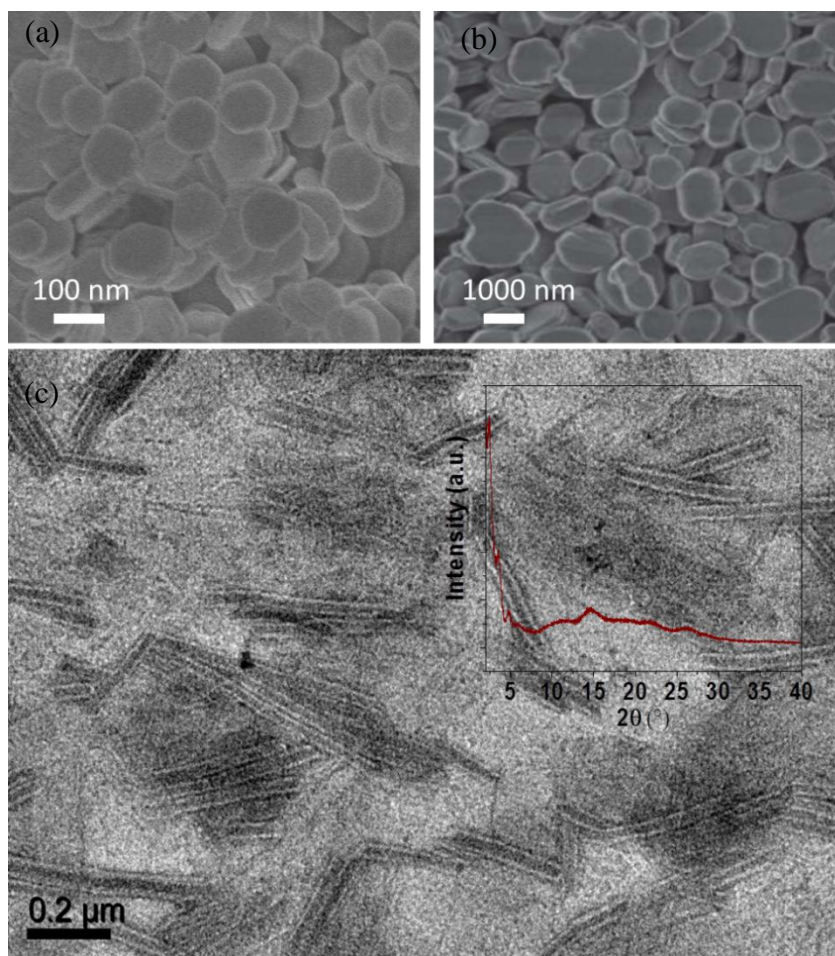


Figure 5.20 SEM of ZrP with small (a) and large (b) aspect ratio; (c) TEM and XRD of M1000 modified ZrP with large size in epoxy.

levels on surfaces of different sized ZrP (Table 5.2), with a variation as low as 4.9%. Even though the grafting density of ZrP with  $\alpha= 850$  and ZrP with  $\alpha= 160$  are not exactly the same, the remarkable change in the micromorphology is unlikely due to the insignificant difference in the grafting density. Especially, taking into account the fact that the self-assembled nanostructures in essence are ruled by the balance between

attractive force and repulsive force, knowing that the steric effect with provided by M1000 on ZrP with  $\alpha= 850$  and ZrP with  $\alpha= 160$  are of the same level, it is thus rational to consider that the attractive force has been significantly enhanced when using larger size nanoplatelet for self-assembly.

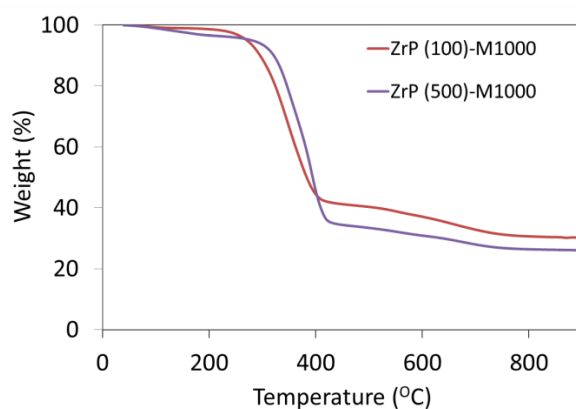


Figure 5.21 TGA results of M1000 modified ZrP with different aspect ratio under air flow condition.

Table 5.2 TGA summary information of M1000 modified ZrP with different aspect ratio.

	ZrP-Small	ZrP-Large
ZrP <sub>2</sub> O <sub>7</sub> (wt.%)	30.1%	26.1%
ZrP (wt.%)	34.2%	29.6%
Oligomer (wt.%)	66.8%	70.4%
$\tau$ (chains/nm <sup>2</sup> )	0.77	0.81

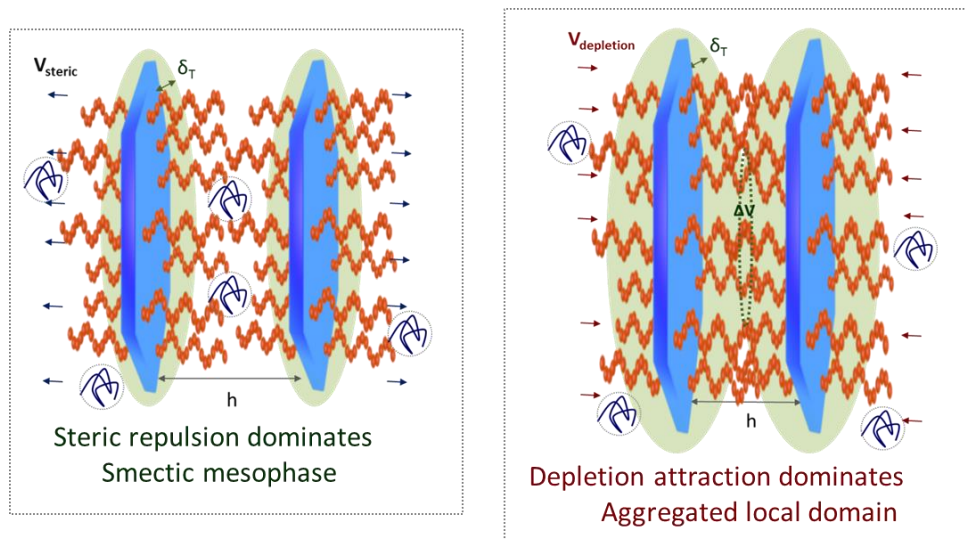


Figure 5.22 Possible self-assembly behavior of oligomer modified ZrP in epoxy dominated by different interaction potentials. Where  $\delta_T$  is depletion thickness;  $h$  is distance between nanoplates;  $\Delta V$  is entropy-driven extra free volume.

Self assembly behavior in principle is governed by the balance between various interactions at nanoscale, such as steric interaction, depletion interaction, etc. The schematic in Figure 5.22 shows possible self-assembly behavior of oligomer modified ZrP dominated by different interaction potentials. Specifically, as repulsive steric interaction dominates long-range smectic order of colloidal ZrP nanoplatelets tends to form in an epoxy matrix. In contrast aggregated ZrP local domains appear as attractive depletion interaction dominates. The approach of tethering oligomer brushes on nanoparticle surfaces to create efficiently repulsive steric interaction has long been used to stabilize and assemble colloidal nanoparticles. Theoretically, the nanoscale steric repulsion induced by oligomer brushes has been intensively studied through various methods such as self-consistent field theory, scaling theory, Monte Carlo theory [12].

Steric interaction increases upon compression due to the increase in osmotic pressure within brushes overlapping region. The increased osmotic pressure is due to the unfavorable exclusion of solvent molecules in the oligomer overlapping region. The repulsive interaction potential significantly is proportional to oligomer length and surface grafting density on nanoplatelet surfaces.

The aggregation of high-aspect-ratio ZrP in epoxy could be explained by increased depletion attraction. The concept of depletion interaction was first explained by Asakura and Oosawa using a model of large hard sphere particles immersed in a solution containing small solute particles [17]. Entropy-driven extra free volume develops when large particles get so close that no solute molecules occupy the region between them. The attractive depletion interactions occur due to net entropy gained and push spheres towards to each other. Essentially entropic depletion interaction is able to be tuned by varying the aspect ratio of ZrP nanoplatelets. In the same colloidal system in terms of particle volume fraction and depletion agent type, an increase in ZrP aspect ratio results in a decrease in total free volume due to stronger steric hindrance of depletion agents for diffusing into ZrP nanoplatelet gallery. As a result, the increased attractive depletion interaction driven by entropy leads to the formation of ZrP aggregation.

## **5.6 Conclusion**

Epoxy nanocomposite coatings containing self-assembled  $\alpha$ -zirconium phosphate nanoplatelets (ZrP) in smectic order were successfully prepared using a simple, energy-

efficient spray-coating fabrication process. Lyotropic liquid crystal behaviour of ZrP nanoplatelets was observed in a number of different solvents, which suggests the phenomena are largely entropically driven and would be suitable for various coating systems. ZrP aspect ratio, surface functionalization, and nanoscale interaction potentials are among the key factors responsible for the colloidal self-assembly process. The potentiodynamic polarization and EIS experiments show that the smectic epoxy/ZrP coatings can effectively repress corrosion reactions. The findings have broad implications for fabricating multi-functional polymer nanocomposites containing highly aligned nanoplatelets for engineering applications.

## **CHAPTER VI**

### **CONCLUSION AND FUTURE WORK**

#### **6.1 Summary**

The research efforts in this dissertation focus on dispersion stability and colloidal self-assembly of two-dimensional nanoplatelets in solvent and polymers. Phase transition behavior and fundamental principles responsible for the formation of long-range liquid crystalline order of nanoplatelets are investigated. The relationship between ordered mesophase and functional properties is also studied. A summary of the results for the individual systems is give as follows.

In Chapter II, a direct colloidal self-assembly approach was utilized to prepare photonic crystals based on exfoliated graphene oxide (GO) in aqueous solution. The GO sheets form ordered photonic structure spontaneously without the need for multiple processing steps. The wavelength of light reflected by the GO photonic crystal dispersion can be controlled over the entire visible light spectrum simply by varying the GO concentration. The aspect ratio of the GO sheets and mediation of the intersheet forces are found to be the key factors influencing the stability of photonic crystal formation. The current study may significantly broaden the utilization of GO-based materials for advanced device applications.

In Chapter III, epoxy nanocomposite spray-coatings containing large aspect ratio modified graphene (MG) were successfully prepared in a facile manner. The individually exfoliated MG nanosheets form liquid crystalline mesophases in epoxy precursor at low loadings. The epoxy/MG nanocomposite films exhibit significantly improved gas barrier properties even in humid conditions. The spray-coating method allows for the preparation of high MG content nanocomposites in large scale without compromising processability. These highly desirable packaging properties make graphene-based epoxy nanocomposites attractive for high performance multifunctional packaging applications.

In Chapter IV, thermally stable and highly conductive films have been prepared based on thermally reduced graphene oxide and exfoliated zirconium phosphate nanoplatelet (ZrP) hybrids. Exfoliated ZrP and graphene oxide (GO) were first mixed in aqueous solution to form a stable dispersion and then cast into free-standing films through flow-directed assembly. Upon annealing at 750 °C in Argon atmosphere, significant amounts of oxidized species were removed from the GO and a noticeable recovery of  $sp^2$  structure of the reduced GO sheets was observed. With the incorporation of the inorganic nanoplatelets, the thermal stability and structural integrity of the hybrid films were greatly improved, while the good electrical conductivity of the reduced GO was maintained.

In Chapter V, A simple and an effective self-assembly approach has been developed to fabricate epoxy nanocomposite films containing ZrP nanoparticles in smectic order.

Lyotropic liquid crystal behavior of ZrP nanoplatelets was observed in a number of different solvents, which suggests the phenomena are largely entropically driven and would be suitable for various coating systems. It was demonstrated that polymer nanocomposites with high filler content may be prepared without compromising processability. Long-range orientational and positional arrangement of ZrP nanoplatelets in smectic order is readily observed in epoxy nanocomposite films, which is characterized by TEM, X-ray scattering, and cross-polarized light OM. ZrP aspect ratio, surface functionalization, and nanoscale interaction potentials are among the key factors responsible for the colloidal self-assembly process. The potentiodynamic polarization and EIS experiments show that the smectic epoxy/ZrP coatings can effectively repress corrosion reactions. The results show that the epoxy coatings containing highly aligned ZrP nanoplatelets in smectic order may be used to effectively protect metal surfaces from corrosion using a scalable and simple approach. The compatibility of the self-assembling ZrP nanoplatelets in various organic and aqueous solvents will further broaden the practical significance of the present approach.



## **6.2 Recommended Future Research Work**

### **6.2.1 Self-assembly and Phase Transition of Colloidal Nanoplatelets**

Colloidal self-assembly of two-dimensional ZrP nanoparticles into liquid crystalline phases from isotropic to nematic to smectic order have been systematically investigated in organic solvents and epoxy. These oligomer modified nanoplatelets self-organized into long-range ordered mesophases upon increasing ZrP concentration. Oligomer grafting density, oligomer size and nanoscale interaction between ZrP platelets play an important role for the resulting micromorphology in an epoxy matrix. However phase transition of ZrP nanoplatelets in thermoplastic polymer matrices e.g., poly(methyl methacrylate) (PMMA) is less understood. According to the nanoscale depletion interaction theory, the phase transition of nanoplatelets is in function of polymer molecular size. It is recommended to design experiments using oligomer modified ZrP nanoplatelets in polymer matrices of various molecular sizes to verify theoretical simulations.

### **6.2.2 Functional Properties of Composites Containing Smectic Clay**

A simple and effective self-assembly approach has been developed to fabricate epoxy nanocomposites containing ZrP nanoparticles in smectic order. Moreover the fabrication method presented in this dissertation is flexible to different systems. Long-range orientational and positional arrangement of ZrP nanoplatelets in solvents and polymer

matrices would provide a number of unique physical and chemical properties. It has been demonstrated that smectic epoxy/ZrP composites show outstanding barrier properties against oxygen, low viscosity under shear, superb mechanical rigidity and strength, as well as corrosion resistance. More effects is recommended to explore novel functionality including:

- Design high-performance polymer/clay nanocomposites with improved thermal stability and flame retardancy
- Develop zirconium phosphate nanoplatelets based novel lubricant additives for engineering oils
- Formulate nanoplatelet based multifunctional inks for 3-dimensional printing. ZrP nanoplatelet server mainly as rheology modifier.
- ZrP as a model nanoplatelet has been fundamentally studied for colloidal self-assembly behavior. Other inexpensive and plentiful nanoplatelets would be recommended for practical applications.

## REFERENCES

- [1] M.C. Mourad, E. Groeneveld, H. Lekkerkerker, *J. Mater. Chem.* 18 (2008) 3004.
- [2] M.C. Mourad, A.V. Petukhov, G.J. Vroege, H.N. Lekkerkerker, *Langmuir* 26 (2010) 14182.
- [3] J. Gabriel, F. Camerel, H. Desvaux, P. Davidson, P. Batail, *Nature* 413 (2001) 504.
- [4] J. Lahiri, L. Isaacs, B. Grzybowski, J.D. Carbeck, G.M. Whitesides, *Langmuir* 15 (1999) 7186.
- [5] L. Rossi, S. Sacanna, W. Irvine, P.M. Chaikin, D.J. Pine, A.P. Philipse, *Soft Matter* 7 (2011) 413.
- [6] N. Ise, I.S. Sogami, Springer, New York (2005).
- [7] C. Cheng, D. Li, *Adv. Mater.* 25 (2012) 13.
- [8] D.H.J. Napper, *Colloid Interface Sci.* (1977) 390.
- [9] L. Onsager, *Ann. N.Y. Acad. Sci.* 51 (1949) 627.
- [10] P.G. Gennes, *Adv. Colloid Interface Sci.* 27 (1987) 189.
- [11] J.U. Kim, M.W. Matsen, *Macromolecules* 41 (2008) 4435.
- [12] S. T. Milner, T. A. Witten, M. E. Cates, *Macromolecules* 21 (1988) 2610.
- [13] M. Rubenstein, R. H. Colby, *Polymer Physics*, Oxford University, Press, Oxford, UK (2003).
- [14] J. Mewis, W.J. Frith, W.B. Russel, *Aiche J.* 35 (1989) 415.
- [15] S. T. Milner, *Europhys. Lett.* 7 (1988) 695.

- [16] S. Asakura, F. Oosawa, *J. Chem. Phys.* 22 (1954) 1255.
- [17] S. Asakura, F. Oosawa, *J. Polym. Sci.* 33 (1958) 183.
- [18] P.D. Kaplan, J.L. Rourke, D.J. Pine, *Phys. Rev. Lett.* 72 (1994) 582.
- [19] S. Abbas, T. P. Lodge, *Phys. Rev. Lett.* 99 (2007) 4.
- [20] B. Dmitry, M. Liberato, R. Cingolani, L. Manna, *Nano, Lett.* 10 (2010) 743.
- [21] R. Laura, P.P. Albert, D.J. Pine, A.P. Philipse, *Soft Matter* 7 (2011) 4139.
- [22] Y. Kim, Y. Li, W. Pitts, Werrel, *ACS Appl. Mater. Interfaces* 6 (2014) 2146.
- [23] Y. Dou, S. Xu, X. Liu, X. Duan, *Adv. Funct. Mater.* 24 (2014) 514.
- [24] S. Phua, L. Yang, C. Toh, S. Lau, A. Dasari, X. Lu, *ACS Appl. Mater. Interfaces* 5 (2013) 1302.
- [25] T. Ebina, F. Mizukami, *Adv. Mater.* 19 (2007) 2450.
- [26] H.F. Lee, P. D. Rodgers, W. R. Paul, *Polymer* 46 (2005) 11673.
- [27] T.D. Fornes, D.R. Paul, *Polymer* 44 (2003) 4993.
- [28] P. Podsiadlo, A. Kaushik, E. Arruda, A. Waas, N. Kotov, *Science* 318 (2007) 80.
- [29] A. Walther, I. Bjurhager, J. Malho, J. Ruokolainen, O. Ikkala, *Nano. Lett.* 10 (2010) 2742.
- [30] P. May, U. Khan, A. Neill, J. Coleman, *J. Mater. Chem.*, 22 (2012) 1278.
- [31] S. Pavlidou, C.D. Papaspyrides, *Prog. Polym. Sci.*, 33 (2008) 1119.
- [32] D.R. Paul, L.M. Robeson, *Polymer* 49 (2008) 3187.

- [33] I. Corni, T. Harvey, J. Wharton, K. Stokes, F. Walsh, R. Kwood, *Bioinspir. Biom.* 7 (2012) 31001.
- [34] E. Munch, M. Launey, D. Alsem, E. Saiz, R.O. Ritchie, *Science* 322 (2008) 1516.
- [35] Y. Yu, Y. Lin, C. Lin, C. Chan, Y. Huang, *Polym. Chem.* 66 (2014) 535.
- [36] T. Yeh, T. Huang, H. Huang, Y. Huang, Y. Cai, S. Lin, J. Yeh, *Polym. Chem.* 3 (2012) 2209.
- [37] R.K. Raman, P. Banerjee, D. Lobob, H. Gullapallid, P.M. Ajayand, M. Majumder, *Carbon* 50 (2012) 4040.
- [38] J.M. Yeha, H.Y. Huanga, C.L. Chena, W.F. Sua, Y.H. Yub, *Surf. and Coat. Technol.* 200 (2006) 2753.
- [39] H. Yockell-Lelièvre, J. Desbiens, A. Ritcey, *Langmuir* 23 (2007) 2843.
- [40] E. Munch, M.E. Launey, D.H. Alsem, E. Saiz, A.P. Tomsia, R.O. Ritchie, *Science* 322 (2008) 1516.
- [41] M. Liu, S. Wang, Z. Wei, Z. Song, L. Jiang, *Adv. Mater.* 21 (2009) 665.
- [42] P. Podsiadlo, M. Michel, K. Critchley, S. Srivastava, M. Qin, J.W. Lee, E. Verploegen, A.J. Hart, Y. Qi, N.A. Kotov, *Angew.Chem., Int. Ed.* 38 (2009) 7073.
- [43] K. Putz, O.C. Compton, M. Palmeri, S. Nguyen, C. Brinson, *Adv. Funct. Mater.* 20 (2010) 3322.
- [44] L. Yang, S. Phua, C. Toh, S. Lau, J. Ma, X. Lu, *ACS Appl. Mater. Interfaces* 3 (2011) 3026.
- [45] A. Leon, R. Pernites, R. Advincula, *ACS Appl. Mater. Interfaces* (2012) 3169.
- [46] C.H. Chang, M.H. Hsu, C. Weng, W. Hung, T. Chuang, K. Chang, C. Peng, Y. Yen, J. Yeh, *J. Mater. Chem.* 1 (2013) 13869.

- [47] X. He, C. Chiu, M. Esmacherb, H. Liang, *Surf. and Coat. Technol.* 237 (2013) 320.
- [48] X. Huang, J.D. Chrisman, N.S. Zacharia, *ACS Macro. Lett.* 2 (2013) 826.
- [49] S.M. Doucet, M.G. Meadows, *J. R. Soc. Interface* 6 (2009) 115.
- [50] R.O. Stoddard, M. C. Prum, *Behavioral Ecology* 22 (2011) 1042.
- [51] P. Vukusic, J.R. Sambles, *Nature* 422 (2003) 852.
- [52] S. Vignolini, P. Rudal, A. Rowland, U. Steiner, *PNAS* 39 (2012) 15712.
- [53] H. Hoffmann, *Adv. Mater.* 6 (1994) 116.
- [54] K.P. Loh, Q. Bao, G. Eda, M. Chhowalla, *Nature Chemistry* 2 (2010).
- [55] C.M. Soukoulis, M. Wegener, *Nature Photonics* 5 (2011) 523.
- [56] M.D. Stoller, S. Park, Y. Zhu, J. An, R.S. Ruoff, *Nano. Lett.* 8 (2008) 3498.
- [57] C. Lee, X. Wei, J.W. Kysar, J. Hone, *Science* 321 (2008) 385.
- [58] K.I. Bolotin, K.J. Sikes, Z. Jiang, M. Klima, P. Kim, H.L. Stormer, *Solid State Commun.* 146 (2008) 351.
- [59] A.A. Balandin, S. Ghosh, W. Bao, I. Calizo, D. Teweldebrhan, F. Miao, C.N. Lau, *Nano. Lett.* 8 (2008) 902.
- [60] T. Kurkina, S. Sundaram, R.S. Sundaram, F. Re, M. Masserini, K. Kern, K. Balasubramanian, *ACS Nano.* 6 (2012) 5514.
- [61] X.L. Sun, Z. Welsher, K. Robinson, J.T. Goodwin, A. Zaric, S. Dai, *Nano. Res.* 1 (2008) 203.
- [62] D.A. Dikin, S. Stankovich, E.J. Zimney, R.D. Piner, G.H.B. Dommett, G. Evmenenko, S.T. Nguyen, R.S. Ruoff, *Nature* 448 (2007) 457.

- [63] Z. Xu, C. Gao, *Nat. Commun.* 2 (2011) 571.
- [64] J. Shang, L. Ma, J. Li, T. Yu, G.G. Gurzadyan, *Sci. Rep.* 2 (2012) 792.
- [65] G. Eda, M. Chhowalla, *Adv. Mater.* 22 (2010) 2392.
- [66] S. Park, R.S. Ruoff, *Nat. Nanotech.* 4 (2009) 217.
- [67] G. Eda, C. Mattevi, H. Yamaguchi, H. Kim, M. Chhowalla, *J. Phys. Chem. C* 113 (2009) 15768.
- [68] K. Shopsowitz, H. Qi, W. Hamad, M. MacLachlan, *Nature* 468 (2010) 422.
- [69] F. Castles, F.V. Day, *Nat. Mater.* 11 (2012) 599.
- [70] W.S. Hummers, R.E. Offeman, *J. Am. Chem. Soc.* (1958) 1339.
- [71] N.V. Medhekar, A. Ramasubramaniam, R.S. Ruoff, *ACS Nano* 4 (2010) 2300.
- [72] S. Stankovich, R.D. Piner, X. Chen, N. Wu, S. Nguyen, R.S. Ruoff, *J. Mater. Chem.* 16 (2006) 155.
- [73] W. Zhang, W. He, X. Jing, *J. Phys. Chem. B* 114 (2010) 10368.
- [74] X. Wang, H. Bai, G. Shi, *J. Am. Chem. Soc.* 133 (2011) 6338.
- [75] A. Ray, *Nature* 231 (1971) 313.
- [76] T. Greaves, C.J. Drummond, *Chem. Soc. Rev.* 37 (2008) 1709.
- [77] F. Kim, S. Kwan, J. Akana, P. Yang, *J. Am. Chem. Soc.* 123 (2001) 4360.
- [78] V. Geringer, M. Liebmann, T. Echtermeyer, S. Runte, M. Morgenstern, *Phys. Rev. Lett.* 102 (2009).
- [79] A. Fasolino, J.H. Los, M.I. Katsnelson, *Nat. Mater.* 6 (2007).

- [80] S.V. Morozov, K.S. Novoselov, M.I. Katsnelson, F. Schedin, L.A. Ponomarenko, D. Jiang, A.K. Geim, *Phys. Rev. Lett.* 97 (2006).
- [81] C. Cheng, D. Li, *Adv. Mater.* 25 (2012) 13.
- [82] J.I. Paredes, S. Villar, A. Martínez, J.M. Tascon, *Langmuir* 24 (2008) 10560.
- [83] R. Larciprete, S. Fabris, T. Sun, P. Lacovig, A. Baraldi, S. Lizzit, *J. Am. Chem. Soc.* (2011) 17315.
- [84] A. Ganguly, S. Sharma, P. Papakonstantinou, J. Hamilton, *J. Phys. Chem. C* 115 (2011) 17009.
- [85] S. Park, J. An, J. Potts, A. Velamakanni, S. Murali, R.S. Ruoff, *Carbon*, 49 (2011) 3019
- [86] G. Platz, C. Thunig, H. Hoffmann, *Prog. Colloid Polym. Sci.* 83 (1990) 167.
- [87] I.H. Tseng, M.H. Tsai, C.W. Chung, *ACS Appl. Mater. Interfaces* 6 (2014) 13098.
- [88] B.M. Yoo, H.J. Shin, H.W. Yoon, H.B. Park, *J. Appl. Polym. Sci* 131 (2014) 39628.
- [89] T. Duncan, *J. Colloid Interface Sci.* 363 (2011) 1.
- [90] W.K. Chee, H.N. Lim, H.N. Ming, I. Harrison, *RSC Adv.* 5 (2015) 68014.
- [91] M. Gupta, Y. Lin, T. Deans, E. Baer, A. Hiltner, D.A. Schiraldi, *Macromolecules* 43 (2010) 4230.
- [92] L.J. Cote, F. Kim, J. Huang, *J. Am. Chem. Soc.* 131 (2009) 1043.
- [93] X. Li, G. Zhang, X. Bai, X. Sun, X. Wang, E. Wang, H. Dai, *Nat. Nanotech.* 3 (2008) 538.
- [94] Jeremy T. Robinson, M. Zalalutdinov, J.W. Baldwin, E.S. Snow, Z. Wei, P. Sheehan, B.H. Houston, *Nano. Lett.* 8 (2008) 3441.



- [95] M.A. Priolo, D. Gamboa, K.M. Holder, J.C. Grunlan, *Nano. Lett.* 10 (2010) 4970.
- [96] K. Apaydin, T. Fouquet, M. Jimenez, S. Bourbigot, D. Ruch, *RSC Adv.* 4 (2014) 43326.
- [97] M. Wong, R. Ishige, K.L. White, P.L. Kim, R. Krishnamoorti, R. Gunther, T. Higuchi, H. Jinnai, A. Takahara, R. Nishimura, H.J. Sue, *Nat. Commun.* 5 (2014) 3589.
- [98] E.L. Cussler, S. E. Hughes, W.J. Ward, *J. Membr. Sci.* 38 (1988) 161.
- [99] L. Sun, W.J. Boo, A. Clearfield, H.Q. Pham, H.J. Sue, *J. Mem. Sci.* 318 (2008) 129.
- [100] L.Y. Sun, W.J. Boo, D.Z. Sun, A. Clearfield, H.J. Sue, *Chem. Mater.* 19 (2007) 1749.
- [101] M.H. Tsai, H. Tseng, J.C. Chiang, J.J. Li, *ACS Appl. Mater. Interfaces* 6 (2014) 8639.
- [102] P. Li, M. Wong, X. Zhang, H. Yao, R. Ishige, A. Takahar, M. Miyamoto, R. Nishimura, H.J. Sue, *ACS Photonics* 1 (2014) 78.
- [103] A.A. Balandin, S. Ghosh, W. Bao, I. Calizo, D. Teweldebrhan, F. Miao, C.N. Lau, *Nano. Lett.* 8 (2008) 902.
- [104] J.W. Jiang, J.S. Wang, B. Li, *Phys. Rev. B* 80 (2009) 113405.
- [105] L. Chen, M. Feng, H. Zhan, *RSC Adv.* 4 (2014) 30689.
- [106] Y.Y. Zhang, Q.X. Pei, M. Hucd, Z. Zonge, *RSC Adv.* 5 (2015) 65221.
- [107] C. Chang, T. Huang, C. Peng, T. Yeh, W. Hung, *Carbon* 50 (2012) 5044.
- [108] O.C. Compton, S. Kim, C. Pierre, J.M. Torkelson, S.T. Nguyen, *Adv. Mater.* 22 (2010) 4759.
- [109] D. Jiang, V.R. Cooper, S. Dai, *Nano. Lett.* 9 (2009) 4019.

- [110] C.H. Chang, T.C. Huang, C.W. Peng, T.C. Yeh, W.I. Hung, C.J. Weng, T.I. Yang, J.M. Yeh, H.I. Lu, *Carbon* 50 (2012) 5044.
- [111] Y. Yu, Y. Lin, C.H. Lin, C. Chan, Y.C. Huang, *Polym. Chem.* 5 (2013) 535.
- [112] J.C. Spear, B.W. Ewers, J.D. Batteas, *NANO Today* 10 (2015) 301.
- [113] J.C. Spear, J.P. Custer, J.D. Batteas, *Nanoscale* 7 (2015) 10021.
- [114] K. Sint, B. Wang, P. Kral, *J. Am. Chem. Soc.* 130 (2008) 16448.
- [115] P. Huang, C. Ruiz-Varga, A. Zande, W.S. Whitney, D.A. Muller, *Nature* 469 (2011) 389.
- [116] Y. Lee, S. Bae, H. Jang, S. Jang, S.E. Zhu, S.H. Sim, Y.I. Song, B.H. Hong, J.H. Ahn, *Nano. Lett.* 10 (2010) 490.
- [117] K. White, P. Li, Y. Sumi, H.-J. Sue, *J. Phys. Chem. B* 118 (2014) 362.
- [118] M. Wong, R. Ishige, T. Hoshino, S. Hawkins, P. Li, A. Takahara, H.J. Sue, *Chem. Mater.* 26 (2014) 1528.
- [119] P. Li, K.L. White, C. Lin, D.Kim, A.Muliana, R.Krishnamoort, R. Nishimura, H.J. Sue, *ACS Appl. Mater. Interfaces* 6 (2014) 10188.
- [120] K. White, M. Wong, P. Li, M. Miyamoto, Y. Higaki, A. Takahara, H.J. Sue, *Soft Mater.* 11 (2014) 954.
- [121] K.L. White, P. Li, H. Yao, R. Nishimura, H.J. Sue, *Rheologica. Acta.* 7 (2014) 571.
- [122] K. Hyun, S.H. Kim, K.H. Ahn, S.J. Lee, *J. Newton. Fluid Mech.* 107 (2002) 51.
- [123] A.V. E. Picarda, J.-F. Gérardc, E. Espuchea, *J. Membr. Sci.* 292 (2007) 133.
- [124] S. Takahashia, H.A. Goldbergb, C.A. Feeneyb, D.P. Karimb, M. Farrellb, K. Leary, D.R. Paula, *Polymer* 47 (2006) 3083.

- [125] J. Bicerano, J.F. Douglas, D.A. Bruneau, *J. Macromol. Sci. A* 39 (1999) 561.
- [126] D.J. Chaiko, A.A. Leyva, *Chem. Mater* 17 (2005) 13.
- [127] M.A. Osman, V. Mittal, M. Morbidelli, U.W. Suter, *Macromolecules* 37 (2004) 7250.
- [128] A. Yu, P. Ramesh, X. Sun, E. Bekyarova, M.E. Itkis, R.C. Haddon, *Adv. Mater* 20 (2008) 4740.
- [129] E. Bekyarova, T.W. Chou, E.T. Thostenson, R.C. Haddon, A. Yu, M.E. Itkis, D. Fakhruddinov, *J. Phys. Chem. C* 11 (2007) 17865.
- [130] C. Yuan, C. Wang, K. Hwang, W. Chao, *Biosens. Bioelectron.* 26 (2011) 2858.
- [131] J. Yan, J.P. Liu, Z. Fan, T. Wei, L. Zhang, *Carbon* 50 (2011) 2858.
- [132] M. Waje, W. Li, Y. Yan *Nanotechnology* 16 (2005) 395.
- [133] R. Nair, H. Wu, P. Jayaram, I. Grigorieva, A. Geim, *Science* 335 (2012) 442.
- [134] A. Balandin, S. Ghosh, W.Z. Bao, I. Calizo, D. Teweldebrhan, *Nano. Lett.* 8 (2008) 902.
- [135] D. Dikin, S. Stankovich, E. Zimney, S. Nguyen, R. Ruoff, *Nature* 448 (2007) 457.
- [136] H. Shi, A. Barnard, I. Snook, *Nanoscale* 4 (2012) 6761.
- [137] T. Booth, P. Blake, R. Nair, D. Jiang, E. Hill, U. Bangert, *Nano. Lett.* 8 (2008) 2442.
- [138] Q. Zheng, X. Lin, N. Yousefi, N. Yeung, Z. Li, J. Kim, *ACS Nano.* 5 (2011) 6039.
- [139] V. Tung, M. Allen, Y. Yang, R. Kaner, *Nanotechnology* 4 (2009) 25.
- [140] C. Cheng, J. Huang, Q. Zhang, Y. Yang, *Carbon* 50 (2012) 659.

- [141] C. Tang, K. Hackenberg, Q. Fu, P. Ajayan, H. Ardebili, *Nano. Lett.* 12 (2012) 1152.
- [142] L. Wang, D. Wang, X. Dong, Z. Zhang, X. Pei, X. Chen, *Chem. Commun.* 47 (2011) 3556.
- [143] M. Zhao, Q. Zhang, W. Zhang, J. Huang, H. Zhang, *J. Am. Chem. Soc.* 132 (2010) 14739.
- [144] H. Li, G. Zhu, Z. Liu, Z. Yang, Z. Wang, *Carbon* 48 (2010) 4391.
- [145] K. White, M. Shuai, X. Zhang, H. Sue, R. Nishimura, *Carbon* 49 (2011) 5124.
- [146] D. Sun, C. Chu, H. Sue, *Chem. Mater.* 22 (2010) 3773.
- [147] S. Liang, J. Walda, A. Paul, *Nano. Lett.* 2 (2002) 557.
- [148] M. Nakata, G. Zanchetta, Brandon, C. Jones, *Science* 318 (2007) 1276.
- [149] D. Sun, H. Sue, Z Cheng, Y. Martinez, E. Velasco, *Phys. Rev. E* 80 (2009) 41704.
- [150] J. Paredes, R.S. Villar, J. Tasco, *Langmuir* 24 (2008) 10560.
- [151] X. Peng, X. Liu, D. Diamond, K. Lau, *Carbon* 49 (2011) 3488.
- [152] L.B. Bonderer, A.R. Studart, L.J. Gauckler, *Science* 319 (2008) 1069.
- [153] H.Y. Huang, T.H. Huang, T. Yeh, C.Y. Tsai, C. Lai, M. Tsai, J. Yeh, Y.C. Chou, *Polymer* 52 (2011) 2391.
- [154] T.C. Huang, Y.A. Sua, T.C. Yeha, C.P. Wua, K. Huang, Y.C. Chou, J. Yeh, Y. Wei, *Electrochim. Acta.* 56 (2011) 6142.
- [155] P. Sarkar, P.S. Nicholson, *J. Am. Ceram. Soc.* 79 (1996) 1987.

- [156] K.W. Putz, O.C. Compton, M.J. Palmeri, S.T. Nguyen, L.C. Brinson, *Adv. Funct. Mater.* 20 (2010) 3322.
- [157] P. Li, X. He, T. Huang, K. White, X. Zhang, H. Liang, H. Sue, *J. Mater. Chem. A* 3 (2015) 2669.
- [158] G. Kear, B.D. Barker, F.C. Walsh, *Corrosion Science* 46 (2004) 109.
- [159] A.R. Marder, *Prog. Mater. Sci.* 45 (2000) 191.
- [160] X. Cheng, Z. Wang, Y. Yan, *Electrochem. Solid State Lett.* 4 (2001) 23.
- [161] F. Zhang, L. Zhao, H. Chen, S. Xu, D.G. Evans, X. Duan, *Angew. Chem. Int. Ed.* 47 (2008) 2466.
- [162] S. Chen, L. Brown, M. Levendorf, W. Cai, X. Li, C. Magnuson, R. Piner, J. Kang, J. Park, R.S. Ruoff, *ACS Nano.* 5 (2011) 1321.
- [163] F. Zhou, Z. Li, G. Shenoy, L. Li, H. Liu, *ACS Nano.* 7 (2013) 6939.
- [164] A. Yagan, N. ozcicek, P. Yildiz, *Electrochim. Acta.* 30 (2008) 5242.
- [165] T. Huang, Y. Yeh, H. Huang, W. Jia, W. Chou, W. Hung, J. Yeh, M. Tsai, *Electrochim. Acta.* 56 (2011) 10151.
- [166] Z. Chen, Z. Dong, D. Yang, H. Lu, *Adv. Mater.* 25 (2013) 5352.
- [167] C. Chang, T.C. Huang, T. Yeh, H. Lu, J.M. Yeh, *Carbon* 14 (2012) 5044.